SAPIENZA
UNIVERSITÀ DI ROMA

Ph.D. Course in Mathematical Models for Engineering, Electromagnetism and Nanoscience

- Curriculum: Material Science –

XXXVI cycle

Advanced carbon-based nanostructured materials for energy storage devices

PhD student: Pierfrancesco Atanasio

Supervisor: Prof. Marco Rossi

Cosupervisor: Dr. Francesca A. Scaramuzzo

Department of Basic and Applied Science for Engineering

PhD coordinator: Prof. Lorenzo Giacomelli

Index

Figure Index

Table Index

1 Introduction

1.1 Energy Transition

The increasing of world's population, pushed by the global economy and urbanisation, has dramatically increased the energy demand and the exploitation of resources, bringing along a consistent asymmetry in supply over demand ratio.[1–3] However, in 2018, according to International Energy Agency (IEA) energy demand was still at 80% by fossil fuels (namely coal, natural gas, and oil), with electricity and heat only accounting for 19.31% and 3.03% of energy consumption, respectively.[4,5] A distribution over the global energetical supply is shown in Figure 1-1 (from Tian et al.).[6]

The gradual substitution (ideally the elimination) of fossil fuels in energy production with renewable sources is one of the best paths to minimize pollutant emissions and global warming.[7,8] This idea is known as Energy Transition, and it refers to the gradual replacement of fossil systems for energy production and consumption to renewable energy like solar or wind.[6] The International Renewable Energy Agency predicts that, by 2050, two-thirds of the world's energy will be sourced from renewable energy.[9]

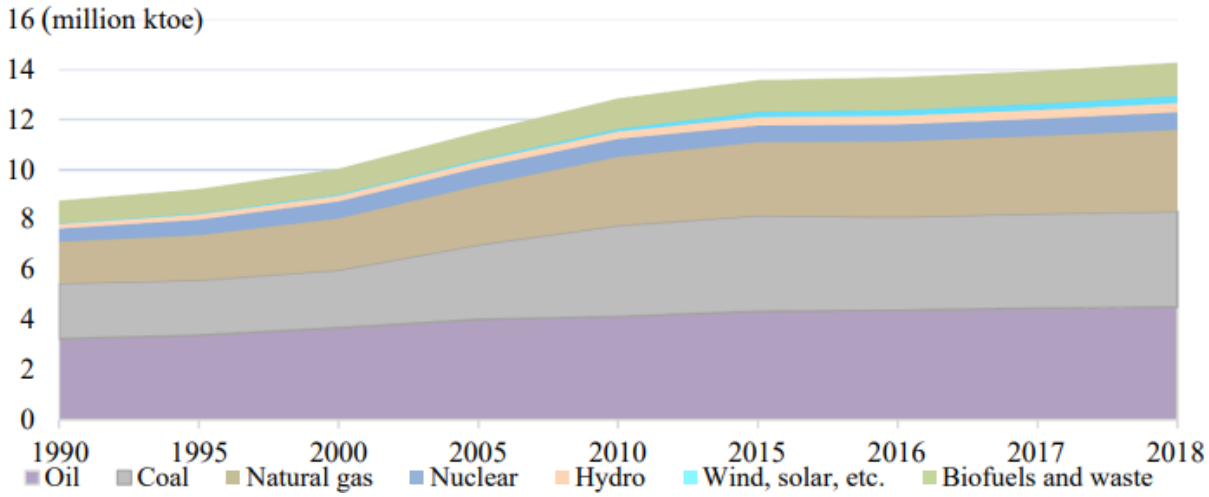

Figure 1-1 Global energy supply from 1990 to 2018, data source IEA. [6]

Considering this scenario, along with the uprising critical concerns about pollution, global warming, environmental depletion and the necessity of a decarbonization policies, governments and global organizations have decided to pledge their efforts on the development of alternative strategies, in terms of sustainable materials and processes.[10,11] For example, in 2019, the European Commission published the European Green Pact (EGP), which stated the policy efforts of the member states to achieve the goal of zero emissions of greenhouse gas during the twenty years ranging from 2030 to 2050.[12] Similar intent was declared two years later in 2021 in Glasgow during United Nations Climate Change Conference (COP26), where world leaders pledged to reduce gas emissions and limit the increase of world temperatures to 1.5°C by 2050.[13,14] An update distribution of the utilization over

the world of renewable energy is shown in Figure 1-2, and it is taken from data of the Energy Institute - Statistical Review of World Energy (2023).[15]

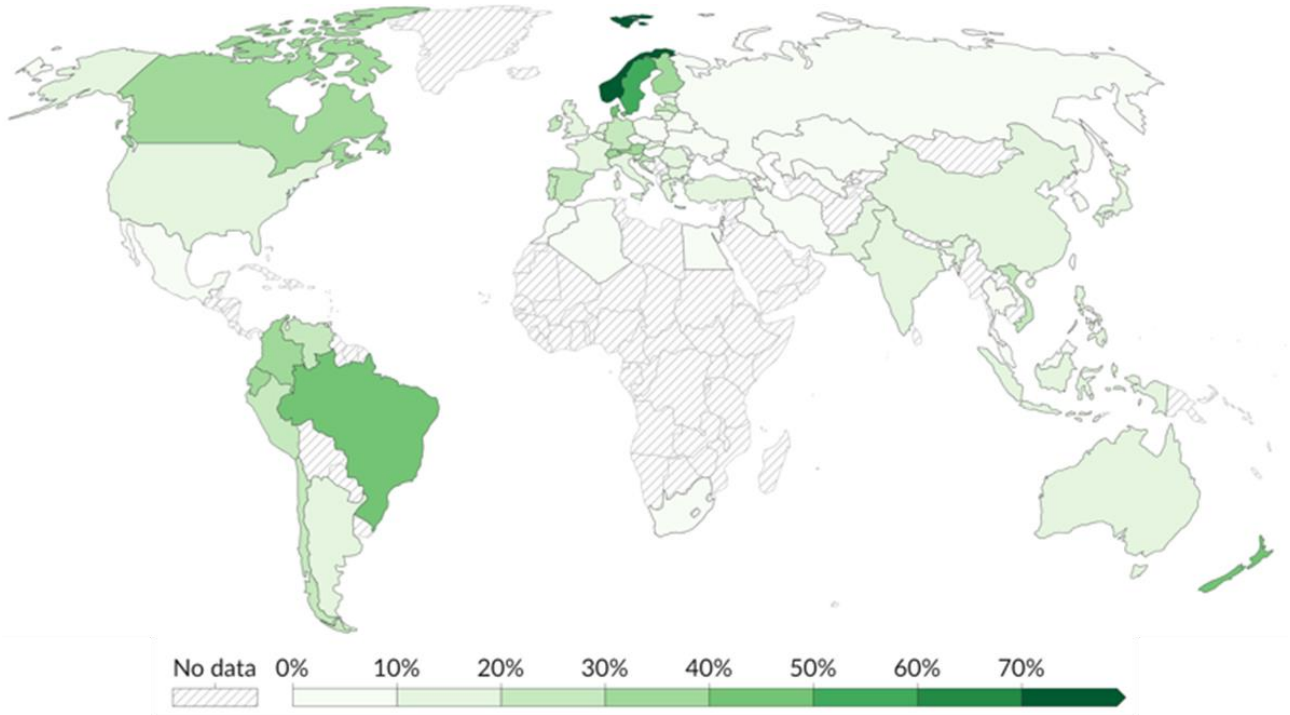

Figure 1-2 Renewable energy consumption in the world, according to Energy Institute - Statistical Review of World Energy (2023).[15]

However, even if renewable forms of energy might appear the alternative to fossil fuels, sources of green energy like sun or wind depend on the time of the day and also on weather conditions, and this makes them unreliable.[16] Therefore, it is necessary to develop high-performance environmental-friendly energy storage devices that will allow a continuous and efficient use of erratic renewable sources of energy to avoid shortages and inefficiency.[17,18] To achieve this result many different solutions have been proposed in scientific literature, and a wide amount of researches and laboratories tried to apply electrochemical devices on this task.[19–22]

1.2 Electrochemical Devices

Storing energy in electrochemical systems is desirable because these devices can offer high energy density per mass unit, and since they do not depend on thermal gradients, they are not limited by Carnot efficiency.[16,23,24] Nowadays many electrochemical devices like batteries, fuel cells or capacitors exist and are being continuously upgraded by efforts and advances in research, but there is no standalone solution and a combination of more devices is necessary.[16] Therefore, present storage systems should be improved through novel materials processing to reach better performances as well as to also guarantee greener alternatives to currently available materials.

Fuel cells can be defined as electrochemical devices able to convert chemical energy of a fuel into electrical energy under a continuous flow.[25–27] These devices do not require conventional fossil fuels, but they use reductant species like hydrogen, ethanol, methanol or methane on the anode

and usually air or oxygen as oxidant over cathode, with water as by-product.[25] A scheme of a fuel cell working is shown in Figure 1-3 (from Hassan et al.).[28]

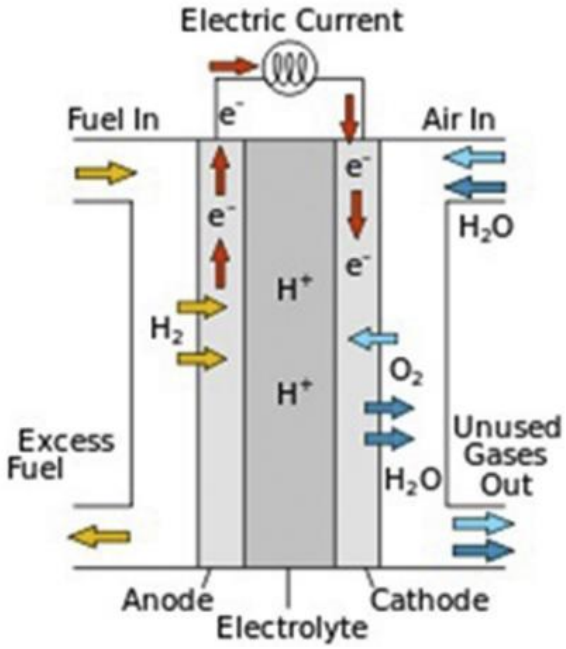

Figure 1-3 Schematic representation of a Fuel Cell.[28]

Fuel cells offer high capacitance and their sustainable mechanism results in nearly zero emission of CO_2 or other greenhouse gases, they avoid fossil fuels and are overall convenient and easily adaptable in many different portable or stationary systems.[28] However, they are also hindered by the high cost of catalysts, complexity of the components, low durability and stability issues.[26]

Other widely popular electrochemical devices are Lithium-ion batteries, which were first commercialized by Sony and Asahi Group in 1991, and have been quickly applied to portable electronics, e.g. 3C devices, current electric vehicles (EV), plug-in hybrid electric vehicles (PHEVs) and electric grid energy systems.[30,31] Their massive diffusion is due to their features in terms of affordable cost, market acceptance, high energy density and durability, which make them highly versatile and robust respect to the most part of other energy storage systems.[32] The interesting properties of these devices in terms of densities of power and energies are shown in **Errore. L'origine riferimento non è stata trovata.** in a Ragone plot (picture taken from Meesala et al.).[29]

Nowadays we are experiencing a rapid increase of interest and demand over electric vehicles and the demand for lithium-ion batteries with high energy density capable of lasting for many cycles is increasing as well.[33]

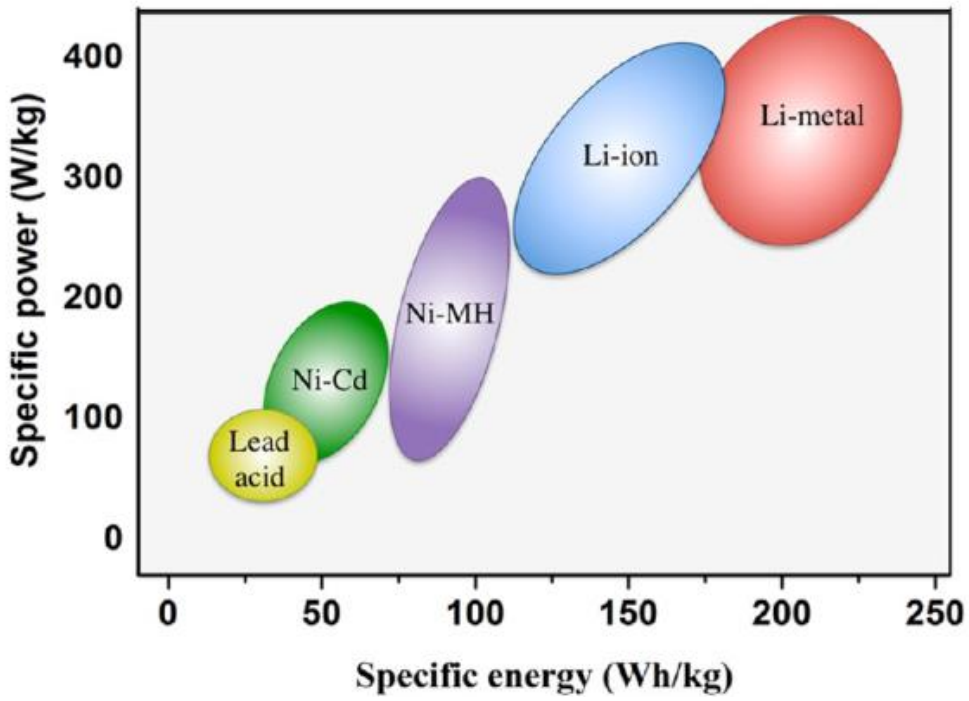

Figure 1-4 Ragone Plot of different kinds of rechargeable batteries.[29]

Working mechanism of a lithium-ion device is shown in Figure 1-5 taken from Roy et al.[34] During charge, lithium ions contained in the electrolyte are stored in the anode through intercalation or alloying process, while during discharge the lithium ions travel to a cathode which is usually made of lithium salts of oxides or phosphate of transition metals.[35,36] Research to improve the performances of a lithium-ion batteries is carried on concerning each and every component, i.e. anodes, cathodes, electrolytes, separators, and also cell design and protective systems, both updating old materials and inventing new solution.[37,38]

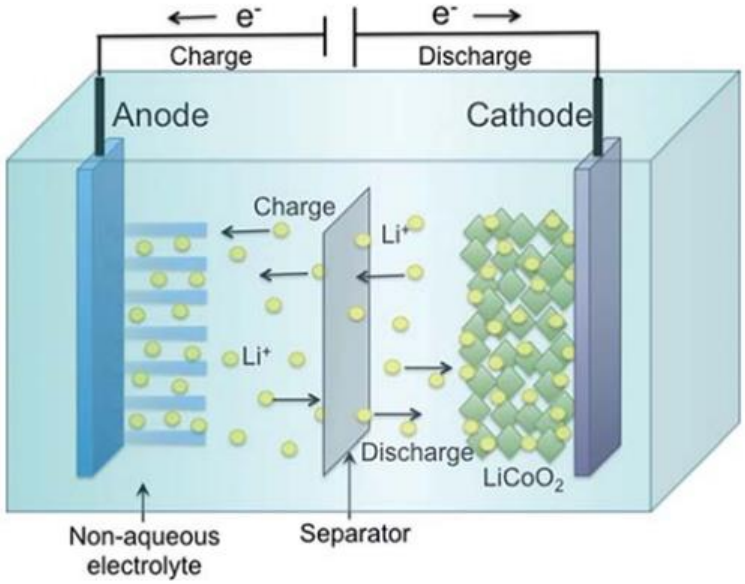

Figure 1-5 Schematic diagram of a lithium-ion battery using $LiCoO_2$ as cathode material (picture taken from Ref 34).

Unfortunately, Li-ion batteries suffer from slow power delivery and uptake, that is a limitation for applications in which a faster and higher-power energy storage is needed. Therefore different devices like supercapacitors, also called electrochemical capacitors (EC), can be used.[39,40] The term "supercapacitors" actually indicates a family of devices all characterised by the capability of being fully charged and discharged within seconds with low energy density but much higher power delivery than a dieletric capacitor or a lithium-ion battery, and high cyclic stability with fast charging/discharging rates.[40] A Ragone plot showing their power and energy densities taken from Permatasari et al. is shown in Figure 1-6.[41] Depending on their charge accumulation method, supercapacitors can be classified into three main categories: electric double layer capacitors (EDLCs), pseudocapacitors, and hybrid supercapacitors.[41]

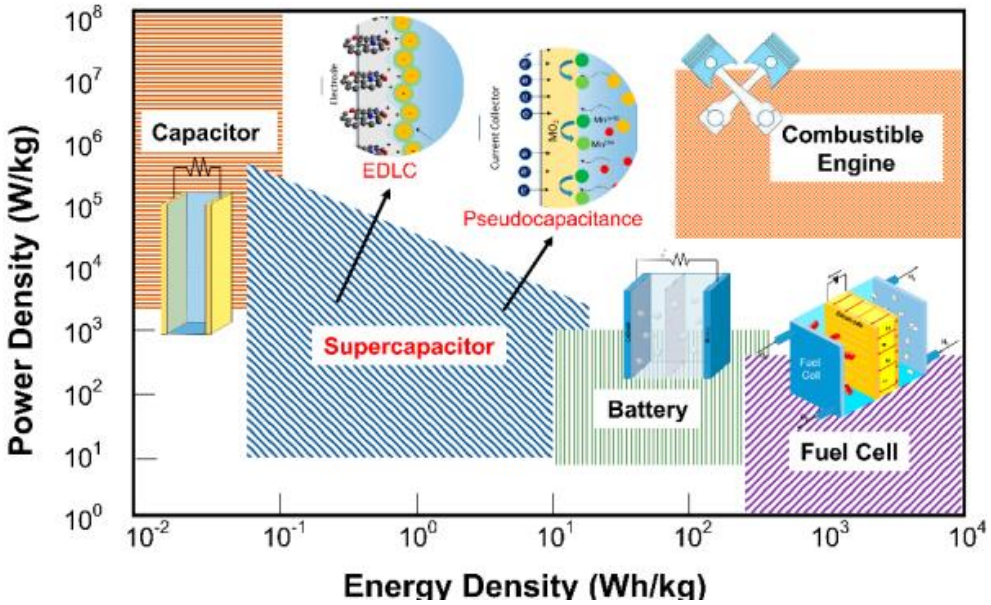

Figure 1-6 Ragone plot for different electrochemical devices taken from Ref. 41.[41]

While a EDLC uses electrode materials capable of accumulating charges over their surfaces, thus storing energy with the adsorption or desorption of ions, in a pseudocapacitor along with this charge accumulation we can also observe fast and highly reversible faradic reactions.[42,43] On the other hand, hybrid capacitors are peculiar devices where one electrode is a battery-like electrode, while the other is a capacitive one. They are generally named after the used cation, e.g. sodium-ion hybrid capacitors or lithium-ion hybrid capacitors.[44]

In EDLCs the capacitance is often determined by the available specific surface area over the electrode that determines the extension of the Helmholtz layer where the ions accumulate over the charged surface.[45,46] A schematic illustration of this mechanism is shown in Figure 1-7 taken from Forouzandeh et al.[47]

When a faradic reaction is involved, the specific capacitance is mostly due to the redox happening at the interface between electrodes and electrolyte; a pseudocapacitor normally uses polymers or metal oxides that reacts offering larger specific capacitance but with poor electron transfer ability and a shorter life compared to EDLC.[48,49]

Despite of the mechanism involved, supercapacitors are worldwide studied as complementary storage devices to secondary battery systems coupling different devices to guarantee high power when needed.[50,51] However, the low energy density, the cost of synthesis, and the availability of material resources are still a challenge for these devices. Therefore, they have become a hot focus in scientific communities, and the development of low-cost electrodes from green synthesis is currently considered a cutting-edge goal.[52]

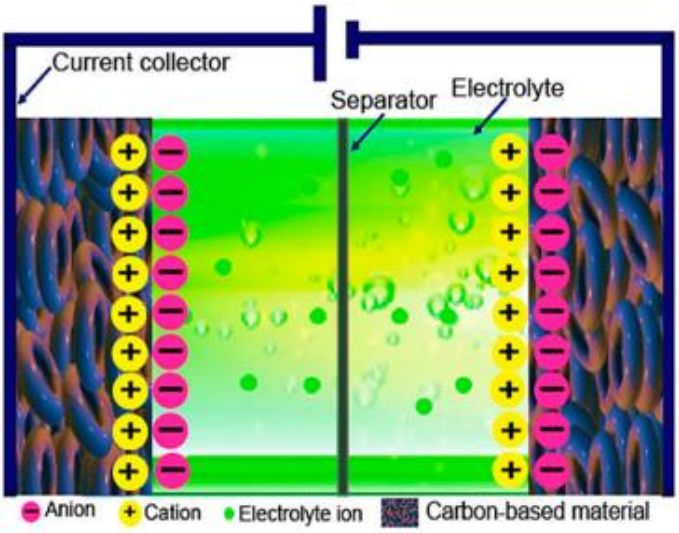

Figure 1-7 Schematic illustration of a double layer capacitor taken from Ref. 47.[47]

1.3 Carbon as golden standard for electrodes

In all the different electrochemical devices illustrated in the previous paragraphs, carbon is widely used or studied as electrode material.[53–55] Carbon materials are an already well established reality in the electronics field thanks to their electrical conductivity, high surface area and natural ability to self-expand with no fragmentation. However, they are still studied in all structures and size, from 0D nanostructured materials to porous carbon, to improve devices performances.[56]

For example, carbon-based cathodes are explored for the reduction of oxygen in anion exchange membrane fuel cells in order to be a cost effective and abundant substitute to common catalysts like platinum, rhodium or iridium/ruthenium oxide.[57] Also in biological fuel cells, where bacterial metabolic energy is transformed into electricity over the surface of different electrodes, carbon is studied in different forms, like carbon nanotubes, nanosheets, quantum dots or pyrolyzed carbons.[58,59]

Conversely, in devices like lithium-ion batteries, carbon, and in particular graphite, has been used ever since the first commercialization of these devices, as the anode for the intercalation of lithium cations and it is still the dominant solution in the market.[60,61] An overview of the possible materials that are capable of being used as anodes in lithium-ion devices is shown in Figure 1-8 taken from Lu et al.[62].

Lithium-ion batteries currently apply graphitic anodes that can offer a theoretical capacitance around 372 $mAhg^{-1}$.[63,64] Besides its low cost, graphite is able to reversibly intercalate Li^+ within its

plane, and also offers high electrical conductivity and structural stability.[65] One Li^+ cation is intercalated per graphite hexagonal ring, according to the following reaction over a single C_6 ring:[66]

$$Li^+ + C_6 + e^- \rightleftharpoons LiC_6$$

Nevertheless, despite widespread use of graphite, lithium-ion batteries anode still presents issues of great concern: capacitance should be increased to face higher demand of energy, while durability is unsatisfactory with high cost ($900–1300 per kW h) and improvable safety systems.[67,68] Aiming at solving these issues, efforts have been devoted towards new battery systems, e.g. using different charge carrier like sodium ions, or moving to safe, low-cost, and naturally abundant raw materials to build the components of the device.[69,70] These efforts involves also the anode preparation, where different carbon structures materials or even different elements are tested, like partially graphitic highly disordered materials made of both sp^2 and sp^3 carbon or alternative materials as Si or Ge.[63–65,68,71]

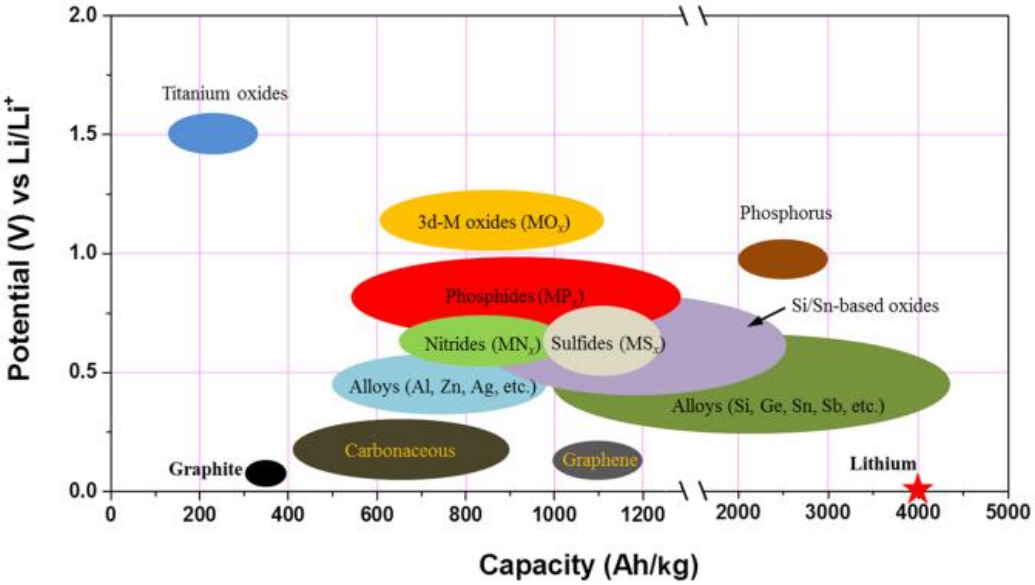

Figure 1-8 Schematic illustration of active anode materials for the next-generation lithium batteries (Ref. 62).[62]

One of the greatest challenges for carbon materials including graphite, when used as an anode is the mechanism and kinetic of formation of the passivation films known as solid-electrolyte interface (SEI).[72]

This film is formed in the very first cycles by interfacial reactions, when the electrolyte is degraded over the surface generating a passivating film that induces an irreversible loss of capacitance but, if properly conducted, is also responsible for stabilizing anodes from further degradation.[74,75] A representation of the composition of a SEI layer over anodes surface is shown in Figure 1-9 taken from Spotte-Smith et al.[73]

Supercapacitors make wide use of carbonaceous electrodes as well, since they guarantee high and controllable surface area, pore volume and size distribution, and high chemical stability, properties which are all fundamental for guaranteeing the desired devices properties.[43,76,77] Moreover, carbon-

based structures can work with aqueous electrolyte, that offers a significantly simpler design of the device, despite a low operative potential window. [78] Liquid electrolytes for EDLC, in fact, are usually classified as aqueous, organic or ionic liquids, and the choice influences safety and performances of EDLCs; compared to water, organic electrolytes and ionic liquids can operate at higher voltage but offer lower ionic conductivity.[79,80] A wider operation voltage window is more appealing since the energy density is proportional to the square of the potential range.[79]

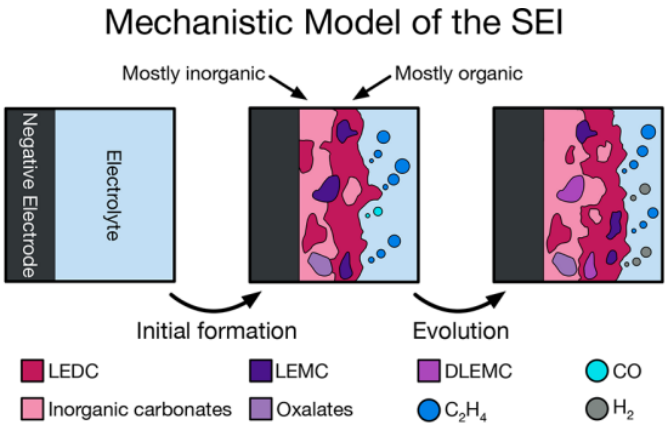

Figure 1-9 model of SEI formation over a carbonaceous anode (taken from Ref 73).[73], LEDC (lithium ethylene dicarbonate, LEMC (lithium ethylene monocarbonate), DLEMC (dilithium ethylene monocarbonate)

In any case, commercially available supercapacitor electrodes are often assembled using pure carbonaceous materials that, despite their advantages, they still present unresolved limitations.[76] These electrodes lack high specific capacitances and/or energy density required by commercial devices and often presents narrow range of operating voltages.[78,81] However, capacitors beneficial features are still worth of further researches to overcome their limits and to fabricate flexible energy storage devices.[76,82]

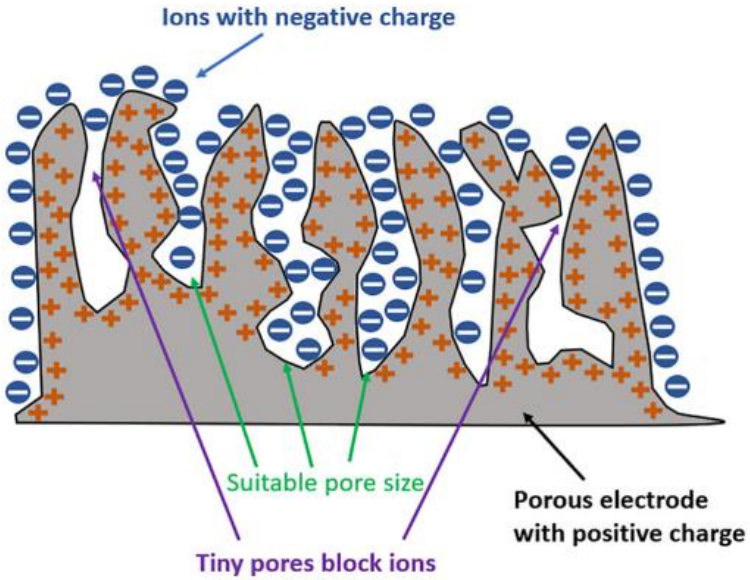

Figure 1-10 . A schematic diagram showing the relationship between ion and pore size on electrodes, taken from Hung et al.[80]

When fabricating an electrode, a crucial factor to achieve superior performances is porosity.[83] Since high surfaces improve capacitance, offering more sites over the electrode for accumulating charges, many efforts had been focused on fabricating high specific surface carbon materials, i.e. with smaller pores, since this leads to better performances.[83] However, tiny pores block or hinder the diffusion of ions inside carbon matrix, consequently it is actually better to achieve a hierarchical pore distribution that combines mesopores and micropores to maintain high capacitance still offering access low resistance to ion movements.[78,81] These principles are schematized in Figure 1-10 taken from Hung et al.[80] Considering these factors, in order to optimize carbon-based electrodes performances, it is necessary to find a compromise between its specific surface area and its pore size distribution.[84]

1.4 Aim of the thesis

As previously illustrated, despite its safety and robustness, the graphite anode behaviour and capacitance are currently considered insufficient in both the devices to meet the always growing energetic demand of modern technologies.[85] The general aim of this thesis is to further investigate over the capability of carbon-based electrode materials to offer solutions to the principal issues illustrated above for lithium-ion batteries and aqueous supercapacitors.

Therefore, three different materials all characterized by a structure of disordered graphite have been synthesised and tested: (i) a hybrid carbon/silicon composite material based on a multilayer of nanostructured components;(ii) carbon aerogels obtained by cellulose purified from a low-cost abundant biomass; (iii) a 0D carbon material, i.e. carbon dots, obtained from the same biomass via a facile top-down synthetic step.

Moreover, preliminary studies over the practicability of in operando functional measurements over the abovementioned materials have been carried out, making the first step towards the study of surface modifications via electrochemical in operando atomic force microscopy.

2 C/Si hybrid electrodes for Li-ion batteries

In this chapter a hybrid carbon/silicon composite anode for lithium-ion batteries is described. The anode is made of a particular carbon nanostructure called nanowalls (CNW) and commercially available nanosized Si powder assembled in a multilayer morphology of alternated layers with an industrially scalable process based on chemical vapor deposition (CVD) and deep coating.
Carbon nanowalls are graphitic structures made of 2D stacks of graphene sheets that grow mainly perpendicularly to the support and are interconnected in a 3D matrix.[86] The successive and alternate deposition of Si and CNW creates a material capable of hindering the swelling of the anode and improving the conductivity of the electrode.

2.1 Introduction to C/Si anodes in lithium-ion batteries

2.1.1 C/Si hybrid materials, purpose and goals

As already illustrated in chapter 1, graphite, and more in general carbon has always been used as anode in lithium-ion devices. However, efforts in research to overcome his low specific capacitance have been made to meet the energetic demand of modern society and technologies and different materials have been studied in the last decades to improve the capacitance and to achieve a higher energy density.[85] Silicon has been identified as a very promising candidate thanks to its availability, low cost, synthetic versatility and its outstanding theoretical capacitance (up to 4200mAhg^{-1} for $Li_{22}Si_5$ alloy).[33,87–90] However, Si electrodes suffer of volume expansions up to 300% of original volume during the discharge process, and repeated shrinkage and expansion induce fracturing and pulverisation of the lithium-silicon structures, as shown in Figure 2-1 taken from Di et al.[91].[89,92] These phenomena lead to the loss of electrical contact with a consequent decrease in electrical conductivity, and the constant formation of solid-electrolyte interface (SEI) layer all over the surface of electrodes.[31,33,91,93]

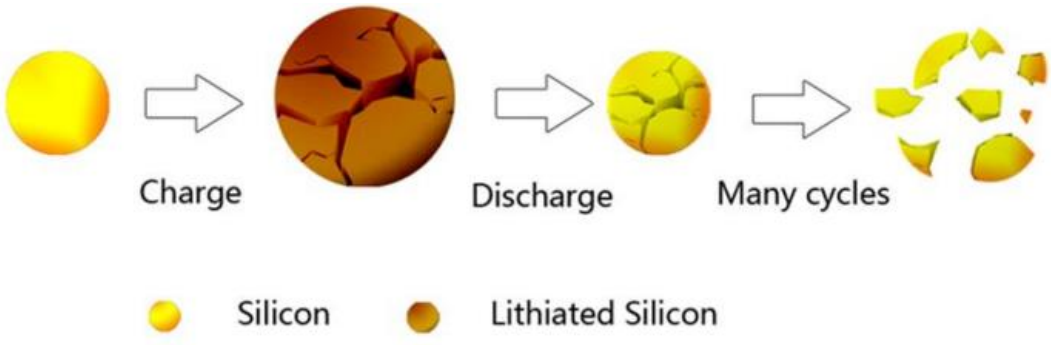

Figure 2-1 Schematic representation of a silicon anode cracking during charge and discharge cycles. image taken from Figure 1 of Di et al.[91]

Despite research over the fabrication of pure Si anodes has accomplished a lot, demonstrating that reducing Si dimension to the nanoscale can improve capacitance and length of life for devices, electrodes can still improve performances.[87,94,95] A first solution approach was coupling Si with a

second material that could help minimising and overcoming limits of pure silicon anodes, thus fabricating a hybrid electrode: the most studied candidate was graphite and, in general, carbon.[31,96] While Si improves capacitance, carbon can offer many beneficial properties, i.e. softness and compliance that accommodates the large expansion of silicon during cyclations, but also high electronic conductivity and capability of intercalating lithium ions in the crystalline lattice of graphite planes.[97,98] The overall ideal outcome of the union of carbon and silicon is a hybrid material where the beneficial characteristics of both components are enhanced, while their defects are compensated by the other element.[94] An illustration of this synergic effect along with the different mechanism of lithiation of both graphitic carbon and silicon is showed in Figure 2-2 taken from Chae et al.[94]

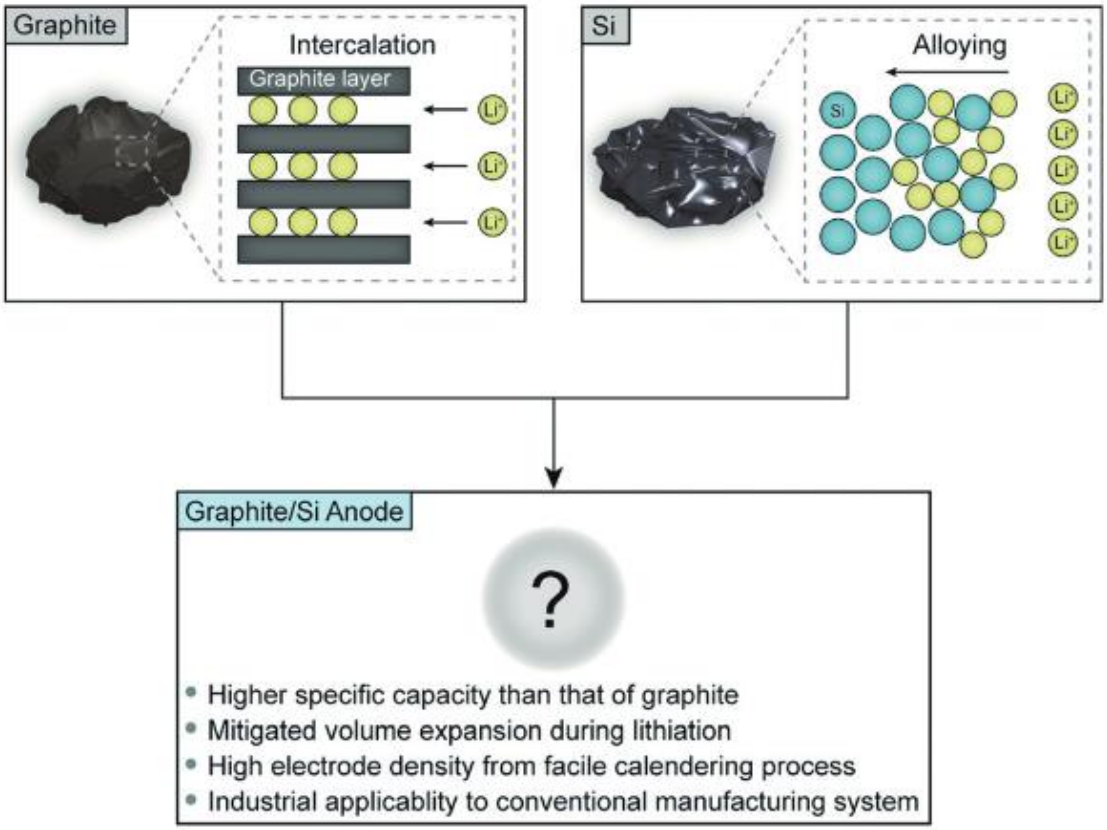

Figure 2-2 Schematic illustration of the advantages of co-utilization of both graphite and silicon and their synergic effect taken from Figure 3 of Chae t al.[94]

Many different synthetic strategies and architectures have been synthesised and tested in order to build a suitable material to meet the needs of market demands, with different approaches and a wide diversity of precursors and raw materials.[92,94,96] Nevertheless, many hybrid materials proposed in literature can't offer required performances in terms of integrity of the electrode, since a simple coating layer of carbon over Si particles might improve kinetics, but a closed matrix with no internal voids and space offers no space for Silicon to expand its structure and a properly developed porous structure with high surface area is required.[99] Moreover, high Si/C ratio and homogeneous distribution of Si in the carbon matrix improves both capacitance and life of the anode, and a lighter anode (weight of the current collector included) plays an important role in the determination of the

final gravimetric capacitance, therefore avoiding using a copper collector and building a free standing electrode could further improve performances.[94,99]

2.1.2 C/Si composite synthetic strategies

Various forms of high-capacitance silicon materials have been applied for the assembly of composites electrodes, from elemental Si, crystalline, amorphous, porous and many different morphologies, to silicon oxides or even alloys between Si and other metals.[100–102]

A schematic representation of synthetic strategies and possible final C/Si hybrid materials is show in Figure 2-3 taken from You et al.[31] and we can categorize materials according to their synthetic methods as: ball milling, spray drying, pyrolysis, hydrothermal process, liquid solidification, and chemical vapor deposition (CVD).

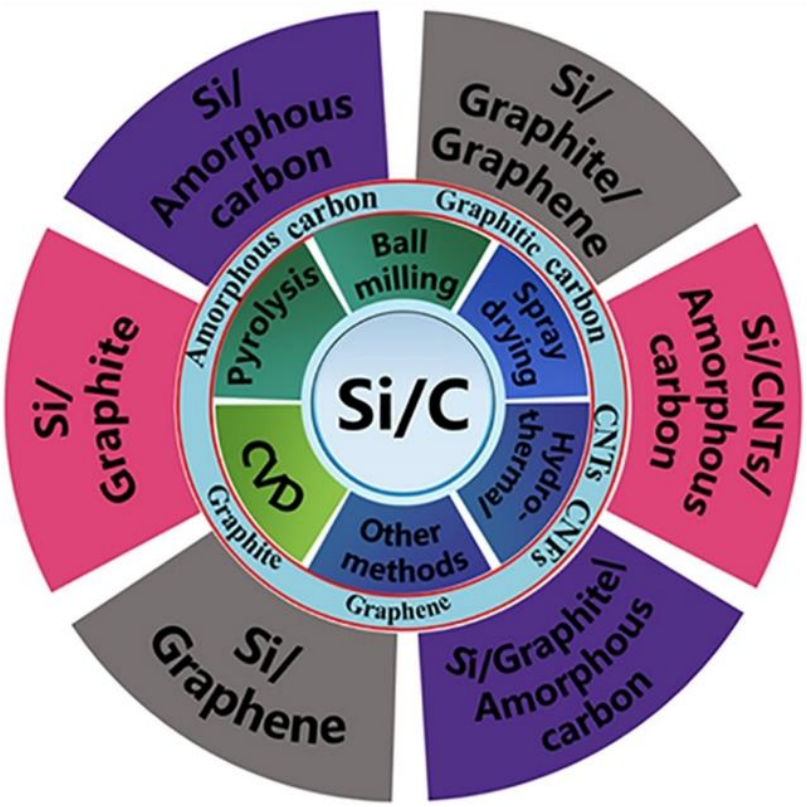

Figure 2-3 design strategies for Silicon and Carbon composites taken from graphical abstract from You et al.[31]

Ball milling is a clearly appealing physical method because of simplicity and cheapness of the instrumental equipment, and it is easy to scale it up in an industrial reality.[103–105] This method assures good adhesion and therefore electrical conductivity.[106] However, despite its simplicity, ball milling methods still require carefulness in setting the parameters of synthesis and in particular in controlling the duration of the experiment, since too much milling can destroy crystallinity and lead to side reactions.[31,94,103] Moreover, structurally damaged components often induce excessive irreversible capacitance in the first cycles and ensuring a narrow size distribution of particles is still challenging.[105,107]

Spray drying methods involve the formation of a dry powder from liquid solution where solvent gets evaporated by heating with under gas flow.[108] Diameter of the nozzle is crucial to determine the droplets dimensions and the size distribution of particles.[109] This method is quick, requires a single step, that can also be carried out in continuous, which is valuable for mass production, and particles are approximately spherical particles with hollow structure that reduces the bulk density of the product.[110–112] C/Si composites materials made with spray drying method has many advantages, pores are optimal to relieve Si expansions and the scalability allows to industrial applicate the anodes produced.[113,114] However, equipment cost, and size need to be taken into account as well as the low thermal efficiency due to the large amount of hot air entering the chamber without contacting directly particles.[111]

Pyrolysis at high temperature in controlled atmosphere is a simple method that is usually applied when the carbon source is a polymer or a biomass that are transformed into an amorphous carbon coating over silicon or silicon oxide.[115,116] Usually pore structure produced by pyrolysis is abundant and capable of buffering silicon expansion, nevertheless this synthetic method still is missing a proper control of the regularity of the coating thickness over the sample.[31]

Hydrothermal processes also are based on high temperature synthetic steps, but usually small organic molecules are applied after being dispersed with Si particles and applied temperature can be several hundred of degrees inferior to the simple pyrolysis.[117,118] The results, as showed by Chang et al.[119] offer carbon coatings capable of promoting the migration of Li^+ in porous structures suitable for the expansion and shrinkage of silicon. These processes are environmentally friendly with broad prospects, capable of giving final products of high purity and homogeneity, but with a consistent problem in the process scalability due to safety concerns over a pressurized reactor.[31]

Liquid solidification has been used for composites with more than two materials: two or more solids get dispersed in a solvent to form a homogeneous suspension and the solvent is evaporated, so that constituents progressively agglomerate.[120] It is a very simple method, but it requires to pay attention to many different parameters that directly influence size distribution and morphology, like size distribution of the starting materials, additives, mixing order, and solvents used.[121] Therefore, even if optimization is required, the simplicity of the method makes it highly attractive.[122]

Chemical vapor deposition (CVD) is a chemical method of depositing high-purity Si or C layer on substrate materials by decomposition of volatile substances over their surfaces applying high temperatures, even under plasma, to produce thin films.[123] This relatively simple method fabricates high-quality film with controllable thickness, and the technology exists and is already established for the deposition in many different morphologies and structures of both components.[124,125] The depositions are pure and uniform, at the nanoscale level, with strong bonds, however the method can be energy consumption.[31,94]

In this chapter we propose a mixed method of Chemical vapour deposition and liquid solidification techniques over free standing supports to build a C/Si hybrid material.

2.2 Materials and methods

2.2.1 Materials

Carbon paper (CP) foils (Toray Carbon Paper TP-090 untreated) were purchased from Quintech and cut in pieces with rectangular shape having dimensions in the range of 1x2.5cm before use. All other chemicals, i.e. silicon nanoparticles (Si, ≥98% with average size 50 nm, CAS number7440-21-3), hydrofluoric acid (HF, 48%, CAS number 7664-39-3, Sigma Aldrich), ethanol (CH_3CH_2OH, 96%, CAS number 64-17-5, Sigma Aldrich), were employed as-is, without any further purification.

2.2.2 Silicon nanoparticles pretreatment

Silicon nanoparticles (SiNPs) were surface cleaned from the silica layer by stirring them for 30 minutes in a 20%wt hydrofluoric acid solution in a mixture of water and ethanol 1:1 v/v. The solution was filtered off, while the solid residue was washed with ethanol, and dried under vacuum at 80°C. Finally, the SiNPs were re-suspended in ethanol by sonication, thus giving rise to a 4 gL^{-1} stable suspension.

2.2.3 Carbon Nanowalls

Carbon nanowalls were grown on carbon paper from CH_4 gas precursor in a hot filament plasma enhanced chemical vapor deposition chamber (HFPECVD). The substrates were introduced in the chamber facing the plasma generator with the gas mixture coming from the substrate's side parallel to the surface. A filament of 3mm of diameter made of graphite was heated over 2000 degree to obtain the plasma, while the chamber was pressurized at 25mbar with a mixture of methane and helium (3.5% CH_4 content) fed at 155 sccm. The substrate was heated up to 650°C after the chamber pressurization and the filament temperature was raised up around 2000°C.
Time of deposition was varied according to the desired thickness of carbon structures layer.

2.2.4 Hybrid Materials Fabrication

According to the desired final product, carbon paper underwent either (i) a 30-minute immersion in a Si NPs ethanol suspension, or (ii) a CNW growth in CVD as previously described. If necessary, the obtained first layer went through one or more subsequent steps overall alternating options (i) and (ii), and thus finally fabricating hybrid C/Si materials.
The pursued strategy of performing each step several times over the same samples alternating the CNW growth and SiNPs deposition allowed to obtain a library of multilayer materials as shown in Figure 2-4.
When the chemical vapor deposition is the first process of the synthesis in order to create a stable and thick conducive network the duration of the CVD growth was kept at 1h. Otherwise, then CNW were grown over Si NPS in order to maintain a high Si/C ratio, the process was stopped at 15 minutes.

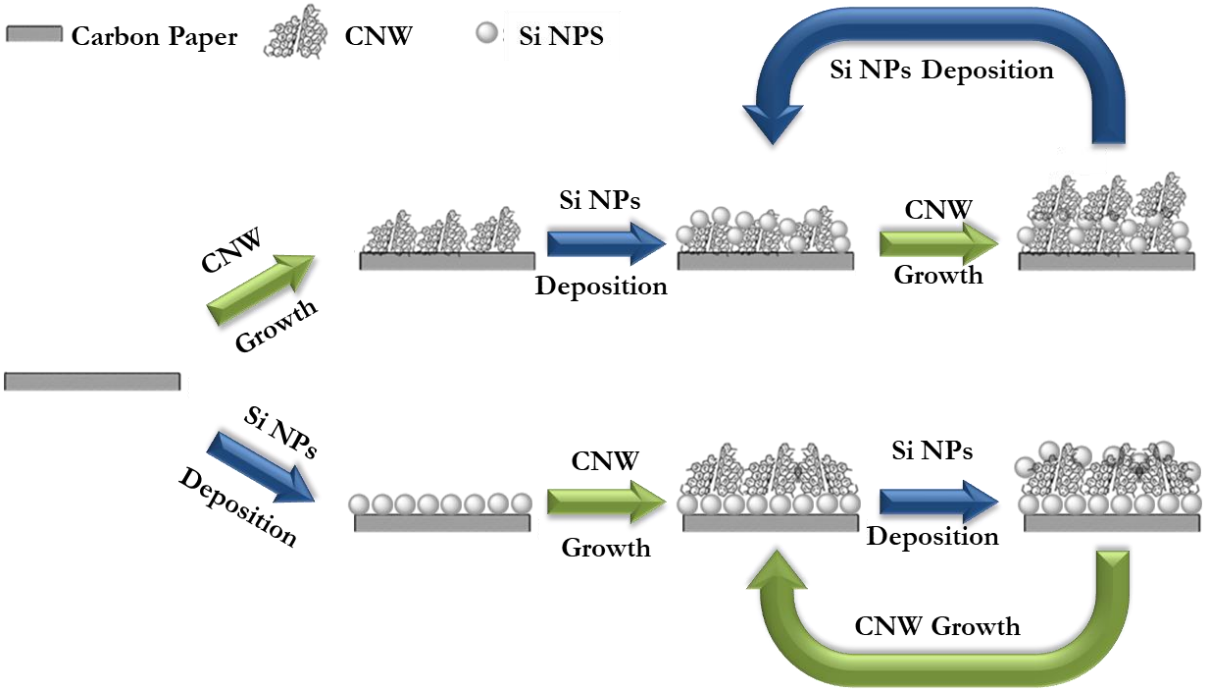

Figure 2-4 schematic representation of C/Si hybrid material synthetic steps

2.2.5 Characterization equipment

Field emission scanning electron microscopy (FESEM) and energy dispersive X-ray Spectroscopy (EDX) were performed using a Zeiss Auriga electron microscope.

X-Ray Diffraction (XRD) analysis for hybrid carbon/silicon electrodes was performed using a BRUKER D8 ADVANCE equipped with Mo tube (Kα 0.71 Å) in 2θ range 8-30°, with 40 kV voltage and 30 mA current.

Raman spectroscopy was performed with a Renishaw inVia Raman confocal Microscope using a green lamp (532.1 nm, output power 50 mW) and 100x lens, in the Raman Shift range between 200 and 3000 cm^{-1}.

Electrochemical performances were evaluated using a multichannel VMP potentiostat by Perkin Elmer Instruments and all samples have been studied in two-electrodes T-cells. Thanks to their free standing capability, samples of hybrid C/Si materials have been cut in circular shape, and used as such as anodes against metallic lithium with $LiPF_6$ 1M in EC:DMC 1:1 as electrochemical solution. These cells have been tested in the range 0.04-1.2V *vs* Li/Li^+.

2.3 Results and discussion

Hybrid C/Si materials analysed in this study are shown in Figure 2-5 and, besides from the support a, they are all materials where the first layer is made of a CNW growth. Materials with Si NPs deposition as the first step have been prepared and tested, however their electrochemical performances were lower than the samples proposed in Figure 2-5, therefore they are omitted from this dissertation.

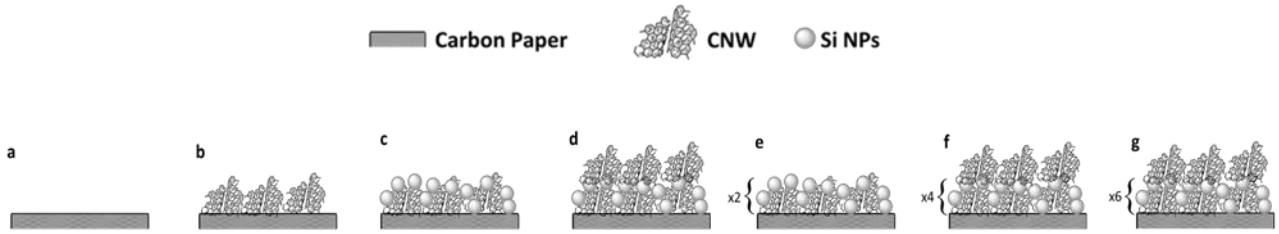

Figure 2-5 schematic representation of the proposed hybrid C/Si materials

The choice of carbon paper as starting support allowed to obtain free standing electrodes, which are highly desirable since they can be easily cut in the desired shape and dimensions for the final cell assembly (in this case, circular shape with 8 mm diameter). Moreover, since the carbon paper framework is conductive, it was possible to avoid both the use of adjuvant and producing an electrodic mixture via grinding or slurry. An image of a free-standing electrode of 8mm diameter is showed in Figure 2-6.

All samples from *b* to *g* have been obtained starting from a first growth of CNW over the surface of carbon paper substrate, while for samples from *c* to *g* at least one deposition of Si NPs followed. Samples *c* and *e* are characterized by an external layer of exposed and uncovered Si NPs. Samples from *d* to *g* can be considered multilayer materials, since they are made of more than one CNW or Si NPs layer.

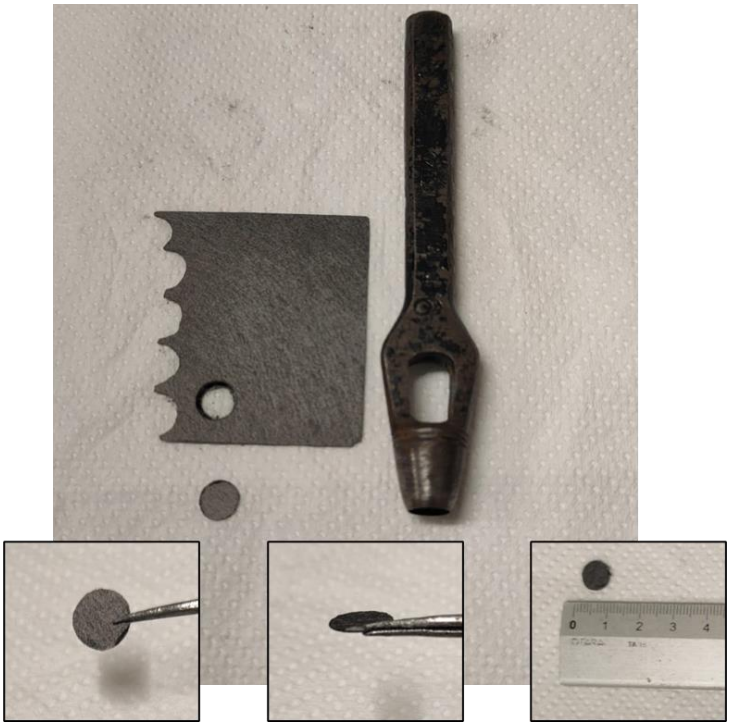

Figure 2-6 Free-standing electrode cut from a larger sample in a circular 8mm diameter shape.

2.3.1 C/Si Characterization

Carbon/silicon hybrid materials were studies by means of scanning electron microscopy coupled with EDX analysis to evaluate morphology of surface, dimension and geometrical properties of

carbon and silicon structure along with distribution and coverage of Si NPs and contact between CNW and Si NPs. XRD and Raman spectroscopy have been used to evaluate structure of both carbonaceous and silicon components in the electrodes.SEM images of four samples are shown in Figure 2-7. Figure 2-7a shows a fibre of carbon paper as it is. The framework formed by the ensemble of all the fibres constitutes the support for the successive deposition of CNW and SiNPs. An array of pristine CNW on carbon paper is shown in Figure 2-7b, where it is possible to notice that the walls of graphitic carbon are mainly distributed perpendicularly to the growth surface. Besides qualitative description, SEM micrographs have been used to evaluate the layer thickness, whose value has been estimated upon comparison of the average carbon paper fibre diameters before and after the growth: after 1h of CVD process using the abovementioned deposition conditions[124], a CNW layer of about 0.92±0.12 μm was obtained.

Figure 2-7c and Figure 2-7d are micrographs of electrodes *c* and *d* respectively. However, they can also be considered representative of all those samples having either Si NPs or CNW as the external layer, regardless of the number and stratification of the underlying materials. As it can be seen from Figure 2-7c, the silicon nanoparticles are homogeneously distributed all over the surface, with no evident tendency to agglomerate. This is probably due to the high surface area offered by CNW in fact, which allows Si NPS to distribute all over the carbon-based layer underneath without forming clusters, thus maintain free volume for future expansions. Nanoparticles smaller than CNW pores are able to diffuse inside the carbon matrix, while larger structures remain on the surface well accommodated and spaced by the vertical walls.

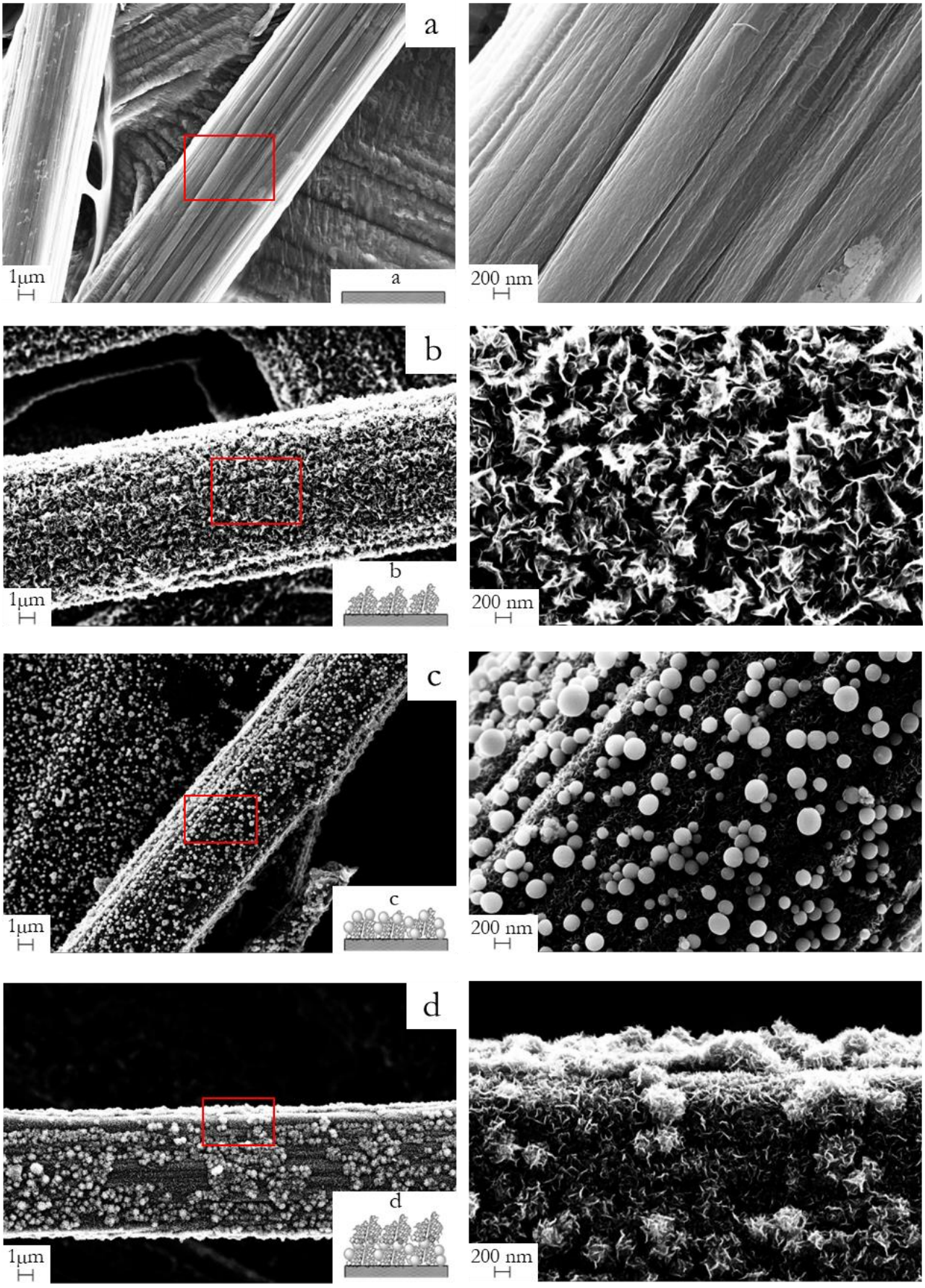

Figure 2-7 SEM micrographs at 10k magnifications of samples a) Carbon paper support, b) CNW growth over Carbon paper, c) Si NPs deposited over CNW matrix and d) a second growth of CNW over Si NPs deposited on the first growth of CNW

Figure *d* of Figure 2-7 shows a multilayer material made of CP-CNW-Si NPs-CNW subsequent layers. Despite having been exposed to the CVD harsh conditions necessary for CNW second layer growth, Si NPs still appear well distributed over the surface. Moreover, the second growth of CNW well embed Si NPs and the entire surface of the spheres is covered by the carbon matrix offering high portions of void for accommodation of Si expansions during lithiation.

The composition of samples on the surface has been studied by using energy dispersive X-Ray spectroscopy and results are shown in Figure 2-8. Since the electron beam energy was set at 15 KeV, the EDX spectra could gain information down to 1.9 µm under the surface, which means that this measurement is not representative of the entire sample, but only of a superficial portion. Nevertheless, the analysis was useful to evaluate the overall efficacy of the succeeding deposition of Si NPs.

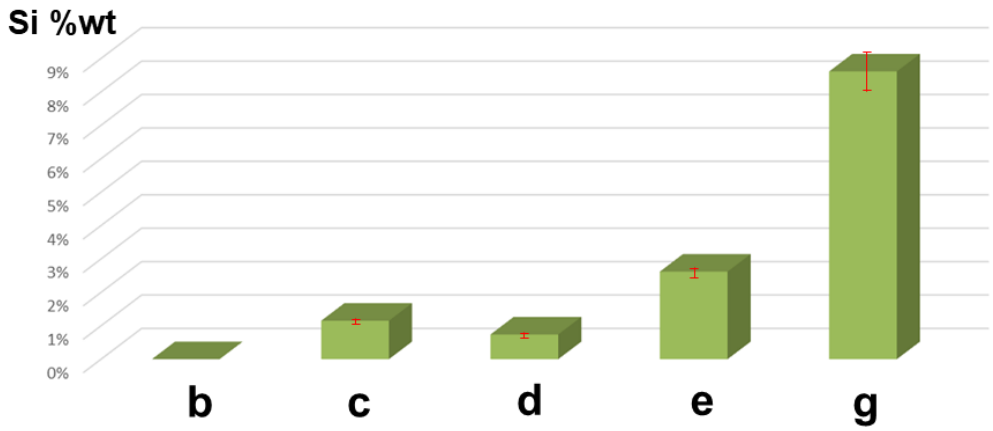

Figure 2-8 Si weight percentage in samples b, c, d, e and g, calculated by EDX spectra.

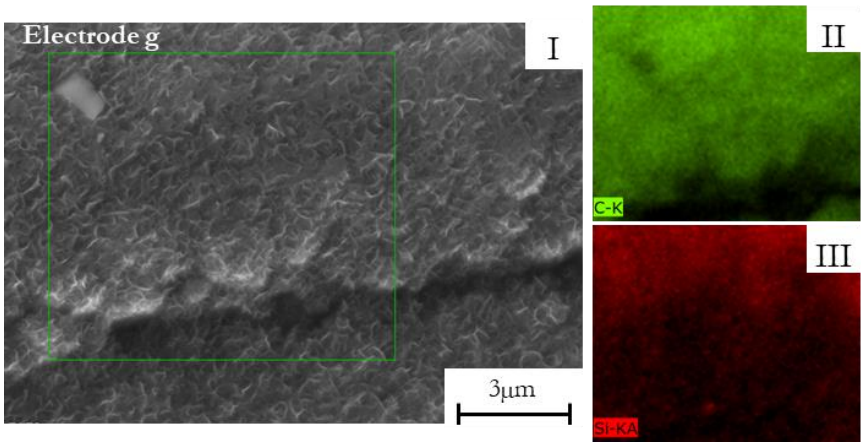

Figure 2-9 Carbon and silicon mapping over the surface of sample g: (I) The sample portion delimited in green shows the area to which the data are referred; (II)carbon distirbution; (III) silicon distribution.

Generally speaking, the amount of silicon increases from sample *b* to *g*. A single external layer of Si NPs gives (sample *c*) gives an amount of silicon weight percentage that roughly doubles when a second external layer is added (sample *e*). However, when the external layer is CNW, like in sample

d, Si %wt decreases, which might be due both to a partial detachment of the Si NPs during CVD high temperature and low-pressure process, or to a shield effect induced by the external CNW layer to the beam penetration. In any case, a multilayer material like sample *g*, made of 6 layers of CNW alternated to 6 layers of Si NPs and a final CNW layer on the top, shows a remarkably higher percentage of Si compared to all other samples. This result confirms that the proposed alternated fabrication method boosts the Si/C ratio while still maintaining high contact between CNW and Si NPs and the separation between Si structures.

In Figure 2-9I, II and III the EDX mapping of a portion of sample *g* showing the areal distribution of Kα signals of Si and C is reported: Si still appears homogeneously distributed under the C nanostructures even after many steps of deposition of Si NPs and growth of CNW.

XRD diffractograms of C/Si hybrid materials are show in Figure 2-10. The main component of all the proposed materials is graphitic carbon characterized by (002) peak at 12° and (004) peak at 24°. Silicon peaks are not visible for materials with low Si weight percentage content, since X-ray are penetrant radiation and the high crystallinity of graphite below the surface hinders the signals of nano-dimensional domains of silicon. However, Si (001) becomes visible as a weak signal in the samples richest in Si, namely d and *g*, thus demonstrating the crystalline nature of the Si structures.

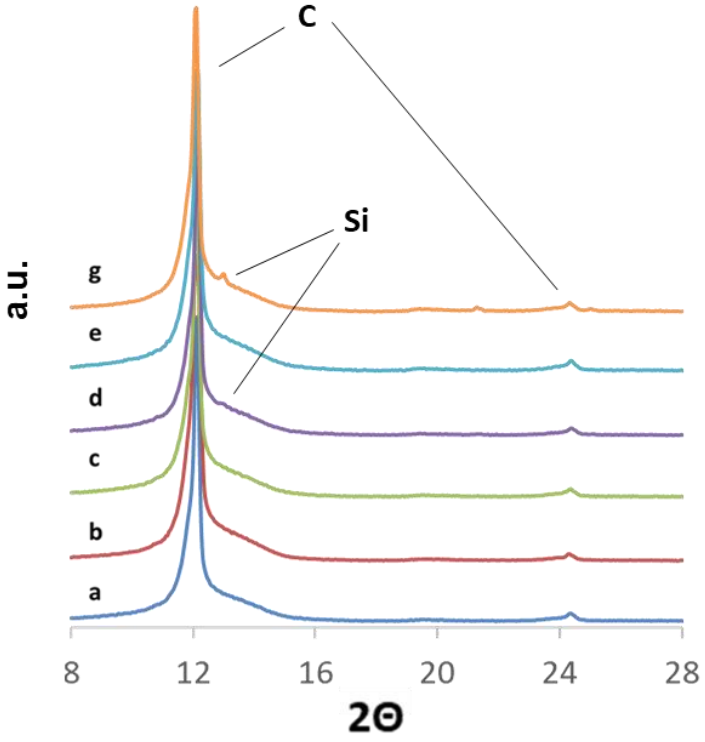

Figure 2-10 XRD diffractograms of different C/Si hybrid materials

Raman spectra have been collected to investigate the structure of the different components of hybrid C/Si electrodes, to observe modifications occurring during the synthetic process, and to evaluate changes in the orientation of C-C bonds and graphitization degree according to variation in the relative intensity of carbon bands. Raman spectrum of graphite-like materials is characterized by the so-called D-band, G-band and 2D-band. The D-band corresponds to disorder-induced Raman scattering, while the G-band is due to E2g phonon mode of graphitic carbon and represents a first-

order Raman scattering from the sp^2 hybridized carbon atoms in the graphene lattice. A high ratio of intensity of D-band over G-band indicates a high degree of disorder, while a low ratio shows a high level of graphitization. Values around 1 are typical of disordered graphite materials and imply the existence of short-range ordered carbon structures and only faulty long-range order. Finally, the 2D-band corresponds to a second-order Raman scattering from the double-resonance process involving phonons near the K point in the Brillouin zone. This peak is a result of the interactions between the stacked graphene layers. The shape and position of 2D-band and the ratio between the intensity of 2D-band and G-band can give indications about the number of graphene sheets in the carbon structure.

Spectra of samples a-g are shown in Figure 2-11, while Table 2-1 I_D/I_G and I_{2D}/I_G ratios of the investigated C/Si materials summarizes corresponding values of I_D/I_G and I_{2D}/I_G ratios. Pristine carbon paper support (sample a) shows very high graphitization degree with a ratio around 0.13 and a very low signal of D-band. On the other hand, sample b, made by growing CNW over carbon paper, shows a much higher disorder degree as suggested by the increase of intensity of its D-band and the I_D/I_G calculated ratio, which drops to 1.01. This indicates lower carbon crystallinity and graphitization of CNW compared to carbon paper.

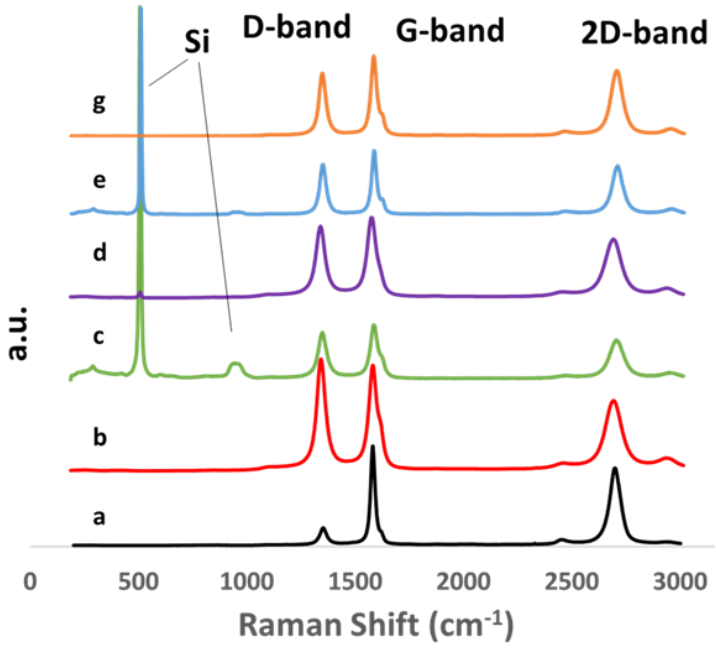

Figure 2-11 Raman spectra of different C/Si hybrid materials

	a	b	c	d	e	g
I_D/I_G	0.13	1.01	0.86	0.98	0.99	0.88
I_{2D}/I_G	0.66	0.66	0.77	0.69	0.83	0.77

Table 2-1 I_D/I_G and I_{2D}/I_G ratios of the investigated C/Si materials

Addition of Si NPs (sample *c*) increases the graphitization degree (i.e. lower I_D/I_G) and the subsequent growth of an additional overlapping of CNW layer seems to give a more graphitic carbon component

in comparison to the one obtained with the previous step. In other words, the presence of Si NPs seems to facilitate the growth of a more crystalline and graphitic CNW layer. This might be due to the interaction between Si NPs and the carbonaceous gas precursors in the CVD chamber. A different interaction between the gas and the adsorbing surface might induce the formation of a more graphitic and crystalline carbonaceous structure by providing different mechanism of nucleation for the growth of CNW and the alignment of successive precursors molecules. It has already been demonstrated that Si can act as a catalyst for CNTs growth by guiding the orientation and alignment of carbon atoms during synthesis[126] and here a similar mechanism could occur.
As shown in Table 2-1, in the analysed samples the I_{2D}/I_G ratio gradually increases along with the number of layers when the external layer is carbonaceous (samples *a*, *b*, *d* and *g*). However, it appears unexpectedly higher when Si NPs is the external layer (samples *c* and *e*). in fact:
On the other hand, the presence of Si can be clearly pointed out by a stretching peak around 520 cm^{-1} only when it is present as uncovered nanoparticles external layer (samples *c* and *e*). A second peak due to the bending of Si-OH on the external surface is shown around 970 cm^{-1}. However, the signal at 520cm^{-1} drastically disappears in samples protected by CNW layers, such as *d*.

2.3.2 C/Si electrochemical performances

Different C/Si have been tested in order to investigate the behaviour of the proposed anodes and the efficacy of both the CNW external layer protection and the addition of silicon layers over the carbon paper fibres. However, since the carbonaceous framework of carbon paper was too heavy respect to the other components, it was not possible to accurately evaluate the mass of Si NPs deposited on the electrodes. Moreover, all the components of the synthesized electrodes, i.e. carbon paper, CNW and Si NPs are capable of binding lithium ions, albeit through different mechanism, and therefore all components may contribute to the battery's performance. These factors result in the impossibility to properly determine a mass value and make the definition of the active mass very challenging. Therefore, a proper definition of gravimetric capacitance of the anodes was never achieved, nor it was possible to set a gravimetric current. For these reasons, a fixed current of 10mA was used for every sample in charge and discharge, and performance were expressed in terms of areal capacitance.

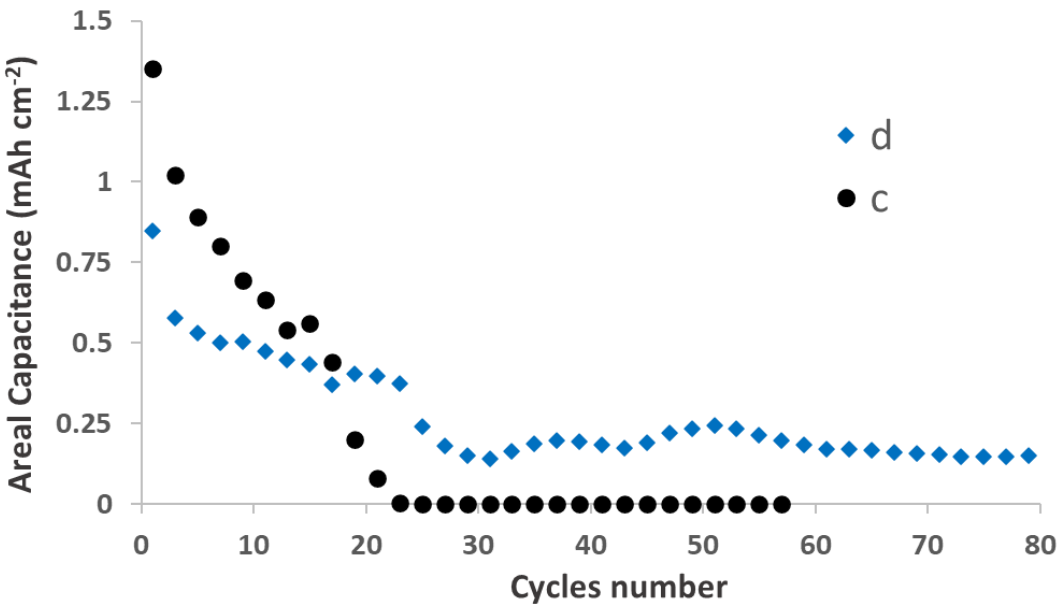

Figure 2-12 Behaviour of the areal capacitance of electrodes c (black dots) and d (blue diamonds) in lithium-ion devices in time

As it is possible to observe in Figure 2-12 Behaviour of the areal capacitance of electrodes c (black dots) and d (blue diamonds) in lithium-ion devices in time, for both *c* and *d* electrodes there is a significant capacitance loss from the first cycle to the second one due to the formation of SEI layer, and at least up to cycle 10. Mostly important the anode with uncovered Si NPs, even offering an initial capacitance higher than the anode protected by the CNW layer, no longer exhibits any activity after only 21 charge and discharge cycles. At the same number of cycle electrode *d* is still working, even facing a second loss in capacitance resulting in stabilization around 0.2 mAh cm^{-2}, and it seems to be still active even after 80 cycles.

Both electrodes were obtained through a process including a single step of silicon nanoparticles dip-coating, and the only difference is the presence of the CNW external layer in *d*. Therefore, the amount of silicon contained in the two anodes can be considered comparable, whereas the surface facing the electrolyte has a substantial difference. It can be concluded that the complete encapsulation of Si NPs is essential for these anodes to properly work and to stabilize at a certain capacitance value, even if it is just around the 20-25% of the capacitance showed in the second cycle.

By keeping the external layer of CNW, increasing the number of deposition stages and the amount of silicon in the anodes, an increase in areal capacitance is expected due the increase in the absolute amount of the active material.

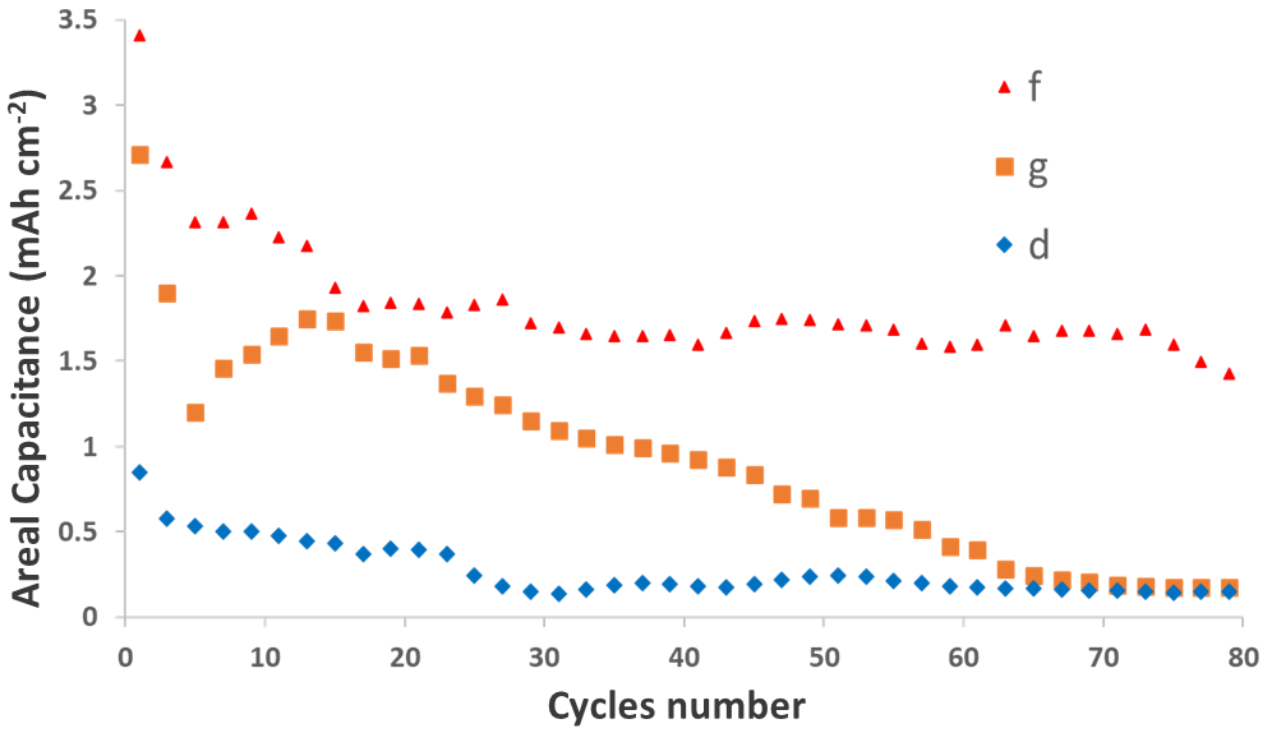

Figure 2-13 areal capacitance over time for electrodes c (black dots), d (blue diamonds), g (orange squares) and f (red triangles)

In Figure 2-13 areal capacitance over time for electrodes c (black dots), d (blue diamonds), g (orange squares) and f (red triangles)the areal capacitance as a function of the number of cycles of different electrodes having external CNW layer and different number of overlapped CNW-Si NPs internal layers (i.e. sample *d* one layer, sample *f* four layers, sample *g* six layers) are shown. that the reported curves indicate that there is an increase in the absolute capacitance of batteries, and this can be simply attributed to the higher amount of active material in samples.

However, it is worth noting that sample *g* even with two additional layers of Si NPs and CNW compared to *f*, actually has a lower areal capacitance. More in detail, both the samples *g* and *f* show an initial capacitance loss in the first cycles, and similar values around 15-20 cycles. However, electrode *g* capacitance quickly fades reaching values similar to those of electrode *d* after around 65 cycles. This unexpected and anomalous result could be explained by assuming that there actually is a mechanical limit in the layers of Si NPs and CNW that can be overlapped on electrodes. Apparently, there is a limit in the obtainable areal capacitance due to the fact that only a fraction of the layers are actually binding lithium-ions, and the quick fade of performances might be due to the detachment of some of the most external layers of active material from the surface. These hypotheses would explain both the similar values f electrode g and f in the cycle range of 15-20 cycle and the similar value of capacitance of electrode g and d after 65 cycles.

In any case, among all the samples, electrode *f* clearly shows the most promising behaviour, with a capacitance around 1.5 mAh cm^{-2} (i.e. 56% of the second cycle value) after 80 cycles. As shown in Figure 2-14 capacitance values as a function of cycle number for electrode f both in discharge (red triangles) and in charge (green triangles)electrode *f* is still working after 100 cycles and moreover

there is only a slight difference between charge and discharge capacities, with a coulombic efficiency close to 100%.

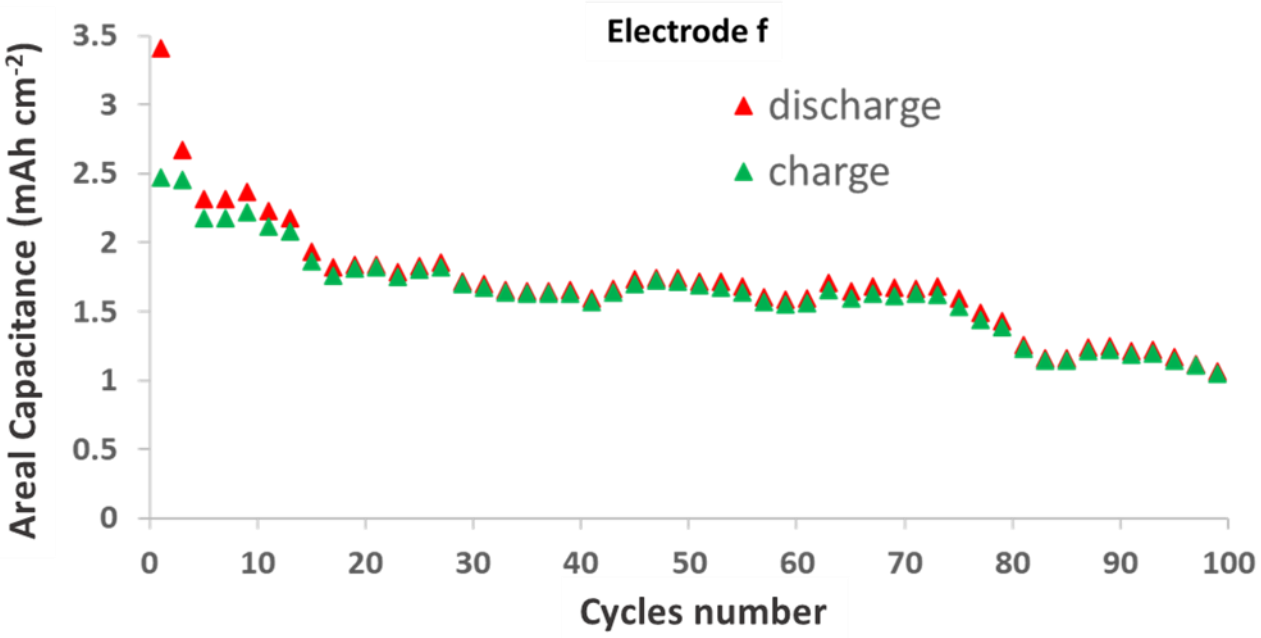

Figure 2-14 capacitance values as a function of cycle number for electrode f both in discharge (red triangles) and in charge (green triangles)

In order to better understand electrode *f* behaviour, the curve shape of the potential evolution during charge and discharge has been investigated for the first cycles. As it can be seen in Figure 2-15 evolution of potential during a single cycle of discharge and charge of anodes for cycle 1 (green line). 2 (orange line), 5 (grey line), and 10 (yellow line), the very first cycle is way longer than the subsequent ones and the curves clearly assume different shape during discharge. This is due to the SEI formation process that occurs in the first discharge that, because of its irreversible nature, makes the coulombic efficiency of the charge always consistently lower than in the following cycles.
Moving from the second to the 10^{th} cycle it can be noticed not only that the duration of cycles is lowering, which means capacitance is fading, but also that there is an increasing of irreversible loss at the beginning of every charge, which can be noticed from the increase in the potential occurring immediately after discharge ends.

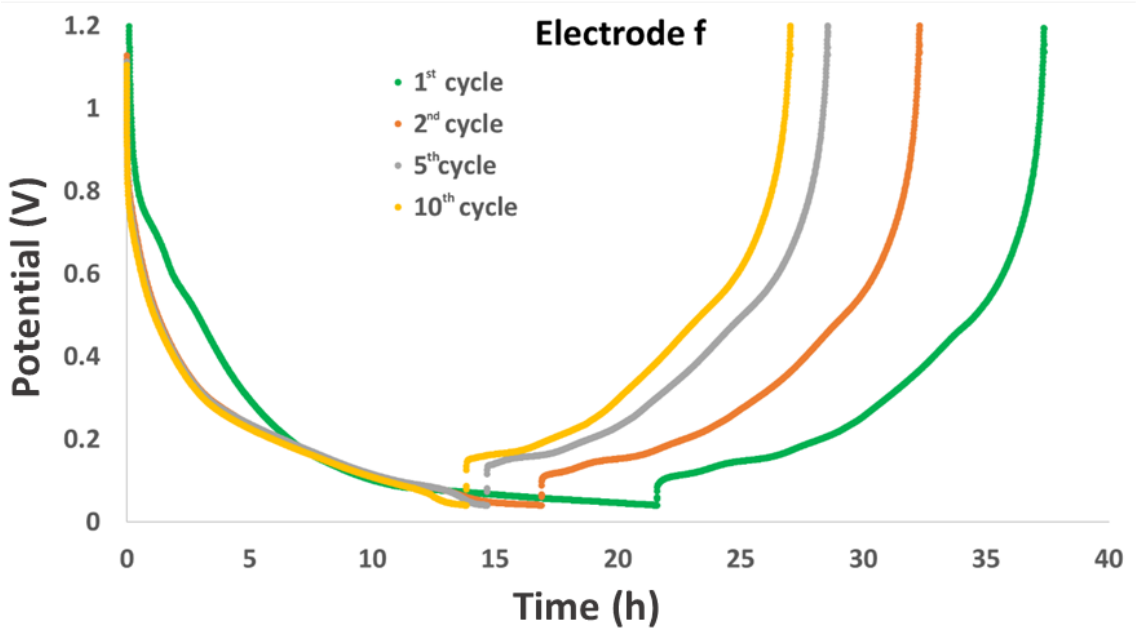

Figure 2-15 evolution of potential during a single cycle of discharge and charge of anodes for cycle 1 (green line). 2 (orange line), 5 (grey line), and 10 (yellow line)

2.4 Conclusions

In conclusion, despite the limitations shown in the impossibility of accurately determining the active mass of the electrodes, this study has demonstrated the effectiveness of CNW coating on the underlying layers of silicon. The multilayer materials have also shown how adding active material on top of pre-existing layers of covered Si NPs (Silicon Nanoparticles) can bring benefits to the amount of charge that the electrodes can provide during discharge. Furthermore, during these investigations we could observe how there is a limit beyond which the underlying layers no longer contribute beneficially to the overall operation of the device

3 Carbon aerogel from rice husk for supercapacitors

In this chapters a facile way to build a light, stable and highly conductive CAs made of cellulose purified from rice husk is showed. The synthetic process will involve a two-step pre-treatment with commercially available reactants followed by the three main steps of CAs fabrication: gelification, drying and pyrolysis.[127–130]

As a proof of principle, the application of the CAs obtained from the developed low-cost process as electrodes for capacitors and lithium-ion batteries is presented, thus evaluating the potentialities of the recycled material in a possible second life.

3.1 Introduction to Carbon Aerogel in electrochemical applications

3.1.1 Green chemistry and circular economy

Green chemistry nowadays is experiencing tremendous progress, and the economy and production sectors are moving towards the exploitation of renewable feedstocks [131–133], the improvement of resource efficiency [134], and the recycling and reuse of materials [135,136]. These pushes towards a more virtuous economy and production model drives global efforts towards a sustainable future [137,138] with support and patronage of political institution, like for example the new EU Circular Economy Action Plan.[139]

In the present world sustainability can no longer be separated from development of materials, and it is true also for efficient energy conversion and storage systems, this includes both design and production of new or alternative materials [140,141], advancement of technologies [142–144], and geometrical optimization [145,146].

In any case the combination of balanced energy technologies and green processes development certainly represents a landmark, that offers the prospect to eventually reduce the fossil fuel utilization [147] and to exploit secondary raw materials, that could be industrial [148,149] or agricultural wastes, and biomasses [150,151].

Actually, Waste management represents not just an environmental and economic critical point of future sustainability, but it is also recognized to be a social and political priority area, especially in megacities and in developing countries where urban populations are the most affected by waste management. The most usual social effects are air pollution, flooding, and impacts on the public health.[152–154]

A pure linear approach to economy where raw materials are promptly directed towards use and waste is no longer sustainable and a different model, a circular economy model aimed at the continual use of resources while eliminating waste must be adopted.[153,155] Circular economy attempts to improve the environmental impact and economic value of existing production and waste management systems through reuse, recycling, recovery, redesign, and remanufacture.[152,153]

A schematic idea of this model is shown in Figure 3-1. Such a model is oriented toward slowing down, limiting, or terminating resource loops and reducing the exploitation of limited natural resources in a series of efforts that moves towards sustainable economy.[156] The inevitably slow

evolution of actual economic systems towards a circular approach is done by balancing economic, social and environmental, values.[155,157] According to Ellen MacArthur Foundation the transition to circular economy is linked to a 12% higher gross domestic production (GDP) growth and a reduction of carbon dioxide emissions by 83% in Europe by 205. 0[158]

Figure 3-1 Schematic representation of a circular economy model

Therefore, Circular business models are quickly gaining attraction in light of a sustained and advocated transition to a more sustainable economic model.[159] However, the transition still involves running and jumping over barriers in a fast-changing worldwide scenario driven by aggressive targets and investments, it takes time and resources and often has to face the implicit limitations that this model actually has.[152,160] The idea of actually obtain a zero-waste approach can only work theoretically.[160]

For examples, limitations in material properties and manufacturing technologies constitute impediments for closing material loops along with inevitable dissipation in the environment of resources wastes, contamination.[161–163] Often authors, scientists and in general social figures falls short of acknowledging and fully addressing the complexity of waste both in fabrication process than in economy since recycling markets are actually unpredictable and display high degrees of volatility.[164,165]

In any case, despite all the limitation and even issues that even circular approach can offer, there is no doubt that actual economy has to change and that worldwide there's plenty of non-toxic wastes still waiting to exploit their added value, like agricultural wastes and biomasses.[166–168] Since the aim

of this chapter is to develop carbon aerogel-based electrodes, biomasses constitute a huge library of possible secondary raw materials.

The considerable amount of different possibilities, among these virtuous eco-friendly sources of carbon each one with different morphology and structure at micro- and nanoscale, result in versatility and potentiality of use in a variety of fields, from catalysis [169] to energy conversion and storage. [170,171] The latter application is particularly noticeable for this study.

3.1.2 Rice Husk

The main component of biomasses (average content of 33% wt) is cellulose; its natural abundance, together with renewability and biodegradability, make it the ideal green precursor of carbon-based products [172–175]. Among the others, a promising and appealing biomass as source of cellulose for electrochemical applications is the outer covering of the rice kernel, i.e. rice husk (RH). It has been estimated that for every 5 tons of rice produced almost a ton of RH remains from the process.[87] Considering that the annual world rice production is about 600 tons, it is clear that RH is an inexpensive and abundant waste whose efficient recycling and conversion in high-value products would represent a virtuous purpose.[176,177]

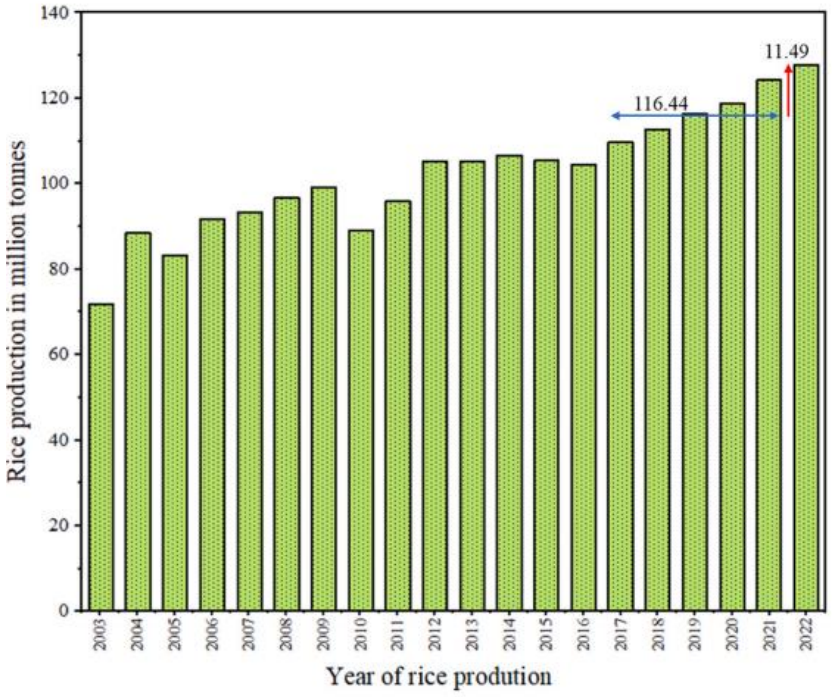

Figure 3-2 Rice production in India over the past two decades taken from figure 1 of Jyothsna et al.[178]

Dried RH is mostly made of cellulose (≈38% wt), lignin (≈22% wt) and hemicellulose (≈18% wt), besides silica (≈20% wt) and few other with trace amounts of other components, mostly oxides, like K_2O, but also CaO, Na_2O, MgO, and Al_2O_3.[179] However, the composition of RH matrix is actually very variable, being linked to a large number of factors, like growth process, geographical origins, age, harvesting or storage process, exposure to fertilizer, pesticide or even pollutants.[179–181]

Actually, RH has been exploited as starting material for design and production of carbon-based structures for energy applications, e.g. biochar, carbon capture, fabrication of electrodes for lithium-

ion batteries (either as such and in composites with silicon), capacitors and supercapacitors (see Figure 3-3 from Soltani et al.[182]).[183–186] It is a very promising and interesting application is in lithium-ion devices thank to the rich content of silica. The presence of silica in RH is due to a process called biosilicification: absorption of $Si(OH)_4$ or $Si(OH)_3O^-$ from soils to generating complex and hierarchical nano-structured silica frameworks between the cell walls [179,187,188] The presence of silica layers in the form of silicon–cellulose membrane between the cell walls provides a protective barrier to the rice kernel against the attack of microorganism against the rice grain.[187,188]

Figure 3-3 Schematic representation of possible applications for RH, image taken from figure 5 of Soltani et Al.[182]

In any case, these chapters will focus on pure carbon electrodes obtainable from RH not just for lithium-ion devices but also for supercapacitors application. It is worth notice that such materials can successfully fabricated by RH, and more in general from biomasses and carbon sources, in many different forms of carbon, such as graphene, graphene oxide and nanotubes, either pristine and in hybrid structures coupled with metals or other materials [55,189,190]. Among this wide library of material, Carbo Aerogels (CAs) have been chosen.

3.1.3 Carbon Aerogel

Carbon aerogels (CAs) proved to be particularly interesting among the possible carbon-based materials, since they seemed to offer the opportunity to fabricate electrodes for electrochemical devices with remarkable efficiency.[191,192] They were first fabricated in 1980s CAs gathered attention thanks to outstanding physical and chemical properties, i. e. low density, chemical stability, high

specific surface and a 3D porous structure which derive from the network of interconnected particle of aerogel microstructure.[128,193–195] Moreover, CAs show high conductivity, temperature resistance, and acid/alkali resistance. This peculiar set of features makes such material suitable and versatile in a broad area of applications. In fact, besides electrochemical devices, they have been applied in many different sectors, like mechanics to electricity and even heat transfer, or as adsorbents and supports for catalysis [195–198]. A few of these applications along with a resume of CAs most interesting properties are shown in Figure 3-4 taken from Gan et al.[199]

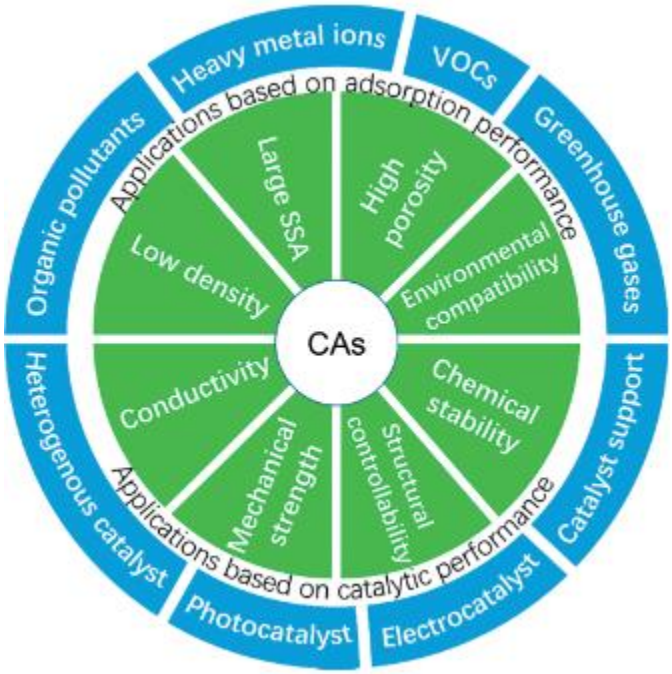

Figure 3-4 Schematic illustration of properties and possible applications for CAs, image taken from figure 2 of Gan et al.[199]

CAs can be obtained from different precursors such as organic monomers, biomasses, polymers or carbon nanostructures like graphene or nanotubes, but regardless of the starting material, they are usually prepared in three steps, i.e. gelation, drying and carbonization. [129,193,194,200] These generic steps are showed in Figure 3-5 taken from Yu et al. [193]

Gelation is the transformation of a sol precursor to a gel, no matter the nature of the precursor used. It includes different processes and reactions in solution, since the nature and the steps of the mechanisms can vary according to the precursor, but usually it involves passages of polymerization and cross linking of chains. [201,202]

Drying passage, on the other hand, is crucial for the fabrication of CAs, it is the most important to maintain a highly porous final material since it must be conducted avoiding that solvent removal could lead to excessive shrinkage and collapse of the network.[203] Simple vacuum drying must be avoided and alternative supercritical and freeze drying must be considered, since they guarantee a limited shrinkage of a well-aged gel and the preservation of hierarchical pore structures.[193,204] Since Freeze drying is usually performed with a lower cost experimental apparatus and is, in general, simpler than supercritical solvents use, it is preferred, and it was chosen for this study.[205]

The final synthetic passage of carbonization in controlled atmosphere (usually inert using Ar or N_2) removes the non-carbon volatile components that could be present in different elemental nature and relative quantities according to the carbonaceous precursor.[193] During this process many of the final properties of CAs are tailored (final porosity, pore volume, surface area).[206] It is a very important step and the control over the temperature of the process is crucial, it must be in a range between 600 and 900°C, since a temperature below this range won't allow to create a proper 3D porous network, while above this ranges the porous structure might collapse.[199]

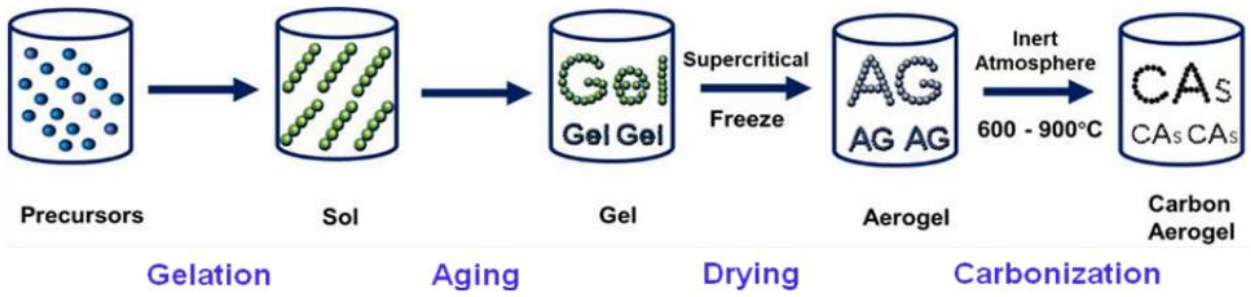

Figure 3-5 schematic representation of a generic synthesis for carbon Aerogel taken from figure 2 of Yu et al.[193]

In this study, in a view of valorisation of an agricultural waste and approach to a model of virtuous use of resources, a CAs made from cellulose chains purified from RH has been successfully prepared and its use as electrodes both in symmetric supercapacitors and lithium-ion devices have been studied.

3.2 Materials and methods

3.2.1 materials

Rice Husk was purchased by LD Carlson Co. and was finely ground before use. All other chemicals, i.e. sodium hydroxide (NaOH 98.5%, CAS number 1310-73-2, Sigma Aldrich), acetic acid (CH_3COOH 99-100%, 99-100%, CAS number 64-19-7, Sigma Aldrich), sodium chlorite ($NaClO_2$ 80%, CAS number 7758-19-2, Sigma Aldrich), potassium hydroxide (KOH 90%, CAS number 1310-58-3, 90%, Sigma Aldrich), polyvinylidene difluoride (PVDF 100%, CAS number 24937-79-9, Sigma Aldrich), and urea (NH_2CONH_2 99-100%, CAS number 57-13-6, Carlo Erba) were employed as-is, without any further purification.

3.2.2 Synthesis of Carbonaceous materials

Cellulose Extraction

Cellulose extraction from RH involved a two-step pretreatment. In the first step, the removal of lignin and a portion of hemicellulose was carried out by immersing the initial matrix in an aqueous solution containing 1.7% wt sodium chlorite and 3.36 gL^{-1} acetic acid, maintained at 80°C for one hour with magnetic stirring. The RH to solution ratio was 1 g: 17 mL, and this process was repeated four times. Following each iteration, the solid residue was separated using qualitative filter paper,

rinsed with distilled water until reaching a neutral pH, and then dried in an oven at 110°C until constant weight.
Subsequently, the resultant product was treated in 1 M NaOH (ratio 1 g: 8 mL) at reflux for one hour, under magnetic stirring, to eliminate silica, as well as other inorganic impurities and the remaining hemicellulose. The final residue was filtered using qualitative filter paper, washed with distilled water until neutral, and dried in an oven at 120°C until a constant weight was achieved.
These two pretreatment sequences were conducted in either the stated order (hereinafter Route 1) or in reverse order (hereinafter Route 2).

Cellulose Gel and CA Formation

The cellulose pulp purified as previously described was added to a 7% wt NaOH and 12% wt urea aqueous solution in ice bath to get a final concentration of either 2%wt or 7%wt of cellulose. The mixture was magnetically stirred at 0°C until complete dissolution was achieved, then the product was aged at 50°C overnight or until a stable cellulose gel was formed (i.e. until the supernatant removal and formation of a cohesive, gelificated cellulose-based structure). Approximately 1.2 L of distilled water for each starting gram of cellulose were used to complete regeneration and the gel was then freeze dried at -50°C for 5 hours. Finally, the cellulose dried gel was carbonized under Ar atmosphere at 800°C for 2 h in a tubular furnace, thus producing CAs.
In order to better recognize the CAs samples obtained by following either synthetic Route 1 or 2 at either 2%wt or 7%wt concentration of cellulose, hereinafter samples will be indicated according to Table 3-1, where the number indicates the synthetic pathway and the letter indicates a smaller or higher concentration of cellulose.

Synthetic pathway	Cellulose concentration in gel	Name
Route 1	2%wt	**1A**
Route 1	7%wt	**1B**
Route 2	2%wt	**2A**
Route 2	7%wt	**2B**

Table 3-1 CAs samples name assignation

3.2.3 Characterization

Field emission scanning electron microscopy (FESEM) and energy dispersive X-ray Spectroscopy (EDX) were performed using a Zeiss Auriga electron microscope
Meanwhile XRD for cellulose based materials was performed using a Philips PW1830 APD3520 diffractometer using Cu-Kα radiation (λ 1.54 Å) in 2θ range 8-40°, with 40 kV voltage and 30 mA current.
Raman spectroscopy was performed with a Renishaw inVia Raman confocal Microscope using a green lamp (532.1 nm, output power 50 mW) and 100x lens, in the Raman Shift range between 800 and 2200 cm^{-1}.

Brunauer Emmert Teller (BET) method was used using a Quadrasorb SI instrument from Quantachrome.
X-ray tomography was performed using a 3D Sub-micron X-ray resolution microscope Zeiss Xradia Versa 610 both in absorption and phase contrast mode. For absorption experiments, 2401 projections were acquired with a 4x objective, 4 s of exposure time at 40 kV and 3 W, pixel size of 3.5 µm. For phase contrast measurements 2401 projections were acquired with a 20x objective, 80 s of exposure time at 40 kV and 3 W, pixel size of 0.7135 µm. Both experiment settings used air as filter for the X-rays. The reconstruction of dataset was performed using Zeiss Scout-and-Scan Control System Reconstructor, whilst 3D models of the samples were investigated and processed with software Dragonfly Pro from Object Research Systems (ORS).
Electrochemical performances were evaluated using a multichannel VMP potentiostat by Perkin Elmer Instruments and all samples have been studied in two-electrodes T-cells. Carbonaceous electrodes based on CAs were fabricated by mixing active material, PVDF and acetylene black (80:10:10) and assembled both in symmetrical configuration for supercapacitors and against a counter electrode of metallic lithium for lithium-ion batteries. In supercapacitor application, aqueous solutions were used as electrolytes and galvanostatic cyclations and cyclic voltammetry tests were performed in -1.0 – 0.2V potential window respectively at different currents (0.1 – 1.0 $A \cdot g^{-1}$) and potential scan rates (1-50 $mV \cdot s^{-1}$). In batteries test galvanostatic cyclations in the range 0.04 – 3 V have been observed.

3.3 Results and discussion

3.3.1 Synthetic steps

Synthetic strategy developed for CAs and CD involves a two-step pretreatment aimed at the purification of cellulose. Both passages are performed in aqueous solution employing common low value chemicals. Each sequency of the two steps has been analysed in order to investigate the different outcomes in terms of morphology, structure and performances of the final products. Yields reported are calculated by gravimetric measurements before and after each process.

Route 1: delignification + desilication pretreatment

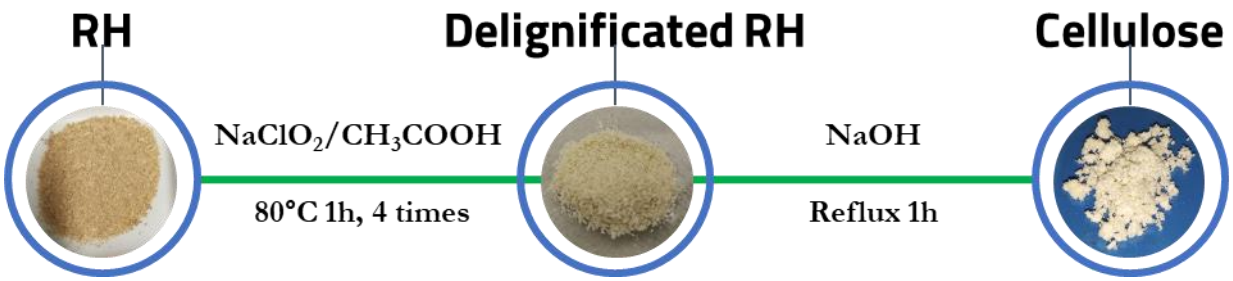

Figure 3-6 schematic representation of cellulose purification during Route 1 synthesis

Route 1 passages are shown in Figure 3-6. The first passage of delignification is widely known as bleaching and the resulting materials appears as a powder whiter and less rigid than the starting

rice husk. The final yield after this step is around 67.0%wt, which is consistent with the content of lignin and hemicellulose in the starting matrix. All Yields are average obtained after, at least, three repetitions of the same procedures.

The second step of pretreatment in Route 1 is aimed at extracting silica and the residual hemicellulose. The final product will assume colour and characteristic of white cotton-like cellulose flakes with a yield of 48.9%wt, indicating a yield from starting material around 32.8%wt which is consistent with the cellulose content range in RH according to literature.[170,179]

Route 2: desilication + delignification pretreatment

Route 2, as shown in Figure 3-7 involves the same passages of delignification and desilication but with a different sequency. During the step of silica removal, a brown powder is produced with a yield of 53.7%wt, which is in good agreement with a removal of silica and hemicellulose.

A second step of bleaching was performed with a yield of 68.8% and a final product of flakes of cellulose smaller than samples obtained following Route 1. The average final yield is 36.9%wt, which is compatible with the range of 32-38%wt described in literature.

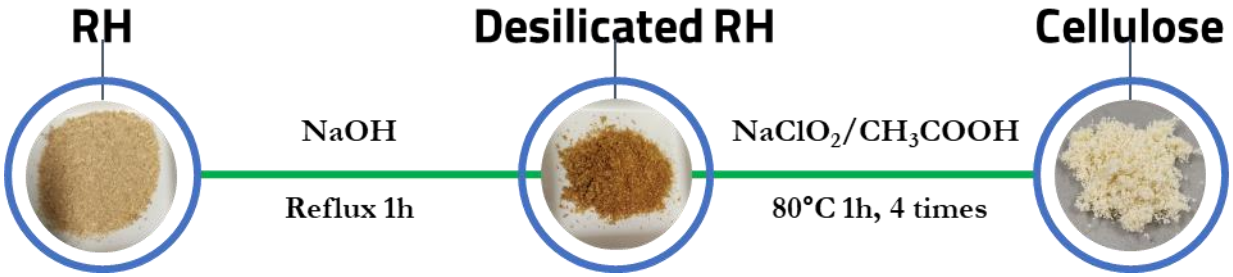

Figure 3-7 schematic representation of celulose purification during Route 2 synthesis

Gel Formation

Each cellulose was dissolved in a aqueous solution of urea and sodium hydroxide at two different concentration of cellulose (2%wt and 7%wt with respect to the dissolving solution) in order to make a gel according to Figure 3-8. Sodium hydroxide swells the clusters of fibres in order to make them more accessible for the dissolution role of urea that brings the polysaccharidic chains in solution. After complete dissolution the dark yellow solution obtained is left aging and the hydrogel is formed with the reordering of fibres in an interconnected framework. During the process of regeneration in distilled water the gel appears whiter and whiter after every passage along because of the removal of urea and sodium hydroxide from its fibrotic framework. Once the gels are frozen and freeze dried the final product appears as a white rough solid aerogel that must be carbonized in a short time in order to avoid structural collapsing of the framework.

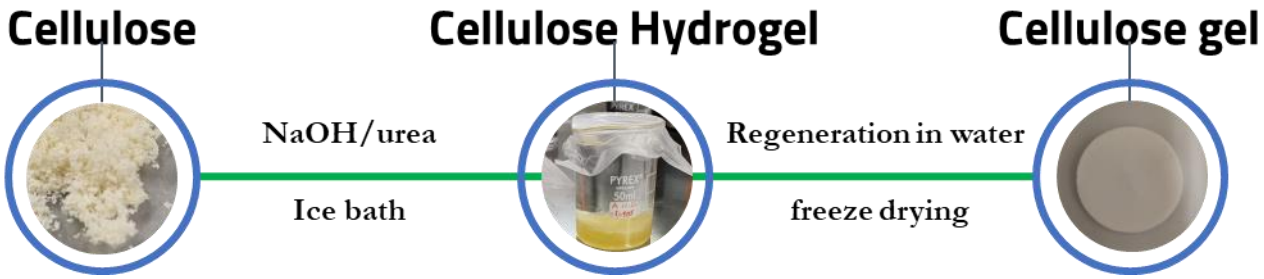

Figure 3-8schematic representation of celluose gelification and freeze drying

The yield of gel, with respect of the amount of cellulose used, for both concentration and route is around 86.8%wt, which means part of fibres are lost during regeneration process. Average density of gels, calculated by measuring its mass and calculating the volume assuming a cylindrical shape and thus taking into account only diameter and height of the disk gel, is around 92.7 $mgml^{-1}$. Average density for Route 1 (95.2 $mgml^{-1}$) appears slightly bigger than density calculated from Route 2 (89.6 $mgml^{-1}$).

Carbonization

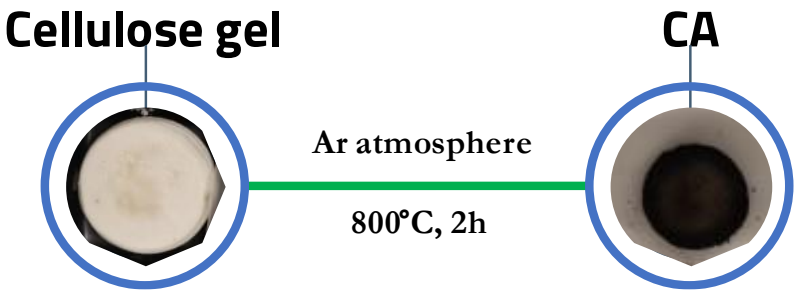

Figure 3-9 schematic representation of cellulose carbonization and CAs formation

As shown in Figure 3-9, after freeze drying the cellulose gels are transformed into an ordered matrix of carbon fibres by mean of carbonization. During this step, the organic and volatile components are removed by degradation and evaporation, while the residual material becomes a high conductive aerogel. CAs appears as black soft matrix of carbon fibres with a significant shrinking in volume.

Average yield, volume shrinkage, and final density of the 4 different CAs obtained upon combination of the two different pre-treatment pathways and the two different cellulose concentrations for gel formation are shown in Table 3-2. Yield is calculated with respect to the starting RH used, while density has been calculated as previously indicated for cellulose aerogel. Volume shrinkage is the ratio in percentage between the volume of CA and the volume of the cellulose aerogel that was carbonized. Apparently, higher cellulose concentration brings higher yield with lower volume shrinkage and densities. On the other hand, a comparison of samples obtained by using the same cellulose concentration, but different synthetic pathways shows that Route 2 results in higher shrinkage and density.

Sample	Yield %	Volume Shrinkage %	Density (mgml^{-1})
1A	4.92	73.64	44.7
1B	5.22	58.23	41.4
2A	3.22	84.04	51.6
2B	5.94	61.71	43.5

Table 3-2 Yield, volume shrinkage and density of the four CAs samples obtained

3.3.2 CAs Structural and Morphological Characterization

Every sample, as well as every intermediate step after each synthetic passage, has been studied with advanced characterization techniques in order to investigate structure, morphology and properties both at the final stage and during the synthetic pathways in order to analyse the evolution of final products through time.

SEM/EDX

Rice husk as well as every final material and every intermediates of the processes were observed with a scanning electron microscopy to determine the starting matrix morphology and it composition by means of EDX.

Rice Husk

In Figure 3-10 it is possible to see, in the insert a, the morphology of the outer shell of rice husk, which is richer in silica content concentrated around the aligned cells that form the RH assembly, giving structural resistance to the entire matrix. In insert b the inner wall of RH appears smoother with lower amount of silicon. Since RH has been ground into a fine powder, in order to make assumption about the evolution of our products, an average composition has been estimated from EDX data (and visible in Figure 3-21).

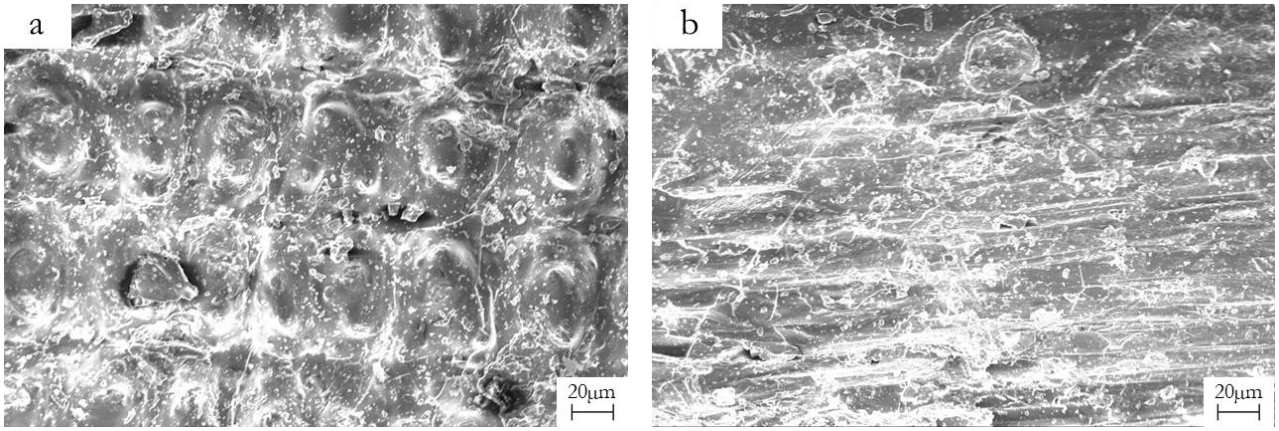

Figure 3-10 SEM micrographs of a) outer face of rice husk fragment, b) inner portion of rice husk fragment

Cellulose Synthesis Route 1

Following Route 1 RH gets bleached and lignin and part of hemicellulose is removed. In fig. X two images can be seen, the first one (Figure 3-11a), taken at the same magnification of RH SEM micrographs, showing the external shell of bleached RH and a second insert at higher magnification

(Figure 3-11b) of details on the surface of RH shell. The surface appears smoother and cleaned from organic components that were making difficult to take clear images, Figure 3-11a appears much more vivid than the bright surface of Figure 3-11a and b, where organic components charged the surface giving excessively high brightness and made impossible to collect clear images at higher magnification. The cleaned surface appear still intact with no fragmentation and silica seems to maintain together the aligned cells on the outer wall.

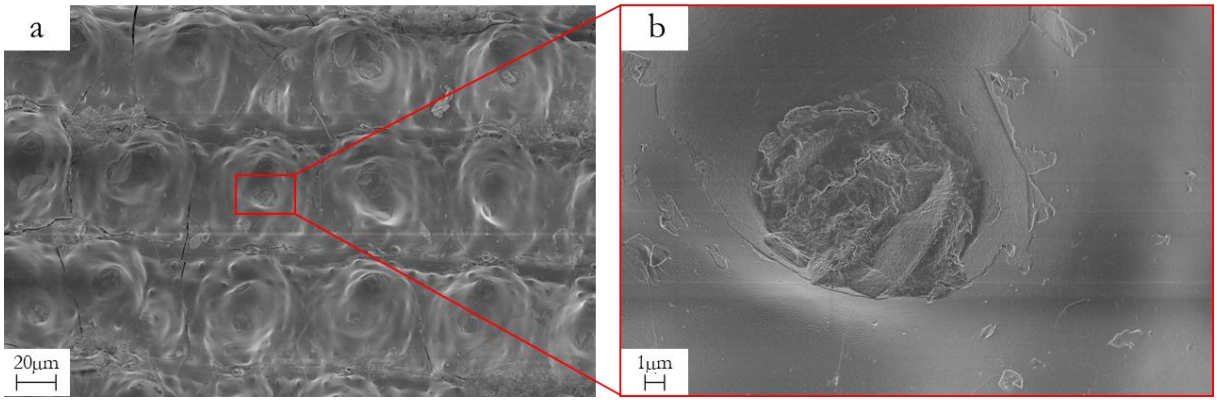

Figure 3-11 SEM micrographs of a) a portion of bleached outer walls of rice husk with b) a magnification of the center of one of the cells that form the Rice Husk shells

Cellulose obtained from Route 1 is collected after sodium hydroxide treatment on samples in Figure 3-11 and SEM micrographs are shown in Figure 3-12. The morphology is composed of mainly two kinds of structures, namely platelets and fibres. Platelets are thin wide sheets of cellulose that probably derived from the still intact shells of rice husk, as shown in Figure 3-12a,b and c. Fibres, on the other hand, are fibrotic structures that are formed by cellulose fibrils during NaOH leaching with an average diameter, measured by ImageJ software, around 5.6±0.5 µm (Figure 3-12d, e, f). In both these structures, platelets or fibres, the surface investigated at higher magnification (Figure 3-12c and F) reveals they are made of smaller fibrils joined in a porous structure.

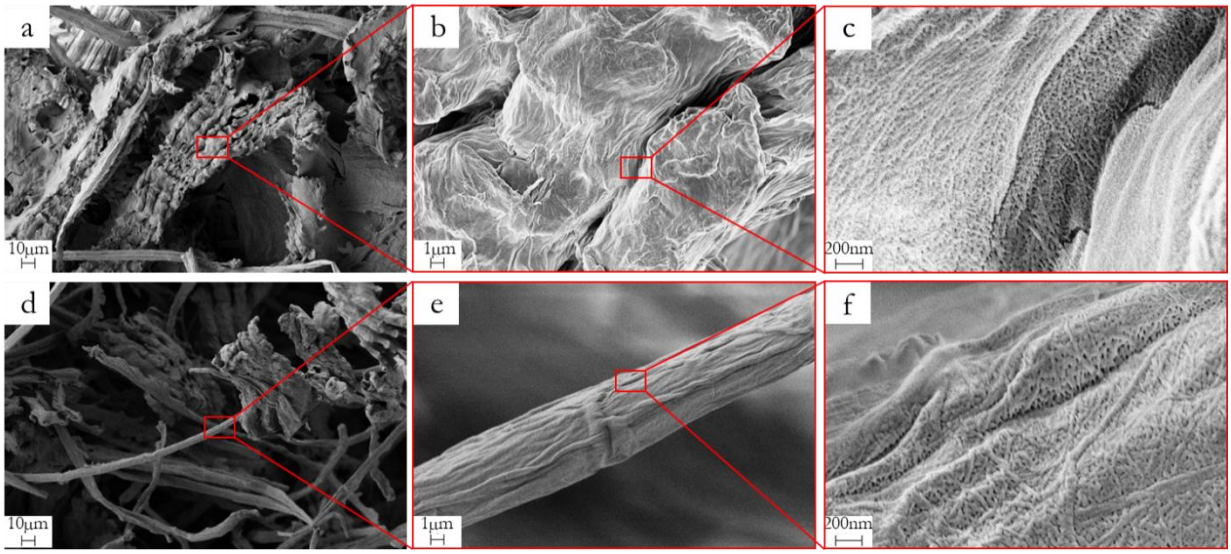

Figure 3-12 two sets of three subsequent magnification (a-b-c and d-e-f) of cellulose obtained from Route 1 SEM micrographies

Cellulose Synthesis Route 2

When Route 2 is followed, on the other hand, as shown in Figure 3-13, the desilification of RH due to NaOH leaching induces ruptures all over the surface. The micrograph at lower magnification (Figure 3-13a) shows that even if the main structural integrity is maintained, the morphology of the sample is deeply modified by the removal of silica from the interconnective area of cells, and many cracks (Figure 3-13b), mainly perpendicular to the orientation of the husk, are opened and edges appear frayed and rough.

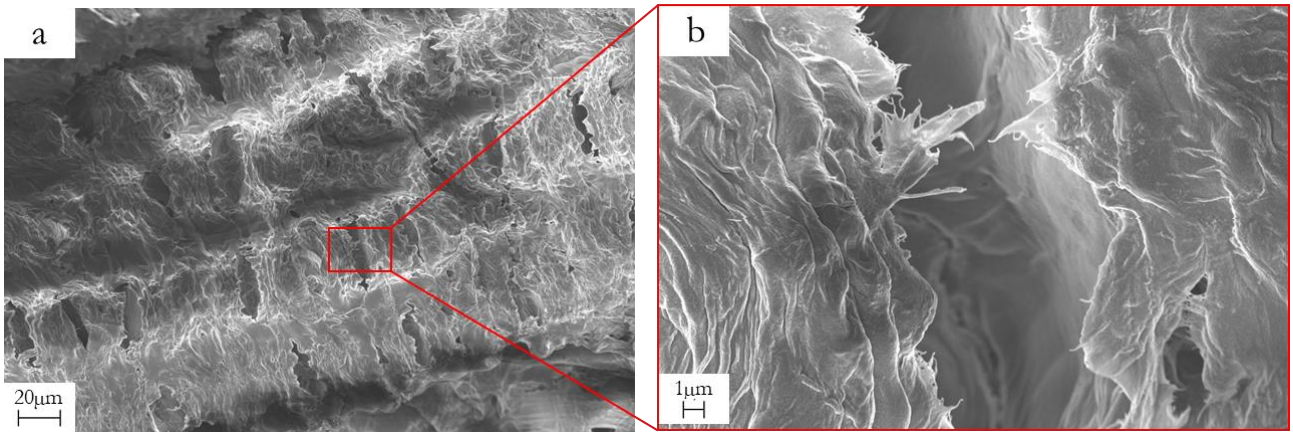

Figure 3-13 SEM micrographs of a) a portion of desilicated outer walls of rice husk with b) a magnification of the breaks between two edges of the outer rice husk walls.

Following Route 2, cellulose is obtained after bleaching the desilicated RH shown in Figure 3-13 in Figure 3-14 Route 2 cellulose is still composed of platelets and fibres, however there are some differences in morphology and dimensions: platelets (Figure 3-14a,b and c) appear wider with frayed edges like the outer shells leached shown in Figure 3-13 and holes over platelets have a different shape, not elongated as holes in Figure 3-14a(cellulose route1) but more circular. Fibres (Figure 3-14d, e and f), on the other hand, have a larger average diameter around 9.8±1.2 µm.

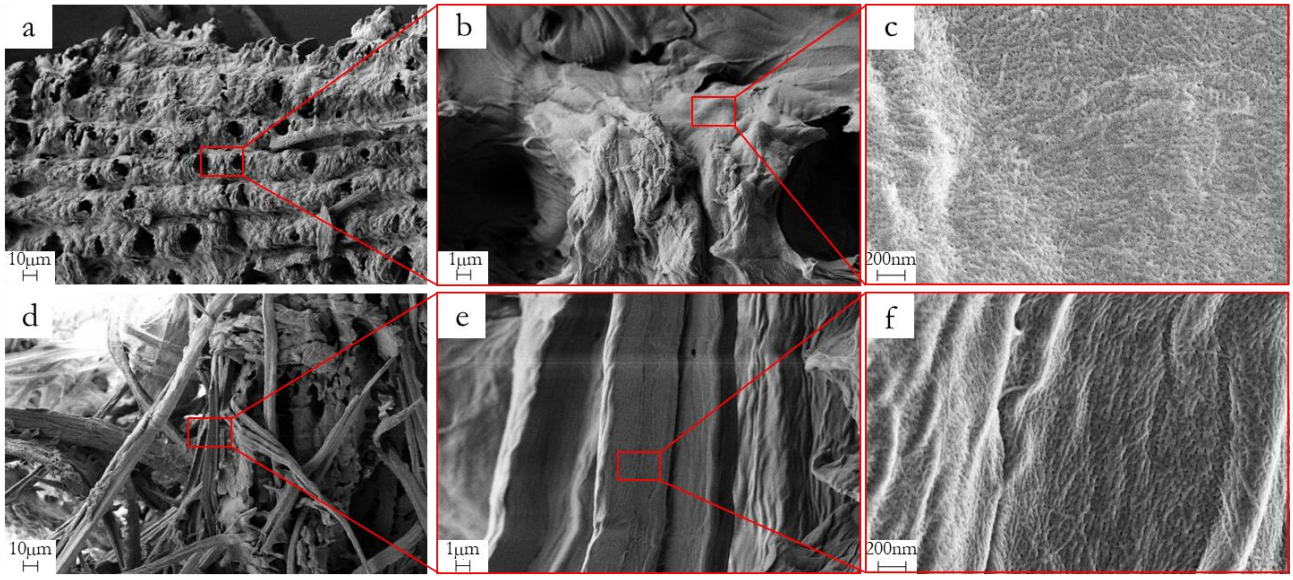

Figure 3-14 two sets of three subsequent magnification (a-b-c and d-e-f) of cellulose obtained from Route 2 SEM micrographies

In any case the surface of both platelets and fibres still appears porous and composed by fibrils o cellulose clusterized.

Cellulose Gel and CAs in Route 1

Cellulose purified from RH was dissolved at two different concentrations (i.e. 2%wt and 7%wt) in a mixture of NaOH, urea and water regardless of the synthetic route. After gelation, gelation and freeze drying occur, a solid cellulose aerogel is obtained, and its structure was investigated by scanning electron microscopy as well.

In Figure 3-15 we can observe the surface of a gel with cellulose concentration of 7% synthetized according to Route1 process. Its surface appears smooth at lower magnification (Figure 3-15a) but zooming progressively on it we can observe it is actually rough and made of many small nanometric parts that appear to be on a smooth surface below (Figure 3-15b and c).

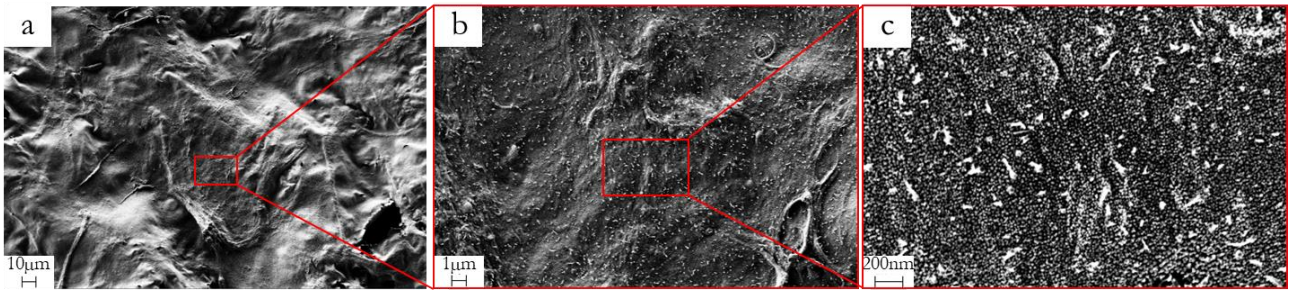

Figure 3-15 SEM micrographs of a cellulose gel at subsequent magnifications obtained by cellulose purified from Route 1

When this cellulose aerogel are carbonized, they produced a Carbon Aerogel that was called, according to Table 3-1 when the cellulose was at 2%wt and 1B when cellulose was at 7%wt concentration.

SEM micrographies representing both 1A and 1B are shown in Figure 3-16 and Figure 3-17 respectively. Overall, both samples at lower magnification (Figure 3-16a and Figure 3-17a) show a rather similar morphology, and the materials appear as interconnected networks of fibres and sheet-like structures of compacted structures of carbonized cellulose, hereinafter named respectively fibres and platelets. No significant differences in the relative distribution of these two microstructures can be noticed over the sample by mean of scanning electron microscopy.

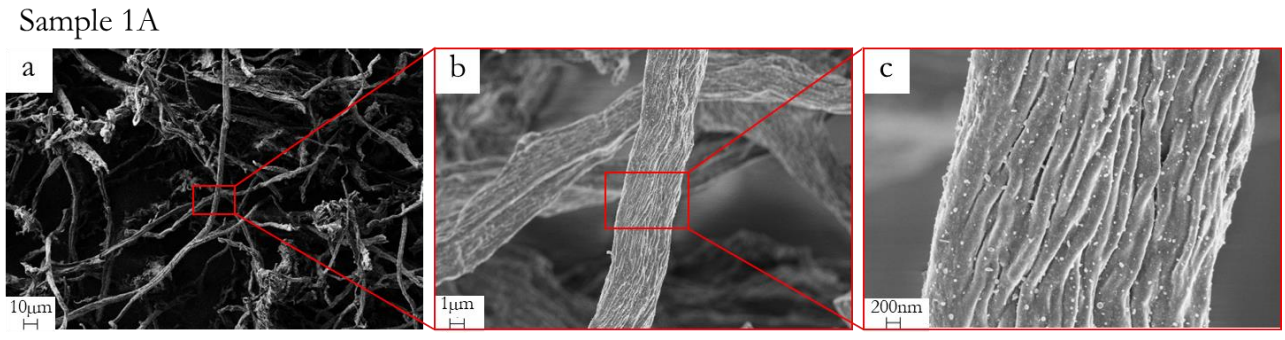

Figure 3-16 SEM micrographs of 1A Carbon aerogel at subsequent magnifications

Despite a comparable general morphology, at higher magnification (Figure 3-16b and c and Figure 3-17b and c) images show that the surface of both samples 1A and 1B (i.e. obtained following Route 1) looks rough, with clusters of carbon nanostructures and pores all over fibres and platelets, however sample 1B also looks more porous.

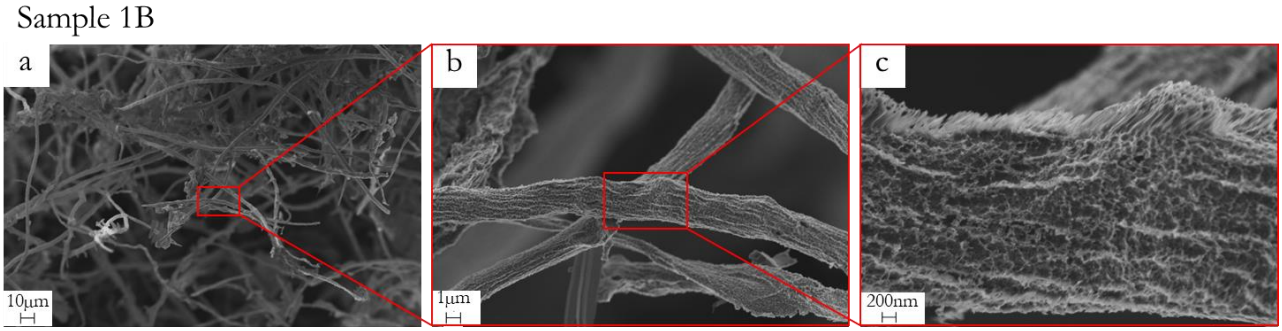

Figure 3-17 SEM micrographs of 1B Carbon aerogel at subsequent magnifications

Software ImageJ was used to perform a statistical analysis of the fibre dimensions in order to measure average diameter of CAs produced. At least two hundred fibres per sample have been observed and the average diameter of samples 1A and 1B were respectively 3.7±0.9µm and 3.3±1.1 µm.

Cellulose Gel and CAs in Route 2

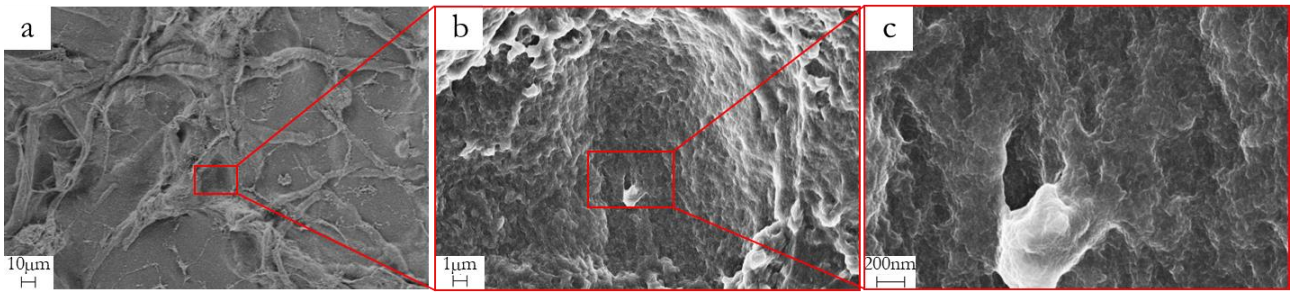

Figure 3-18 SEM micrographs of a cellulose gel at subsequent magnifications obtained by cellulose purified from Route 2

When Route 2 was followed, the gel surface at lower magnification (Figure 3-18a) appear smooth and similar to gel obtained from cellulose of Route 1, with fibres intertwined over and underneath a continuous cellulose matrix. Increasing magnification (Figure 3-18b and c), however, the surface appears rough but more homogeneous than Route 1 gel, where small particles were visible all over the coarse and irregular surface. Moreover, the roughness appears made of elements fused together with coalesced edges.

CAs pyrolized from cellulose from Route2, according to Table 3-1, were called 2A (at 2%wt cellulose) and 2B (at 7%wt of cellulose), and their micrographs are shown in Figure 3-19 and Figure 3-20. Following synthetic Route 2 at low magnification (Figure 3-19a and Figure 3-20a) it is still possible to observe in both CAs distributions of fibres and platelets. However, the surface appears much cleaner than samples 1A and 1B, with very few particles over the surface and smaller pores. When observed at higher magnification (Figure 3-19b and c and Figure 3-20b and c) samples 2B seems to be rougher than 2A, like 1B was compared to 1A, but in any case, the difference seems definitely

less remarkable than in the previous synthesis. Moreover, samples 2B doesn't show a similar porous nature of samples 1B at higher magnification and its roughness is mostly due to coarse surfaces.

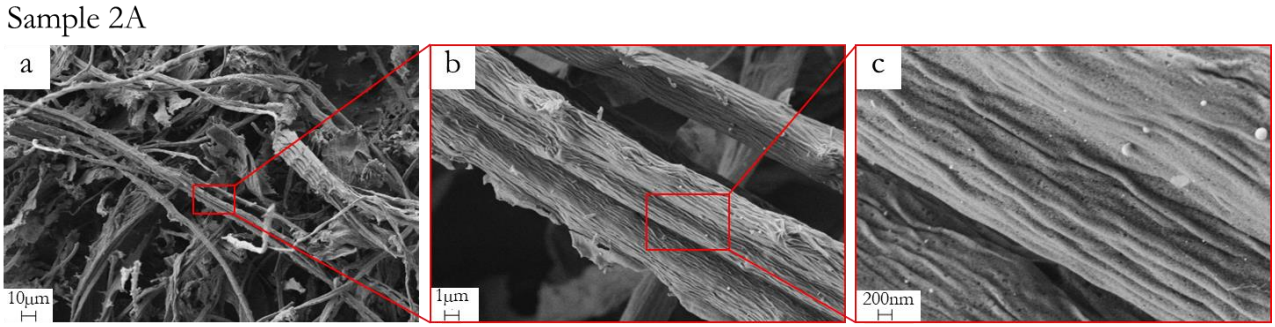

Figure 3-19 SEM micrographs of 2A Carbon aerogel at subsequent magnifications

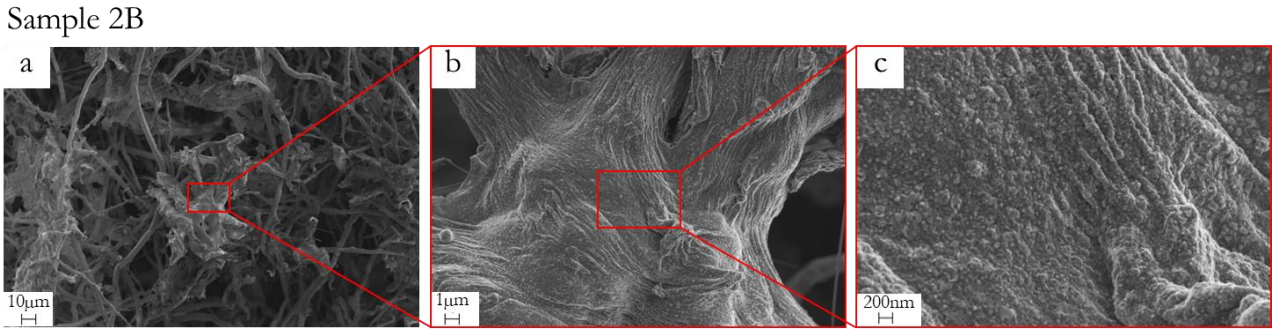

Figure 3-20 SEM micrographs of 2B Carbon aerogel at subsequent magnifications

ImageJ software was used to investigate average fibres diameter also with samples 2A and 2B and the values are respectively 4.0±1.2 µm and 3.7±0.8 µm.

At first glance it seems that there could be some effect of the synthetic route over the final values of diameters, with sample 1B offering the smallest average value and a tendency to decrease upon increasing the concentration of cellulose (i.e. from samples A to B) and to increase upon moving from Route 1 to Route 2. However, all measured diameters are in the range from 2 to 6 µm and standard deviations values are remarkable, therefore this parameter might not actually indicate meaningful differences in the samples.

Energy Dispersive X-Ray Spectroscopy

Energy Dispersive X-Ray Spectroscopy has been applied to investigate the evolution in the composition of samples after each step. Values are shown in Figure 3-21 and have been obtained after collecting at least three measurements each sample for at least two samples.

As it is shown, Rice Husk is rich in silicon, in particular in the outer shell, in the form of SiO_2. The average amount of silicon identified in our sample is in good agreement with literature knowledge over RH composition where usually silica has a concentration around 20%wt. The other component of carbon and oxygen represent the organic part of cellulose, hemicellulose and lignin.[170]

Following Route 1 in the first step, lignin is removed along with a portion of hemicellulose, therefore the silicon relative amount seems to increase- The removal occurs in the next step with sodium

hydroxide leaching, when only cellulose is left from the starting material. As expected, no silicon remains in the sample after this passage.

On the other hand, during Route 2 synthesis, the first passage is the removal of SiO_2, and as shown in Fig.4-26, it is totally effective. However, samples still contain a remarkable amount of hemicellulose and lignin. These components are removed in the subsequent step of bleaching and pure cellulose is obtained. Overall the two routes in parallel result in samples with comparable elemental composition in terms of C and O %wt.

During pyrolysis at high temperature in Ar atmosphere, volatile components are removed along with side reaction components that originate from cellulose gel degradation. The final material has a low oxygen content and a large amount of bonds, both single and double, between atoms of carbon. Sometimes a residual silicon percentage might be fund in samples and it can be ascribed to causal contaminations from quartz vessels in the tubular furnace. In any case, being extremely low (i.e. below 1%) and highly variable over the samples it is considered negligible.

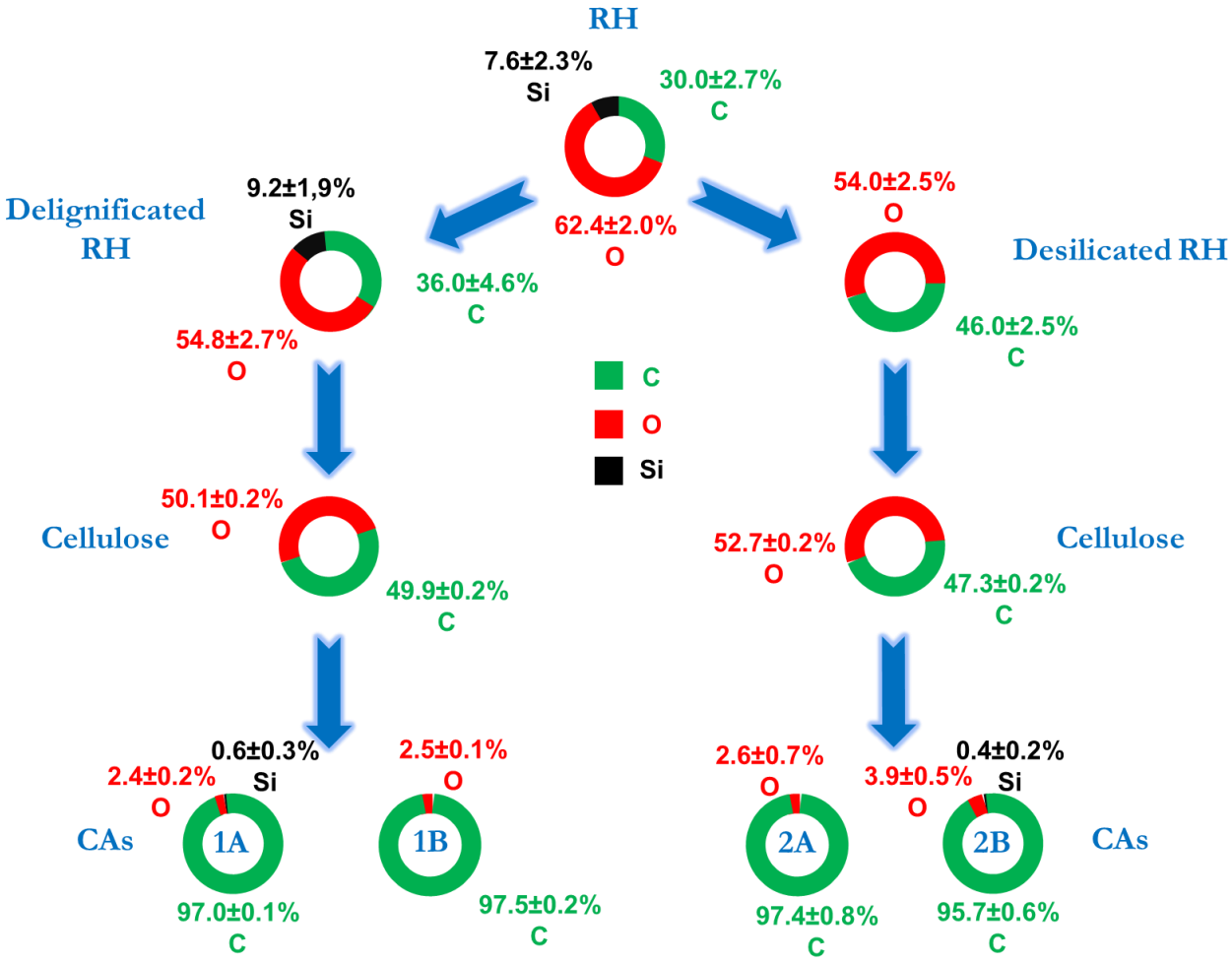

Figure 3-21 EDX atomic percentages of different samples from Rice husk to carbon dots

XRD

The structure of samples and their evolution through the synthetic process was investigated by means of XRD. Results for final materials and every single intermediate passage of synthesis are shown in Figure 3-22(black line). The diffractogram of the starting matrix of RH clearly shows the structure of cellulose I_β. This structure is typical of cellulose produced by vegetables and has a main peak around 22° that corresponds to plane with miller Indexes of (200). Other two peaks are shown around 16° for (110) and (1-10) reflection and a single weaker one can occur at 34° for (004) planes. Other components of Rh like hemicellulose, lignin and silica show no signal in XRD analysis, thus confirming their amorphous nature that makes them invisible for this technique. X ray investigation of cellulose lattice allows to calculate Cristallinity Index (CI), a parameter that indicates the crystalline quality of cellulose. There are many methods to calculate CI, in this study the following equation was used:

$$CI = \frac{(I_{200} - I_{am})}{I_{200}} \qquad \textit{(eq.1)}$$

I_{200} indicates the intensity of the main peak of cellulose, the peak with Miller indexes (200), while I_{am} is the minimum intensity between (110) and (200) peaks, used as accounts for the amorphous content in cellulose.[207]

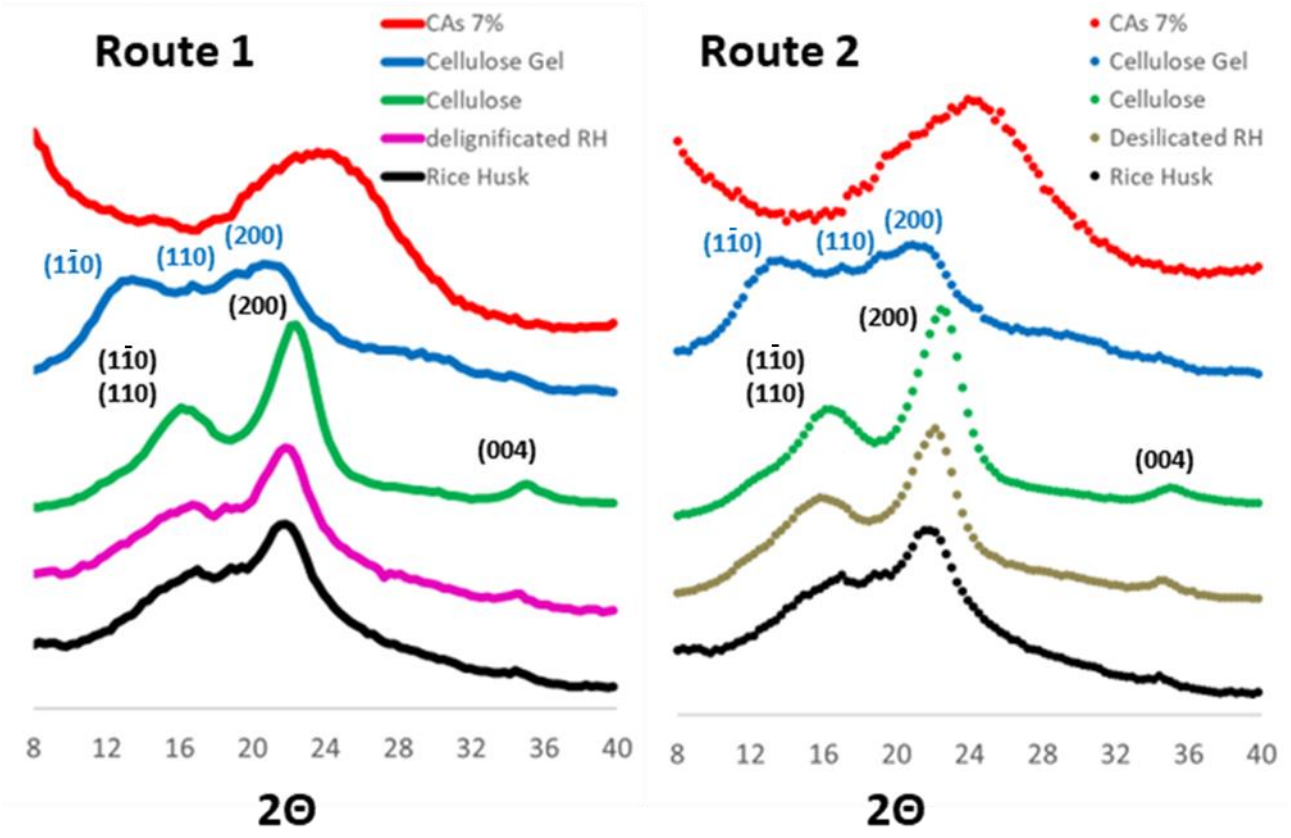

Figure 3-22 XRD Diffractograms of different samples from RH to CAs divided by synthetic strategy

CI was calculated for every step of synthesis involving cellulose and are shown in Table 3-3. Cristallinity index can't represent with accuracy the real crystallinity quality or actually give a real value of the percentage of crystallinity in cellulose framework, however it can still be used to observe the evolution of samples during the synthesis of CAs.
Since (200) peak in RH diffractogram has low intensity, CI appears small, around 27.1%, which is in good agreement with the high content of amorphous components that forms the matrix.
As Figure 3-22 XRD Diffractograms of different samples from RH to CAs divided by synthetic strategy shows, in both synthetic route in the first two step the cellulose framework is maintained as I_β with crystallinity that increases up to a CI of 52.2% for cellulose samples obtained in Route 1 and 53.2% for cellulose in Route 2. This raise is due to the removal of the amorphous component, once pure cellulose is obtained crystallinity increases. Since values of CI for cellulose are actually very similar, it can be concluded that there is no visible effect of the pretreatment chosen on the overall structural characteristics of cellulose samples.
Although it is known that sodium hydroxide induces mercerization, i.e. the irreversible crystalline transition of cellulose I_β to cellulose II via a reorganization of chains from a parallel configuration to an antiparallel structure, this transformation doesn't occur, probably because 1M concentration of NaOH is not enough to promote this process. Therefore, cellulose purified via this synthetic strategy maintain its original structure.

Sample	Crystallinity Index
Rice Husk	27.8%
Bleached RH	31.4%
Cellulose	52.2%
Cellulose Gel	15.5%
Desilicated RH	42.2%
Cellulose	53.2%
Cellulose Gel	10.3%

Table 3-3 crystalline indexes of samples calculated using eq.1

However, during gelification, when cellulose is treated with a much more concentrated solution of NaOH and urea, the crystalline domains are broken and the long-range order disappears. Sodium Hydroxide swells the fibres and urea brings them into solution, once the gel is formed fibres rearrange in different structure thus leading to a different crystalline structure. Cellulose I_β peaks

disappear and the new diffractograms of cellulose gel show a very broad shape that indicates low crystallinity content. Cellulose gel are rich in amorphous domain with a few crystalline domain that are arranged as cellulose II. This structure presents three peaks at 12°, 20° and 21.5° that are respectively assigned to (1-10), (110) and (200) planes. As the broad shape of diffractograms suggested the calculated value of crystallinity indexes for gels, show very low values.

Carbonization process destroys crystalline domains of cellulose and provokes a transformation of fibres structure into a graphitic domain. Peaks of cellulose II are no longer visible and in the examined range only a main broad peak of carbon can be observed. This broad peak contains the main graphitic peak of (002) plane and its broad shape with low intensity testifies the partial graphitic nature of the obtained CAs that can be defined as disordered graphite.

There is a slight difference in the 2Θ value in the position of the peak of Cas obtained with the two synthetic route. While Route 1 CAs are centred around 23.9°, i.e. a plane distance of 3.7Å, Route 2 Cas is centred at 24.5°, which in plane distance is 3.6 Å. Therefore, this slight difference suggests that the two synthetic routes induce a minor but clear difference in the final product structures.

Raman Spectroscopy

Since X ray diffraction over carbon aerogel samples has shown a disordered nature, in order to further investigate the fibrotic carbonaceous framework organization in the short range, Raman spectroscopy has been performed. The obtained spectra shown in Figure 3-23 Raman spectra of the four different CAs produced clearly show that these disordered components have graphitic nature.

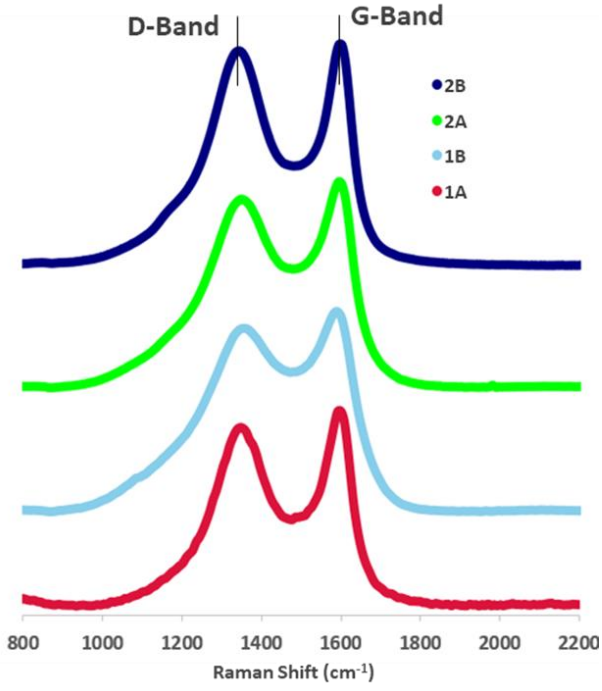

Figure 3-23 Raman spectra of the four different CAs produced

The two main peaks can be ascribed to graphite, where D-band represents the defects of the carbonaceous network while G-band is responsible of interlayer vibration phenomena of graphitic planes. The shape of the curve and the intensity of the two bands are actually similar for every

sample and the ratio between them the intensity of the two bands is typical of disordered graphitic compounds.

In fact, the I_D/I_G ratio values for the four samples are all quite similar as shown in Table 3-4. Samples at 7%wt concentrarion of cellulose in the gel have the same ratio around 0.91, while samples at lower concentration of cellulose offer higher variability with values o 0.89 for Route 1 and 0.87 for Route 2. Overall, these differences are in any case negligible since the materials have all the features of graphites with structural defects, which is in good agreement with those of Carbon aerogels obtained in literature form different sources.[208]

Sample	I_D/I_G
1A	0.89
1B	0.91
2A	0.97
2B	0.91

Table 3-4 I_D/I_G ratio of the four different CAs produced

X-ray Tomography

Since SEM analysis is limited to the external area of samples, in order to investigate the distribution over the three-dimensional framework of platelets and fibres, X-Ray Tomography was used to characterize bulk samples.

Carbon aerogels have been entirely scanned over the vertical and the horizontal direction in absorption mode as much as a portion of their core with more accurate phase contrast mode. Tomography is an interesting totally non-destructive technique already applied in the investigation of materials for electrodic materials that allows to study the core nature of a monolithic sample.[209]

By means of this analysis a cylindrical portion of the four different CAs was observed and reconstructed by elaborating slices of samples both in vertical direction, i.e. along Z axis from the bottom to the top of the samples, and in horizontal direction along Y or X axis (These are equivalent thanks to the cylindrical symmetry of samples).

The main parameters observed were length, width and distribution along different directions of the denser carbonaceous structures. Two different modalities of investigation were performed, namely absorption and phase contrast mode. In absorption mode a larger portion of samples was analysed with a lower resolution in order to observe a general distribution through the entire sample. On the other hand, in phase contrast mode a smaller cylindrical region of the inner core of CAs was investigated to study differences in the vertical and horizontal distribution of carbonaceous structures within the network of different samples.

Each images have a three-dimensional insert in the upper left part that indicates the position along the sample of the corresponding two-dimensional slice observed. The brighter areas in figures are portion with higher mass density when observed with X-Rays and therefore they were identified as the platelets formed by the fibres.

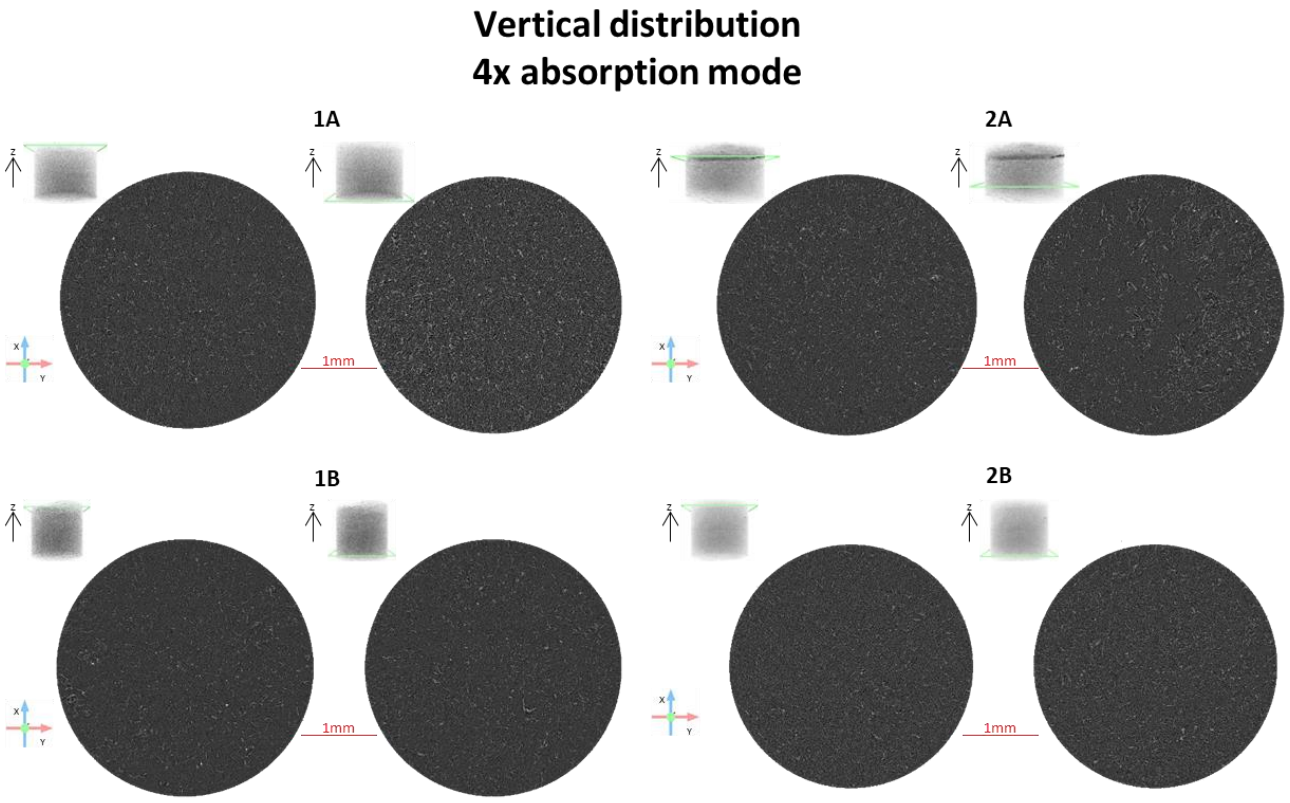

Figure 3-24Vertical distribution of Platelet in CAs investigated in absorption mode at two different heights for each CAs produced

The vertical distribution of the denser regions of samples was investigated in absorption mode and results can be seen in Figure 3-24. Samples 1A and 2A (i.e. obtained at 2% concentration of cellulose) show higher density of platelets in the bottom part. Comparing these two samples, platelets of 1A appear smaller than those in 2A and this difference seems particularly enhanced in the lower part. On the other hand, samples 1B and 2B that were obtained at 7% cellulose concentration show a more homogeneous distribution of platelets in the vertical direction. We can conclude that during carbonization of samples at higher concentration of cellulose, fibres tend to aggregate in the same way all over the samples. This experimental observation seems to be coherent with the parameters previously calculated of shrinkage and density of the samples, where CAs obtained at 2% concentration of cellulose showed the tendency to compact, thus offering higher shrinkage and density.

The phase contrast mode analysis in the inner region of CAs along the Z axis is shown in Figure 3-25. Now, observing a smaller portion the resolution is highly improved and the dimension of platelets can be measured. Samples obtained following Route 1 show a lower density of platelets compared to Route 2 samples and the length of fibres in Route 1 increases along with the cellulose

concentration. In samples 1A there are more bright areas, and they appear much shorter with average length of 59.8±4.9 µm whereas 1B has less platelets but consistently bigger with average measured length of 120.6±18.4 µm. On the contrary the width decreases with the increasing cellulose concentration. In sample 1B an average width of 5.7±0.6 µm is measured while sample 1A has 6.7±0.4 µm of average measured width. Therefore, we can conclude that following Route 1, concentrated samples have the tendency to form longer and thinner platelets, thus creating a network of elongated aggregates and fibrotic structures.

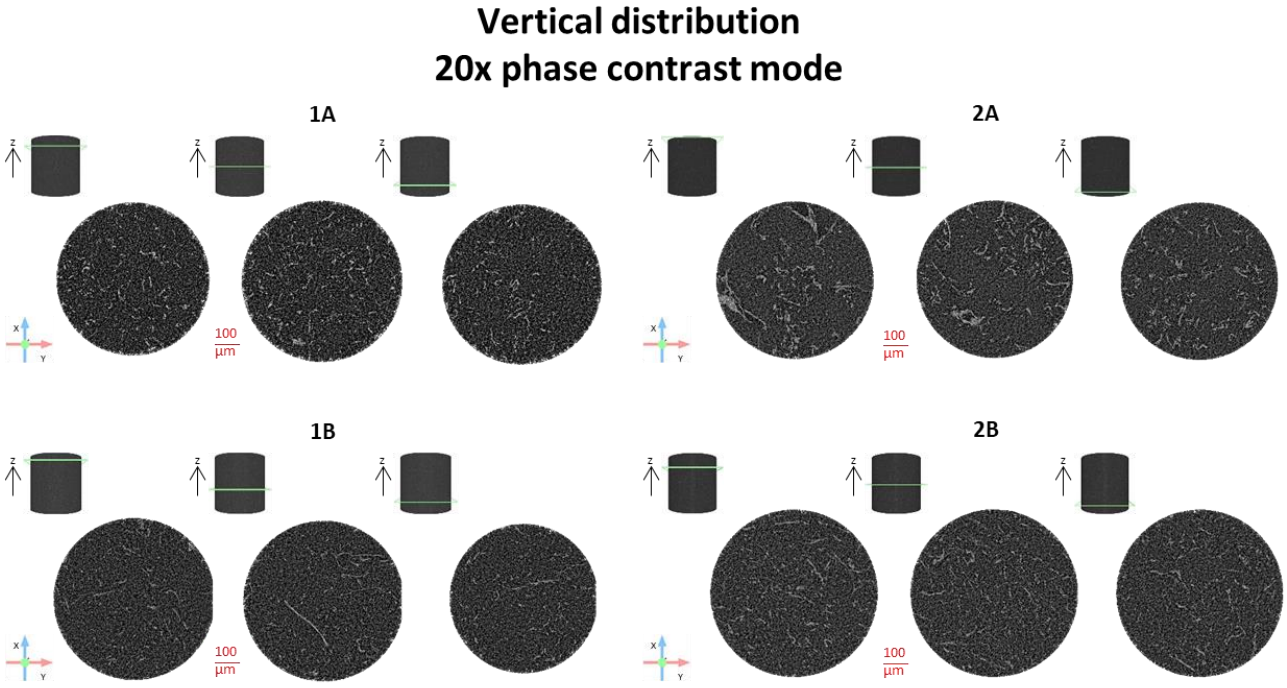

Figure 3-25 Vertical distribution of Platelet in CAs investigated in phase contrast mode at three different heights for each CAs produced

Moving to samples obtained following Route 2, we can see in both samples, i.e. at any cellulose concentration, a remarkably number of platelets, and they are characterized by higher average dimensions. However, while during Route 1 there seems to be no significant variations in terms of platelet distribution and shapes and overall the samples remained fibrotic even with visible differences in dimensions, samples obtained during Route 2 also change the nature of their platelets aggregates and even distribution. Sample 2A is characterized not just by elongated structures but also by cluster-like platelets and three-dimensional aggregates that seem more concentrated ion the upper region of the investigated area. Moreover, differently from Route 1, now both the average length and width of brighter areas is decreasing upon the increasing cellulose content, going from average measured length of 114.7±13.8 µm and 27.4±8.1 µm from sample 2A to 2B and average width goes from 92.3±8.7 µm in 2A to 6.8±0.3 µm in 2B.

X-ray Tomography analysis along Z-axis can actually be rather informative on the nature and homogeneity of carbonaceous network formed in CAs during pyrolysis, on the other hand the investigation of structure and distribution of platelets along the horizontal direction shows no significant changes. As it can be seen in Figure 3-26 along the direction radial to cellulose deposition

during the formation of gel there is no clear disposition or organization of the platelets structures generated in the synthesis.

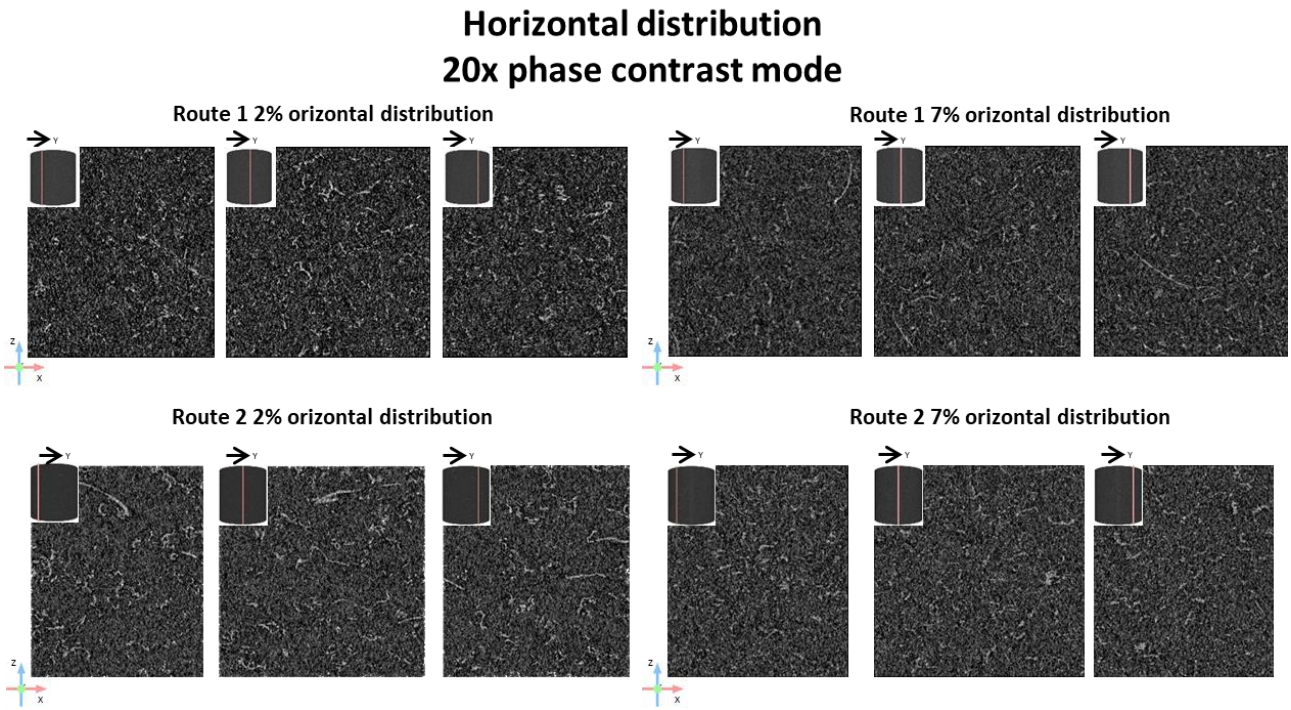

Figure 3-26 Horizontal distribution of Platelet in CAs investigated in phase contrast mode at three different sections for each CAs produced

BET

The electrochemical performances of carbonaceous materials are strongly dependant on the specific surface area and the pore distribution and dimension. Therefore, BET analysis was performed in order to achieve a deeper understanding over the surface nature and porosity of Carbon aerogels.

Sample	SSA [m^2g^{-1}]	Pore volume [cm^3g^{-1}]	Pore Width [nm]
1A	15.08	0.23	4.08
2A	728.30	3.21	1.14
1B	341.73	1.93	0.97
2B	22.79	0.24	3.68

Table 3-5 Specific surface area (SS), Pore volume and pore width of the four CAs produced calculated by BET analysis

Values of obtained specific surface area (SSA), total pore volume, pore size, and pore distribution of the as prepared CAs, are shown in Table 3-5. Samples 1A and 2B offer very small surface area with

a average pore width of respectively 4.08nm and 3.68 nm. As it is possible to observe in Figure 3-27 Distribution of the contribute of pores to the final specific surface area for every sample (black curves) and cumulative pore volume (red curves)both samples are rich in mesopores that hinder the formation of a wide surface area. Moreover, these pores have high variability showing a broad distribution of dimensions. In sample 1B a large SSA can be observed around 341.73 m^2g^{-1}, which may look considerably smaller than sample 2A with its 728.30 m^2g^{-1}, which is the highest value collected. However, sample 2A pore volume is totally ascribed to micropores and pores of width around 1.14nm seems to account for more than the 80% of the total pore volume. On the other hand, sample 1B despite a smaller SSA and average pore diameter shows a pore width distribution much richer in mesopores and a more developed hierarchical structure. This can actually represent an optimum compromise between surface area and pore distribution and can enhance the performance of CAs electrodes, offering both wide surface area for charge accumulation and reaction sites and larger pores as channels for ion diffusion.

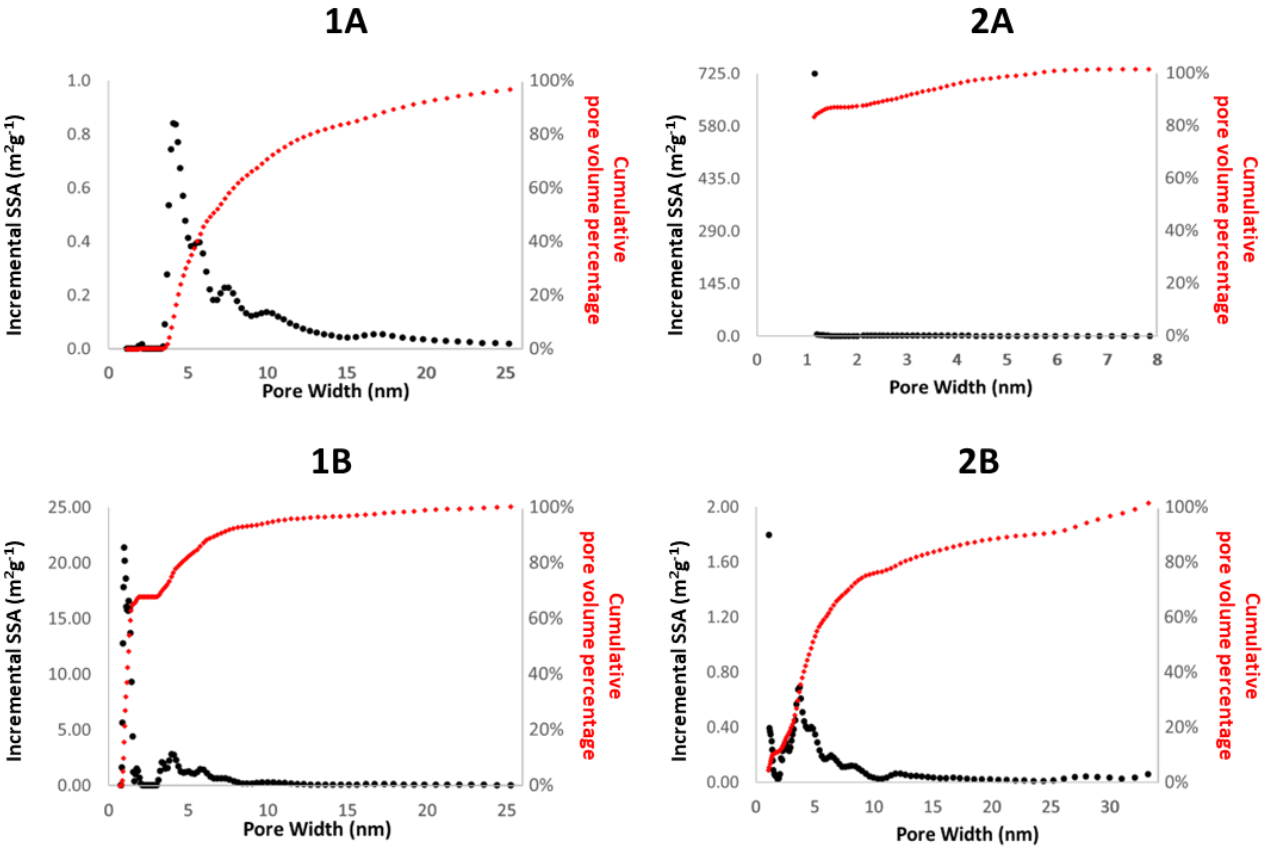

Figure 3-27 Distribution of the contribute of pores to the final specific surface area for every sample (black curves) and cumulative pore volume (red curves)

3.3.3 CAs Applications

Carbonaceous materials derived from cellulose purified from rice husk were tested in electrochemical applications. All different carbon aerogels proposed were tested as supercapacitors and the most promising sample was also tested with different electrolytes, in order to move to a

milder electrochemical solution that would allow preliminary studies on electrochemical AFM, and as anode for lithium-ion devices.

CAs Supercapacitors Electrochemical performance

Cyclic voltammetries have been collected for all CAs in scan rate range from 1 to 50 mVs^{-1} and voltammograms for all sample at 5mVs-1 are shown in Figure 3-28. All curves show a quasi-rectangular shape, however cyclovoltammograms of samples obtained in Route 1 clearly show a larger area than those samples synthesized with Route 2. Within the same synthetic procedure, the area is larger for sample 1B, i.e. higher concentration of cellulose during gelification. And as shown in Table 3-6, in terms of capacitance Route 1 offers more than three times the value offered by samples 2A and 2B.

Cyclic voltammetries allow to calculate specific capacitance using the formula:

$$C = \frac{\int idV}{\varepsilon m V} \qquad (eq.2)$$

where C is the specific capacitance, I is the current, V is the potential window, m is the mass of the active material in the electrode and ε is the scan rate used in the experiment.

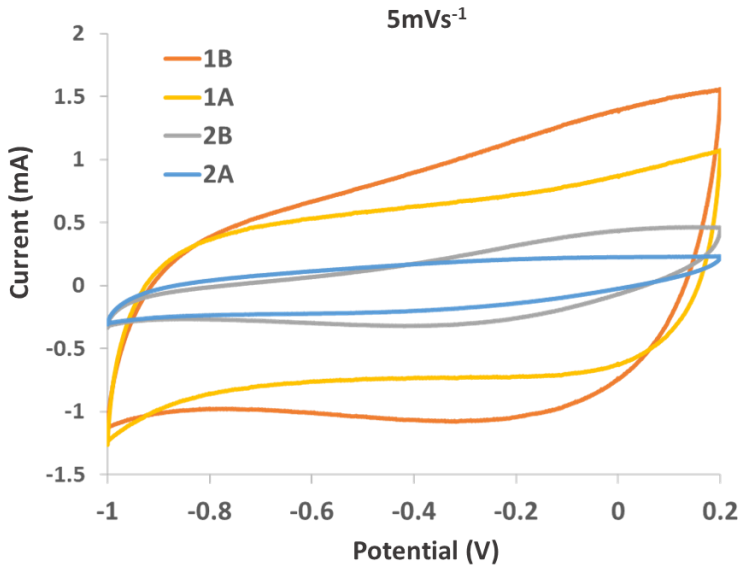

Figure 3-28 cyclovoltammetries of the proposed CAs electrodes, 1B (orange line), 1A (yellow line), 2B (grey line), 2A (blue line)

Sample	Capacitance Fg^{-1}	Sample	Capacitance Fg^{-1}
1A	42.5	**2A**	12.6
1B	52.7	**2B**	13.7

Table 3-6 capacitance values for different CAs calculated by CV according to Eq. 2 at $5mVs^{-1}$

The sample with the better performances in terms of capacitance is sample 1B, which has, among all samples studied, an intermediate valuer of surface area (341.73 m^2g^{-1}). Samples 1A and 2B have lower capacitance value and show very low surface area, but surprisingly the lowest capacitance is offered by CAs 2A which has the largest surface area and highest total pore volume among all samples (see Table 3-5). This apparently counterintuitive results can be explained by considering how the apparently beneficial large surface area of sample 2A is actually due to an abundance of micropores with a really narrow distribution with average diameter around 1.14nm. This means the totality of the surface area is ascribed to micropores with almost total absence of mesopores, and this results in a surface actually available to the electrolyte consistently lower than the surface measured by means of BET due to diffusional limits. Sample 2A could be unable to provide enough space for ions to diffuse into carbon aerogel framework, and since the interphase between aerogel and the solution is connected to the charge accumulation, this limits the performance of 2A as electrode. On the other hand, the intermediate value of sample 1B that has a large portion of micropores but also a more hybrid composition and is rich in mesopores around 5nm, creates a hierarchical structure that mitigates diffusional limits. Therefore, thanks to its ion-accessible surface, this sample can actually offer a more efficient charge storage and offer the best electrochemical results. These experimental evidence and the role of the pore distribution in the electrodic performances of carbon electrodes have already been shown in literature, e.g. from Zu et al.[210] and Kim et al.[211].

As shown for sample 2B in Figure 3-29 the quasi-rectangular shape of cyclic voltamograms is lost upon increasing the scan rate and current grows at higher potential. Capacitance tends to decrease likewise, moving from 70.3 Fg^{-1} at 1 mVs-1 to 20.3 Fg^{-1} at 50 mVs^{-1}. Compared to literature values, such as nanocellulose CAs obtained by Zu et al.[210], the values of capacitance obtained in this study might appear consistently lower. However, this is reasonable considering that our process brings to the formation of microdimensional fibrils of cellulose, while the authors were using pure nanocrystalline cellulose, which implies larger surface areas and well-developed porous structures with more accessible surfaces.

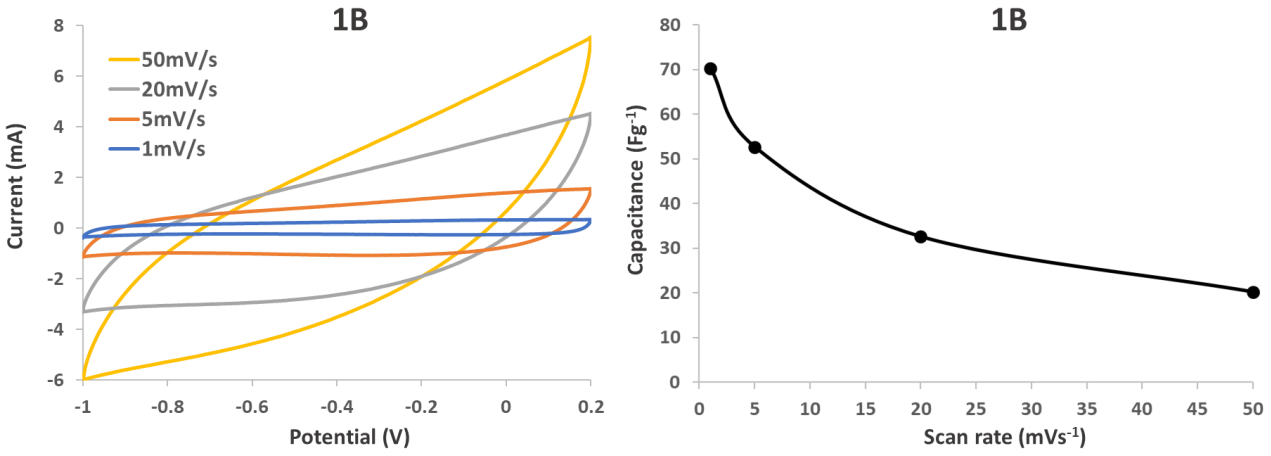

Figure 3-29 Cyclovoltammgrams collected at different scan rates for sample 1B and capacitance as a function of the scan rate (black dots and line) calculated according to eq.Z

In order to evaluate CAs performance as capacitors, galvanostatic cyclations have been studied too. Capacitance has been calculated by the following equation:

$$C = \frac{i\Delta t}{mV} \qquad (eq.3)$$

where C is the specific capacitance, I is the constant discharging current density, Δt is the discharging time, m is the mass of active material in the electrode and ΔV is the potential window in the galvanostatic discharge

Plots of potential as a function of time during a cycle of discharge and charge in galvanostatic cyclation are shown in Figure 3-30 for every CAs sample at the same current density of 0.1Ag^{-1}. All materials exhibit a quasi-triangular shape with the same trend shown by cyclic voltammetries, i.e. no sign of any faradic reaction occurring and higher specific capacitance for sample 1B. In fact, the samples lasting for longer times and thus offering higher capacitance, as shown in Table 3-7, are in order 1B, 1A, 2B and 2A.

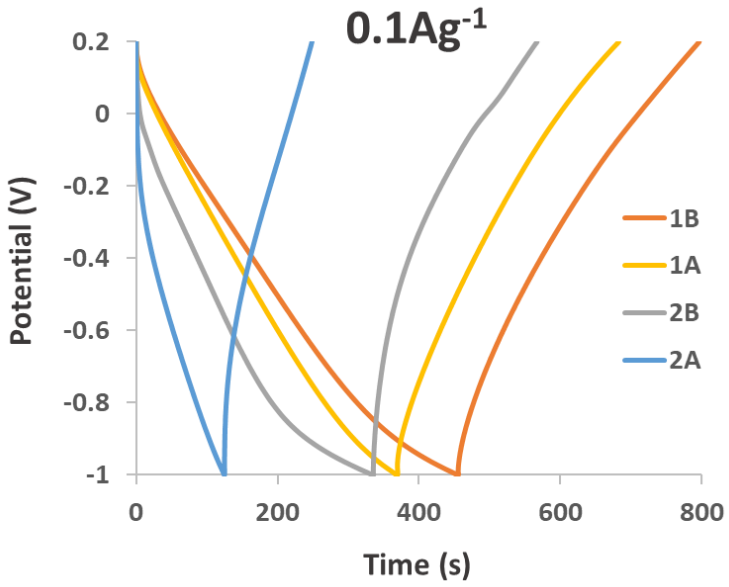

Figure 3-30 evolution of potential during a single cycle of discharge and charge for all proposed CAs samples: 1B (orange line), 1A (yellow line), 2B (grey line), 2A (blue line)

Sample	Capacitance Fg^{-1}	Sample	Capacitance Fg^{-1}
1A	30.6	**2A**	10.4
1B	58.0	**2B**	27.9

Table 3-7 Capacitance calculated according to equation 3 by galvanostatic cyclations data obtained at 0.1 Ag^{-1}.

CAs 1B electrochemical behaviour, being the most promising among our materials, has been further investigated. In Figure 3-31 a galvanostatic cycle in discharge and charge is shown for this sample at

each current density considered, and in every condition the proposed material always offer good charge accumulation capability with the triangular shape maintained.

The capacitance decreases, as expected, with the increase of currents, going from 58.0 Fg^{-1} at 0.1 Ag^{-1} to 21.3 Fg^{-1} at 1 Ag^{-1}. The range of values appears to be in good agreement with the range of those obtained by CV.

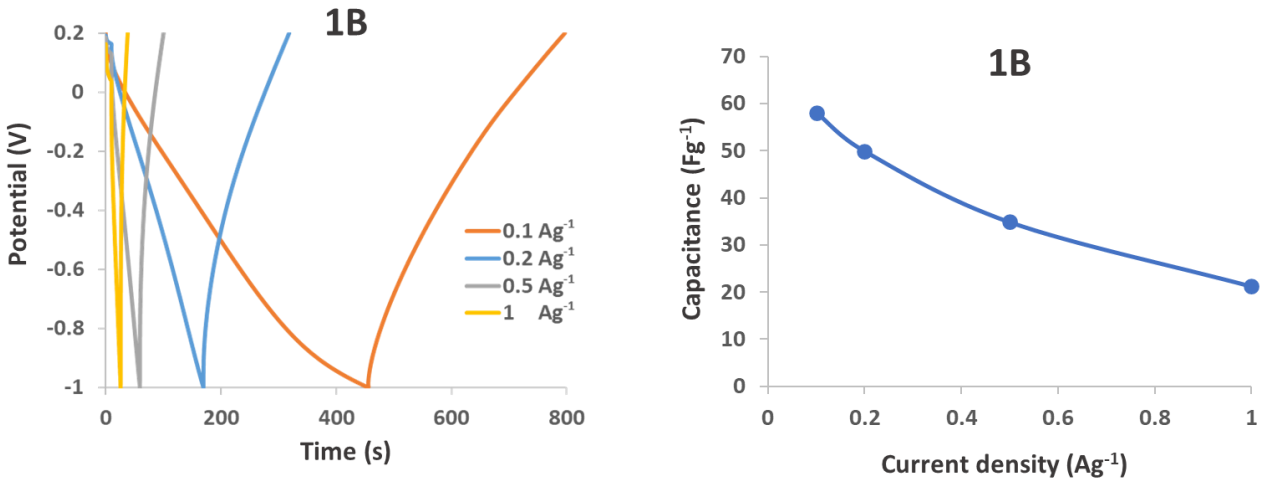

Figure 3-31 Evolution of potential during a single cycle of discharge and charge at different current density for a 1B CAs electrodes and capacitance calculated according to Eq Z as a function of the current.

However gravimetric capacitance value obtained by CV or galvanostatic cyclations are still low compared to values obtained in literature. Nonetheless the proposed material is still promising and appealing, not only for its virtuous nature, but also for its property of stress resistance and capacitance retention.

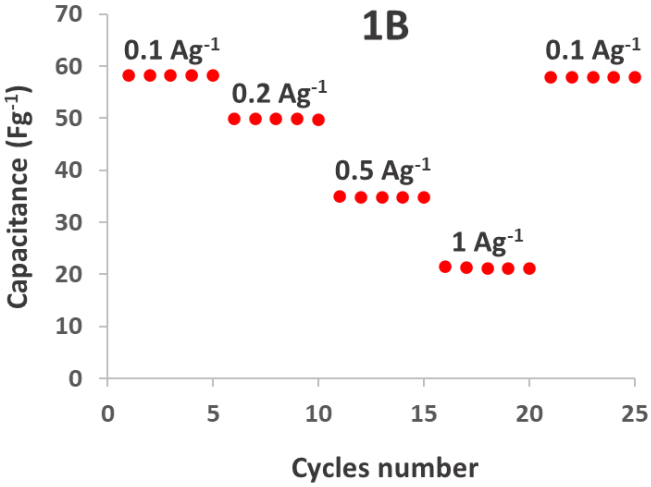

Figure 3-32 Capacitance retention of a 1B CAs electrode under stress condition

In fact, 1B material offers excellent rate capability, i.e. the ability of returning to the original capacitance obtained at lower current density even after undergoing the stress of increasing the current at higher values. As shown in Figure 3-32 a CAs was tested at current up to 10 times the first value and when it was still able to offer the same initial capacitance, thus indicating high stability of the electrode under stressful conditions.

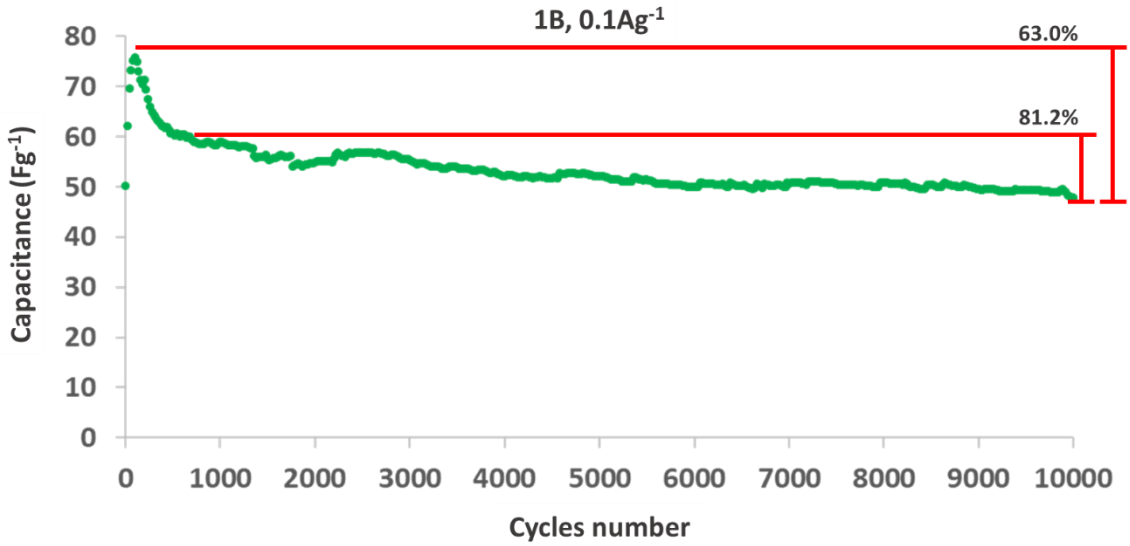

Figure 3-33 life of a 1B CAs electrode for prolonged work

Furthermore, Sample 1B has an extraordinary long-life cycle. As shown in Figure 3-33, the proposed material actually undergoes an initial increase of capacitance in the first 200 cycles, which is a behaviour typical of all the samples presented in this study, reaching around 75 Fg^{-1}. Subsequently there is a significant loss of capacitance till around 500 cycles, when the sample stabilizes and experience a stable trend. The electrode keeps working after 10'000 cycles, thus confirming robustness and long life. Comparing capacitance values along the experiment it can be seen that after 500 cycles, when the trend is stabilized, electrode 1B has a capacitance around 61.0 Fg^{-1}, and after 10'000 cycles capacitance has decreased to 47.8 Fg^{-1}. This means that material 1B offers a capacitance retention of 63.0% compared to the maximum value and 81.2% compared to the value at 500 cycles.

Supercapacitors Performances with different electrochemical solutions

Since CAs 1B was identified as the best performing material among all those considered in this study, it was chosen for every following performance test and hereinafter all electrochemical characterization showed in chapter 3 will refer to a 1B Carbon aerogel electrode.

The application of different electrolytes as electrochemical solution was investigated. The research for a new electrolyte can expand the potential application of the proposed CAs and allows to test the robustness of the material and the perspective of adapting the systems for in operando studies, like electrochemical AFM, where the instrument requires milder operating conditions.

Both a change in the base and the concentration has been investigated and electrochemical solutions used are shown in Table 3-8.

For each electrochemical solution, both Cyclic voltammetries and galvanostatic cyclations have been performed. Voltammograms at 5mVs^{-1} for every solution are shown in Figure 3-34 and in none of the samples there is evidence of faradic reactions occurring. This result was expected since there is no difference in the electrochemical behaviour of the involved chemical species, but only a difference in the dimension of the cation Na^+. The device working with KOH 6M shows a higher capacitance than other samples and there is a clear effect on the concentration of the electrolyte

on the charge accumulation over the surface. The concentration affects both the capacitive behaviour of the material and the ion transport in solution, leading to a lower gradient of concentration close to the surface and a weaker migration in the bulk of the solution.

		Electrolyte	
		KOH	**NaOH**
Concentration	**6M**	KOH 6M	NaOH 6M
	1M	KOH 1M	NaOH 1M

Table 3-8 brief resume of electrochemical solution applied for supercapacitors

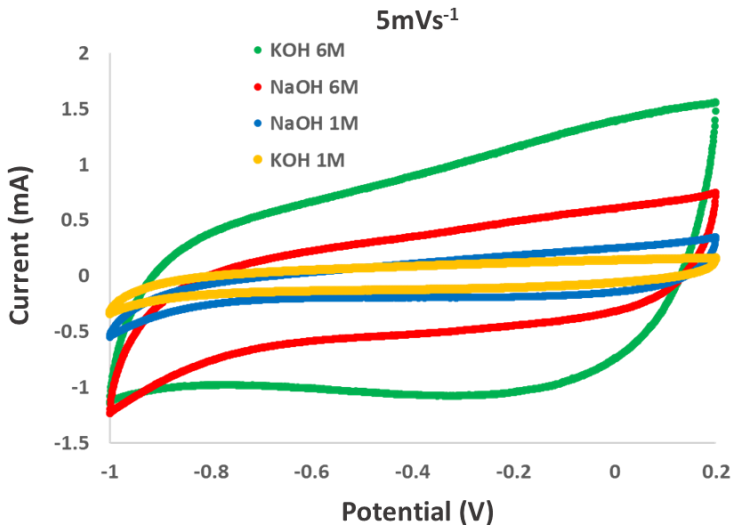

Figure 3-34 cyclovoltammetries of 1B CAs electrodes using as electrochemical solution: KOH 6M (green dots and line), NaOH 6M (red dots and line), NaOH 1M (blue dots and line) and KOH 1M (yellow dots and line)

This effect is amplified at higher scan rate, when the process gets faster, and ions have less time to diffuse and migrate over the surface, therefore capacitance is expected to fade. In fact, as it can be seen in Figure 3-35 where values calculated by CV according to eq.2 are showed as a function of the scan rate in a range from 1 to 50 mVs^{-1}, all electrolytes present similar behaviour.

However, two main characteristics can be noticed, KOH 6M device still offers capacitance values between 25 and 70 Fg^{-1} in the investigated scan rate range, while NaOH 6M not only offers smaller capacitance (from below 10 to 52 Fg^{-1}) but also has a much more consistent capacitance loss moving from 1mVs^{-1} scan rate to 5mVs^{-1}, thus showing a less robust behaviour.

Meanwhile, at lower concentration capacitance are way more similar in values (from around 2 to 22 Fg^{-1}) and in trend for both NaOH and KOH, indicating that the detrimental effect of a lower molarity is much more intense than the effect of the different dimensions of the cation.

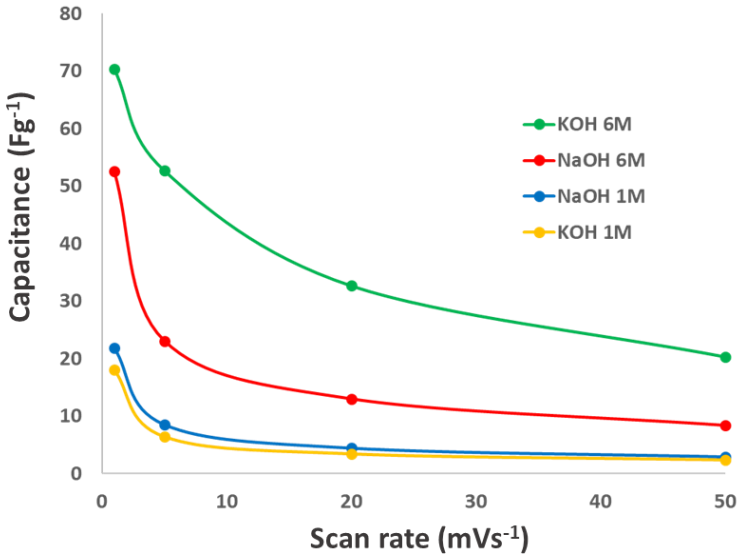

Figure 3-35 Capacitance as a function of scan rate for 1B CAs electrodes using as electrochemical solution: KOH 6M (green dots and line), NaOH 6M (red dots and line), NaOH 1M (blue dots and line) and KOH 1M (yellow dots and line)

In fact, the diffusion and migration limits imposed by a lower concentration hinder the capacitance more than the different nature of the electrolyte and CAs electrodes show similar values and trends at 1M. This suggests that there is no actual difference for the two electrolytes used at low molarity. On the other hand, increasing the concentration and mitigating any diffusive and migrative limit, the different chemical nature of the cation starts to play a role in the electrode performance and a consistent difference between samples at 6M concentration of electrochemical solutions appears. CAs samples working with KOH 6M decreases with a slower trend compared to NaOH 6M, and the difference can only be attributed to the accumulation of different ions over the carbon aerogels surface and the transport inside the pores of the solvated cations.

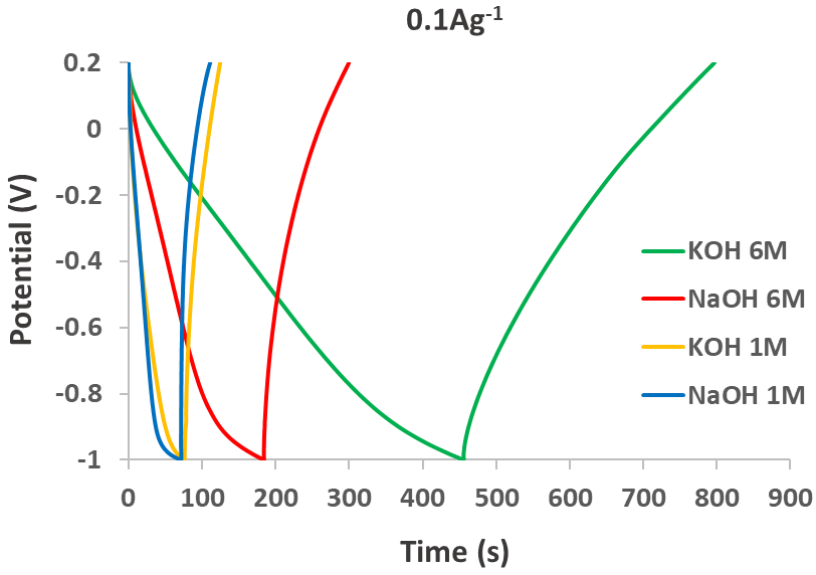

Figure 3-36 trends of capacitance as a function of time for 1B CAs electrodes using as electrochemical solution: KOH 6M (green line), NaOH 6M (red line), NaOH 1M (blue line) and KOH 1M (yellow line)

Galvanostatic cyclations have also been used in order to further investigate the robustness of the materials and to confirm the trends obtained by means of cyclic voltammetry.
A single cycle of discharge and charge for each electrochemical solution used is showed in Figure 3-36. All curves are collected at a current density of 0.1 Ag-1 and all of them shows the quasi-triangular shape typical of capacitive behaviour, already shown in previous experiments. It is confirmed that samples working with a less concentrated solution have a similar behaviour and that at higher concentration, KOH allows to reach longer cycles compared to NaOH.
Galvanostatic cyclations were also used to study the life of devices using different electrochemical solutions, and the capacitance trend in prolonged use. Results are showed in Figure 3-37.

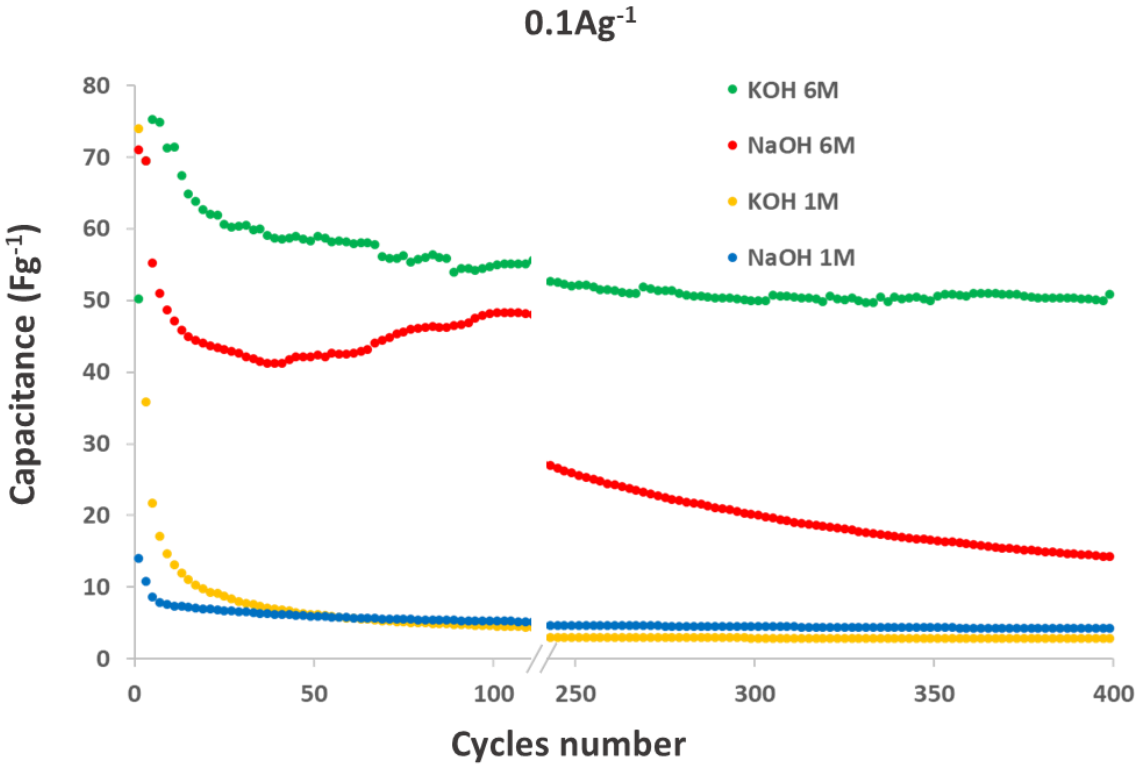

Figure 3-37 Capacitance as a function of cycles number for 1B CAs electrodes using as electrochemical solution: KOH 6M (green dots), NaOH 6M (red dots), NaOH 1M (blue dots) and KOH 1M (yellow dots)

The capacitance obtained by samples at 1M concentration is confirmed to be extremely low and it soon fades stabilizing below 10 Fg^{-1} even after just 50 cycles. Both 1M samples show a decreasing trend different from the curve showed by other samples in Figure 3-37 and here for concentrated electrochemical solution, where there is an initial increase in capacitance. It is confirmed that these 1M samples seem to have a very similar behaviour that seems unaffected by the nature of the electrolyte.
The sample at 6M NaOH, on the other hand, starts at lower capacitance but after 100 cycles it actually seem to reach similar values than the sample using KOH. However, this effect soon expires when looking above 250 cycles it is clear that capacitance is fading much faster than KOH 6M.

Whereas KOH 6M has a retention (compared to the value at 100 cycle) after 400 cycles of 92.2%, NaOH only has a retention of 29.4%.
Therefore, samples using electrochemical solutions of NaOH at high concentration initially works with lower but still comparable performance than KOH, but they don't manage to maintain this performance over a few hundred cycles, whereas our electrodes working with 6M KOH have demonstrated they can work up to 10'000 cycles (see Figure 3-33).
Capacitance for samples operating with the proposed electrochemical solutions was also studied at different current densities in a range from 0.1 to 1 Ag^{-1}. Results are shown in Figure 3-38 and they confirm again the trends and behaviours shown by previous experiments.

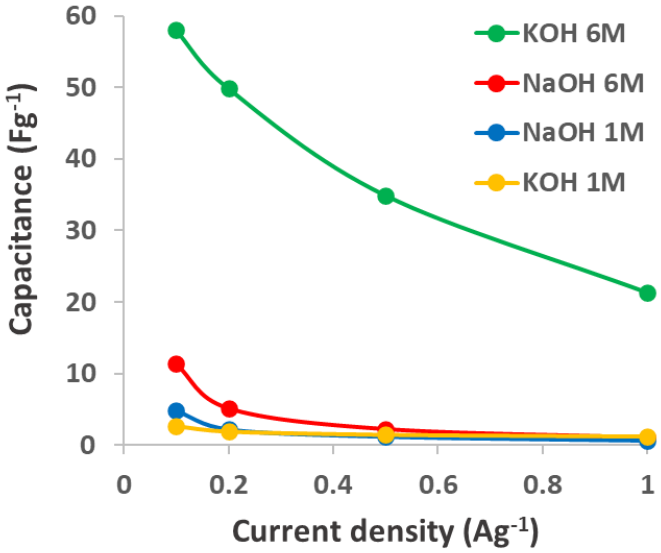

Figure 3-38 Capacitance as a function of current density for 1B CAs electrodes using as electrochemical solution: KOH 6M (green dots and line), NaOH 6M (red dots and line), NaOH 1M (blue dots and line) and KOH 1M (yellow dots and line)

CAs Electrochemical performance in Lithium-Ion Batteries

Sample 1B was also investigated as anode in lithium-ion devices. The disordered graphitic nature of CAs should allow the intercalation of lithium ions in the carbon framework and thanks to the different nature of this sample, where the amount of active material is clearly defined as the 80% of the mass of the entire electrode (being electrodes made of 80:10:10 composition of CAs, acetylene black and PVDF) it is possible to clearly determine the gravimetric capacitance.
The curves of potential are shown in Figure 3-39 for the first, the second, the fifth and tenth cycles at a current of C/10. During the first cycle, that lasts way longer than the others, the formation of the solid electrolyte interphase occurs. The discharge part of the curve is way longer than the charge because of the irreversible transformation of the surface, which is actually a beneficial phenomenon. A slow formation of a stable SEI in fact prevents the further degradation of the active materials. Moreover, where around and below 1.45V the first cycle begins a slower decrease, in following cycles, the potential actually has a quick fall below 1V. Around 1.4V is, in fact, the potential where the decomposition of the electrolyte ($LiPF_6$) begins on the surface of the electrodes, and it

indicates the SEI is forming. The evolution of the solid electrolyte interphase goes on during the rest of the discharge curve in particular around 0.6V.
Under 1V however, both when these reactions are modifying the surface and after the SEI formation is concluded, the reversible insertion of lithium ions into the graphite layers also occurs. And in fact, as it can be seen from the following cycles, there is a quick fall blow 1V, when the curves starts a slower but steady decrease.

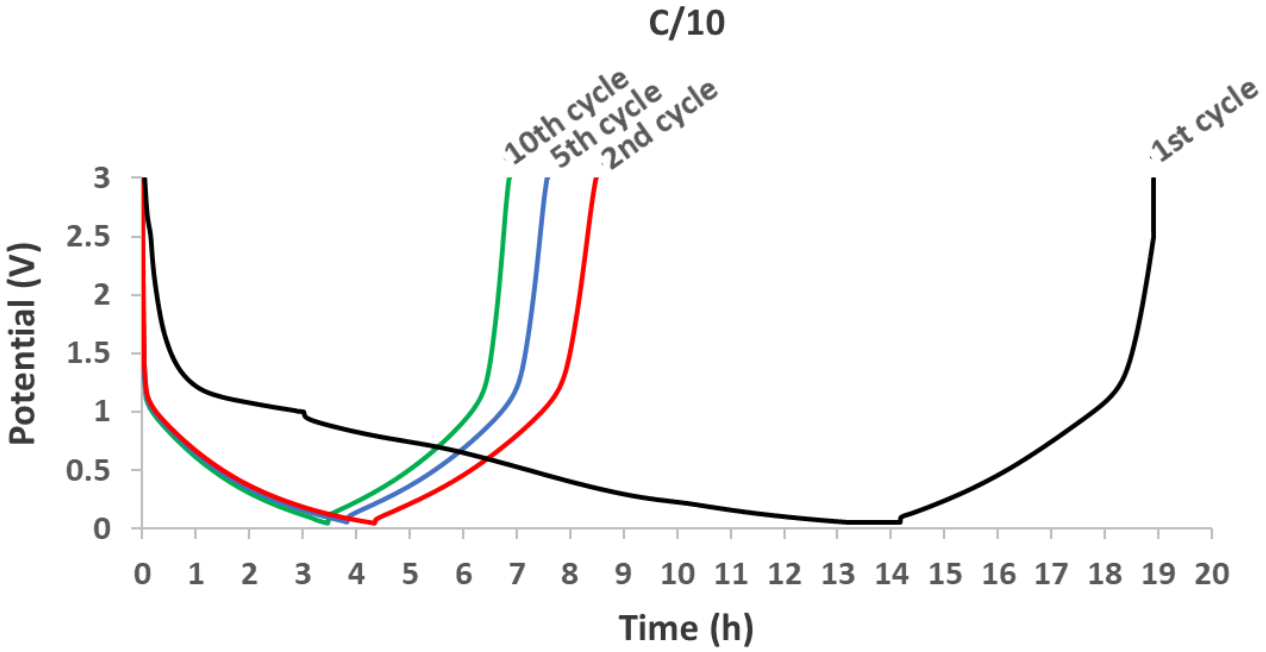

Figure 3-39 evolution of potential during a single cycle of discharge and charge of anodes for cycle 1 (black line). 2 (red line), 5 (blue line), and 10 (green line)

After this decrease below 1V the following charge cycle is pretty similar in length compared to discharge, indicating a good reversibility of the process, but it starts with a increasing irreversible gap with potential that, as soon as the charge begins, has a small but consistent step at higher potential values. Moreover, cycles are quickly decreasing their overall length.
Life and coulombic efficiency (i.e. ratio between capacitance in discharge and in charge) of 1B CAs as anode in Lithium-ion devices are shown in Figure 3-40 starting from the second cycle. The first cycle of SEI formation offered a capacitance of 460.55 $mAhg^{-1}$. After a quick loss of capacitance up to the 10^{th} cycle, from the 161.5 $mAhg^{-1}$ of the second cycle to 128.6 $mAhg^{-1}$ at the 10^{th}, the material starts showing a slower decrease, however, after the 30^{th} cycle this decrease fastens and the capacitance value quickly reaches 43.9 $mAhg^{-1}$, i.e. a retention of 27.2% of the second cycle.
Despite showing, even as anode in lithium-ion devices, low capacitance values and offering a small retention, our samples could still offer an outstanding coulombic efficiency that soon goes up to 100% after just three cycles, indicating that there is a perfect reversibility of the charge process. This result is still promising and indicates that if the electrode could improve its resistance to cyclations and stress occurring during lithium insertion, then the CAs could still be a promising candidate for low-cost carbonaceous anodes, despite its low capacitance.

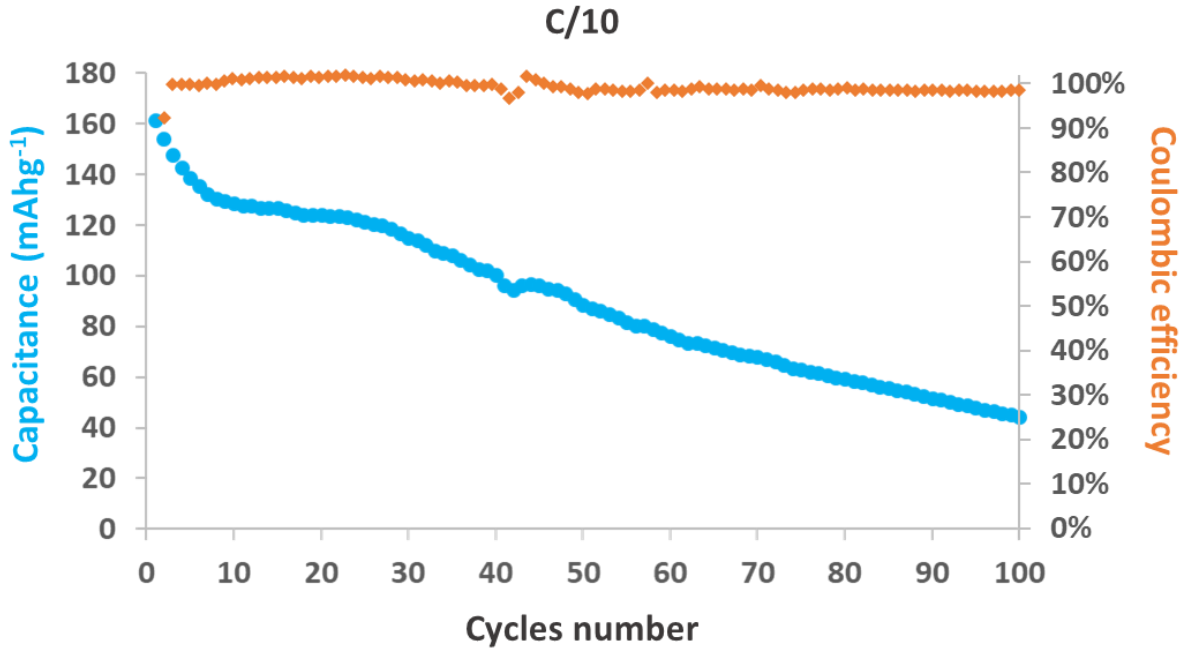

Figure 3-40 capacitance (light blue dot) and coulombic efficiency (orange diamond) of a 1B CAs electrode as a function of cycles number

In fact, since the SEI Formation seems stable and there is a good coulombic efficiency, the loss in capacitance could be due to a loss of contact between components of the electrode. The CAs fibres get inevitably damaged by the process of electrode fabrication during grinding and this probably leads to the loss of contact between carbon structure.

3.4 Conclusions

A facile synthetic process was developed to obtain carbon aerogels starting from rice husk. Some of the experimental conditions that mostly affect the properties of the aerogels were pointed out, and the whole process was optimized in terms of purity and yield.

After the physico-chemical characterization, the obtained aerogels were used to prepare electrodes for supercapacitors. Despite not showing good performances in terms of absolute values, 1B electrodes proved to be characterized by long life, robustness and electrochemical stability, with a capacitance retention up to 81.2% from cycle 500 to cycle 10000. Supercapacitors were also studied by changing electrochemical solution and moving to different solutes and concentration and the crucial role of molarity was pointed out as well as the role of the cation at higher concentration.

Moreover, the preliminary test of the 1B CAs as anode in lithium-ion batteries has demonstrated the capability of intercalating lithium ions despite a low retention of capacitance.

4 Carbon dots: exploring potentialities of 0D materials

In this chapters an immediate top-down passage to obtain carbon dots (CD) from 1B CAs, observed in the section 3 of this work, is proposed. The so obtained carbonaceous 0D material has been characterized to assure the obtainment of the correct morphology and nanostructure and tested both in symmetric supercapacitors and in lithium-ion devices.

4.1 Introduction: 0D materials and carbon dots

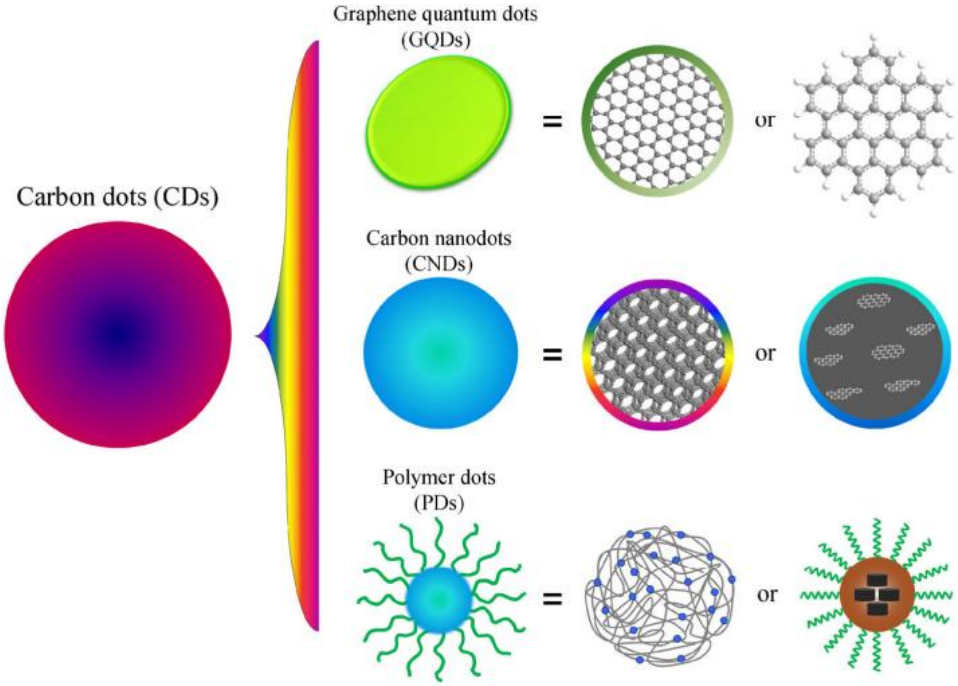

Figure 4-1 Three types of CD: graphene quantum dots, carbon nanodots, and polymer dots, taken from figure 1 from Zhu et al.[212]

Carbon dots (CD) are nano dimensional carbon 0D particle, that have attracted a lot of attention from research ever since 2006. [213] In fact, as the Nobel prize assignation in 2023 to Moungi G. Bawendi, Louis E. Brus, Aleksey Yekimov, "for the discovery and synthesis of quantum dots", demonstrated, 0D particles are actually considered a huge novel and advance of the research in the last decades. [214]

Carbon dots is indeed a comprehensive term for a range of nanosized carbon material, since. In a broad sense, all 0D structures that are composed mainly of carbon can be called CD. [212] This class (as shown in Figure 4-1 taken from Zhu et al.[212]) includes graphene quantum dots (GQDs), carbon nanodots (CNDs), and polymer dots (PDs).[215] In detail, this carbon nanostructured are made of a unique structure made of a core composed by a mixture of both sp^2 and sp^3 conjugated C atoms with abundant functional groups such as carboxyl, hydroxyl, and aldehyde in the outer amorphous surface. They possess ultra-small size, uniform dispersion, adjustable surface states, good dispersion in solvents, excellent electron transfer/reservoir properties and low cost for production.[52,215,216]

CD preparation methods generally fall into two categories of synthetic approach: top-down or bottom-up techniques. [52] Top-down techniques use higher dimensional (micro-sized or even macro-

dimensional) carbon structures, like carbon fibres, graphite, graphene, and graphene oxide, as starting resources to achieve a nanomaterial through a chemical or physical method like laser ablation, chemical oxidation, chemical exfoliation, arc-discharge, ball milling or ultrasonication. [217,218]

Conversely, a bottom-up technique uses smaller carbon precursors, like organic monomers, polymers or molecules to produce CD via different methods or reaction, i.e. hydrothermal, microwave or pyrolysis methods. [219,220] A schematic representation taken from Shaker et al.[221] is showed in Figure 4-2 that illustrates briefly the two approaches in fabricating a particular type of CD: carbon quantum dots and their application in supercapacitors.

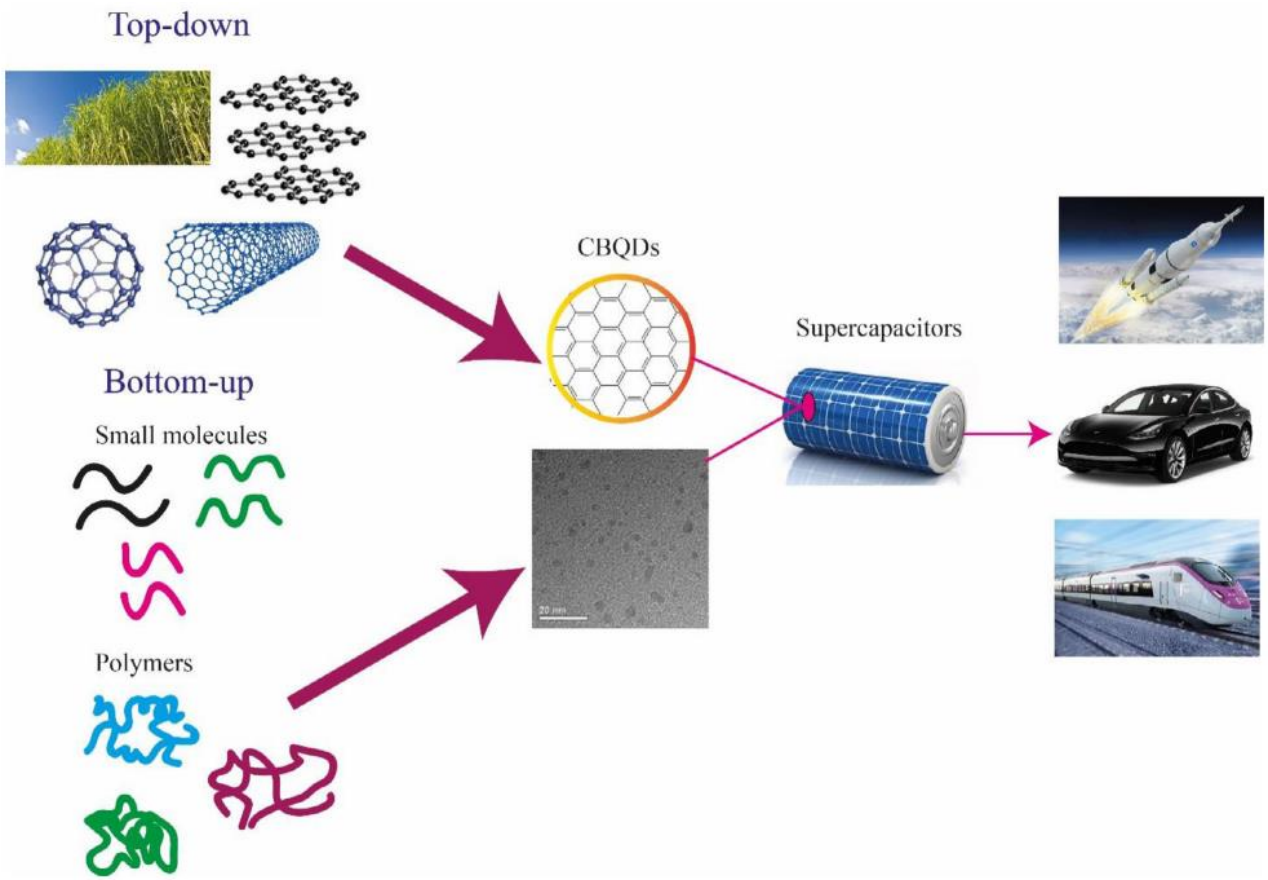

Figure 4-2 A schematic representation of bottom-up and top-down approaches for making carbon-based QDs and their applications in supercapacitors 2 from Shaker et al.[221]

In fact, Nowadays, despite having a huge range of possible application, CDs also have become a focus in electrochemical research.[56,222–226] It is efficiently demonstrated and recognized that CD could represent a great potential for a broad range of practical applications like bio-imaging, bio-sensing, photocatalysis, solar cells and LEDs. In this study we will focus on the energy storage materials and the promising role of CD in this sector. [224,226,227]

Recently for example, in fact CD-based electrodes and composites have well performed in Zn-air, aqueous and lithium or sodium ions batteries.[228–230] According to studies CD are able to provide

excellent interactions at the interphases with electrolytes and facilitate the charge transfer on the surface of electrodes, improving capacitance and kinetics.[231]
The state of the art and the observation of research groups through the world indicate a promising future of CD in electrochemistry, and in many other fields, certainly worth of further exploration and applications also in electrochemical energy storage.[232]

4.2 Materials and methods

4.2.1 CD Preparation

CAs were powdered in a ball milling grinder with agate spheres at 500rpm for 1h and the process was repeated for 5 times. The fine powder was collected with a spoon and both the jar and agate balls were rinsed with water in order to gather the pulverized CD. The solvent was removed by freeze drying to avoid sintering at high temperature.

4.2.2 characterization

Field emission scanning electron microscopy (FESEM) and energy dispersive X-ray Spectroscopy (EDX) were performed using a Zeiss Auriga electron microscope. Meanwhile XRD for cellulose based materials was performed using a Philips PW1830 APD3520 diffractometer using Cu-Kα radiation (λ 1.54 Å) in 2θ range 8-40°, with 40 kV voltage and 30 mA current.
Raman spectroscopy was performed with a Renishaw inVia Raman confocal Microscope using a green lamp (532.1 nm, output power 50 mW) and 100x lens, in the Raman Shift range between 800 and 2200 cm^{-1}.
Atomic force microscopy (AFM) analysis of carbon dots was performed with a BRUKER Dimension Icon in air by drying a diluted suspension of samples in water. Measurements were performed in tapping mode using RTESP-300 BRUKER tips (300kHz frequency, 40 N/m spring costant and nominal radius of 8nm). All images were postprocessed form background removal and levelling using software Gwyddion version 2.62.
Electrochemical performances were evaluated using a multichannel VMP potentiostat by Perkin Elmer Instruments and all samples have been studied in two-electrodes T-cells. Similarly to CAs, CD based electrodes were tested using the same relative quantities of components (i.e. 80:10:10 of CD, binder and adjuvant), however the electrodic powder was suspended in a slurry of N-Methyl-2-pyrrolidone (NMP) and drop casted over platinum (for supercapacitor) and copper (for Li-ion batteries) current collectors. As for CAs in supercapacitor application, an aqueous solution of KOH 6M was used as electrolyte. Galvanostatic cyclations and cyclic voltammetry tests were performed in -1.0 – 0.2V potential window respectively at different currents (0.1 – 1.0 $A \cdot g^{-1}$) and potential scan rates (1-50 $mV \cdot s^{-1}$). In batteries test galvanostatic cyclations in the range 0.04 – 3 V have been observed.

4.3 Results and discussion

4.3.1 Synthetic procedure

Figure 4-3 shows that after ball milling the carbon dots collected appear as a black fine powder with consistent volume loss compared to CAs material. The CD mass seems to increase around 15% of the original mass, which might be due to interaction of samples with air. In fact, ball milling is performed in air and the presence of oxygen along with the high energy induced by impacts and the breaks of C-C bonds occurring during collisions and the generation of new surfaces, could lead to surface reactions and the formation of superficial groups.

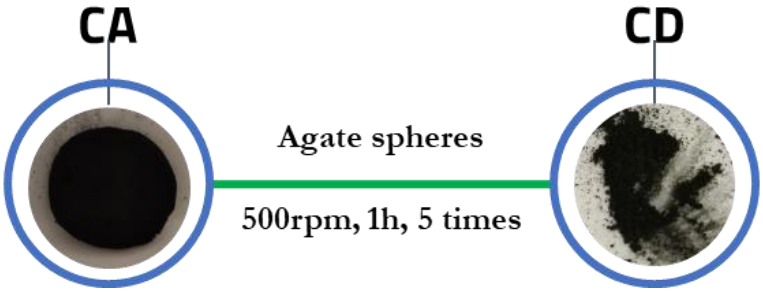

Figure 4-3 Schematic representation of CD preparation

4.3.2 COD Characterization

Scanning electron microscopy has been used to evaluate shape and dimension of Carbon dots obtained by ball milling of CAs. Samples have been investigated both in bulk, as an aggregate powder, to collect EDX spectra and information over the composition of samples, and as a diluted suspension over silicon wafer.

SEM micrographics of diluted suspension are shown in Figure 4-4, where CD are well separated and distributed all over the silicon surface. The average diameter has been measured by means of ImageJ software and the average carbon dots measure 27±9 nm.

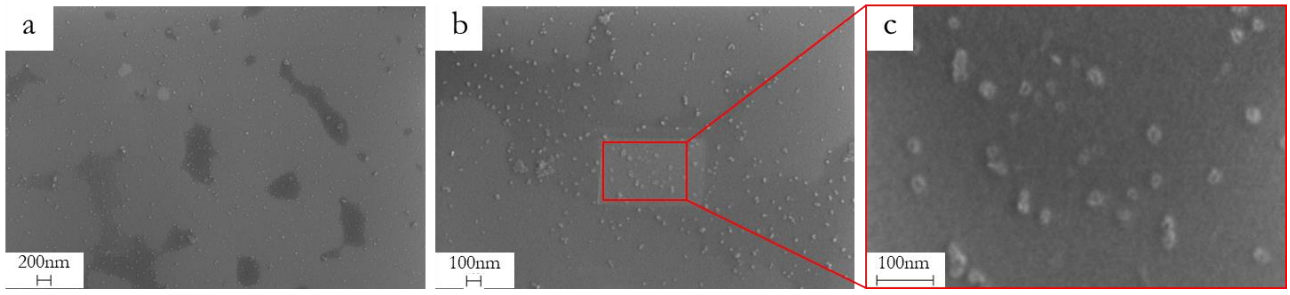

Figure 4-4 SEM micrographs of Carbon dots at subsequent magnifications

1B CAs was used as a precursor for the synthesis of Carbon dot and the EDX analysis over the bulk material (Figure 4-5) shows a composition of carbon with higher content of oxygen compared to the starting CAs. This might be due to a functionalisation of the surface that occur during high energy shocks and the disruption of bonds between carbon atom that arise during ball milling. The new

surface generated in the process undergoes different reactions and since ball milling occur in air, oxygen can functionalise the carbon dot generated.

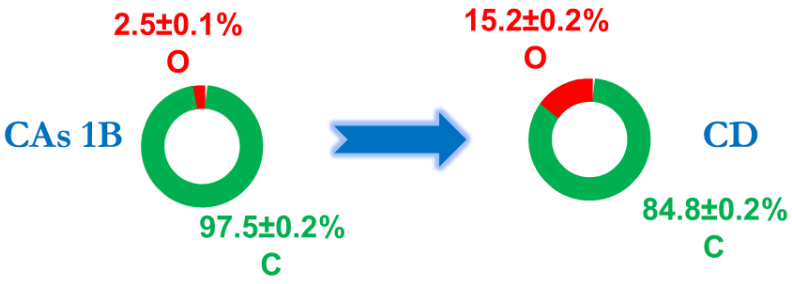

Figure 4-5EDX elemental analysis of a 1B Carbon aerogel sample and CD.

Carbon dots dimension and shape were also investigated by means of atomic force microscopy. Since the investigation of a bulk sample would have offered no useful information regarding this sample, CD had to be separated into smaller clusters or even single elements. To obtain such a sample, the CD powder was suspended in water and diluted until very high dilutions were achieved and a single drop of suspension was then casted over a silicon wafer support and left drying.
Images have been collected in tapping mode in a region of 1x1 µm.
Results of the investigation can be seen in Figure 4-6, where topography and phase maps are shown. Using ImageJ software an average diameter of 29.7±6.1 nm has been calculated, a value in good agreement with the diameter measured by means of SEM analysis. In fact, according to the t test performed on the two sets of data collected by measuring diameters of Carbon dots by means of SEM and AFM, the two values show no significant statistical difference (t_0 calculated was equal to-0.988 with a critical two tailed t of 2.035).

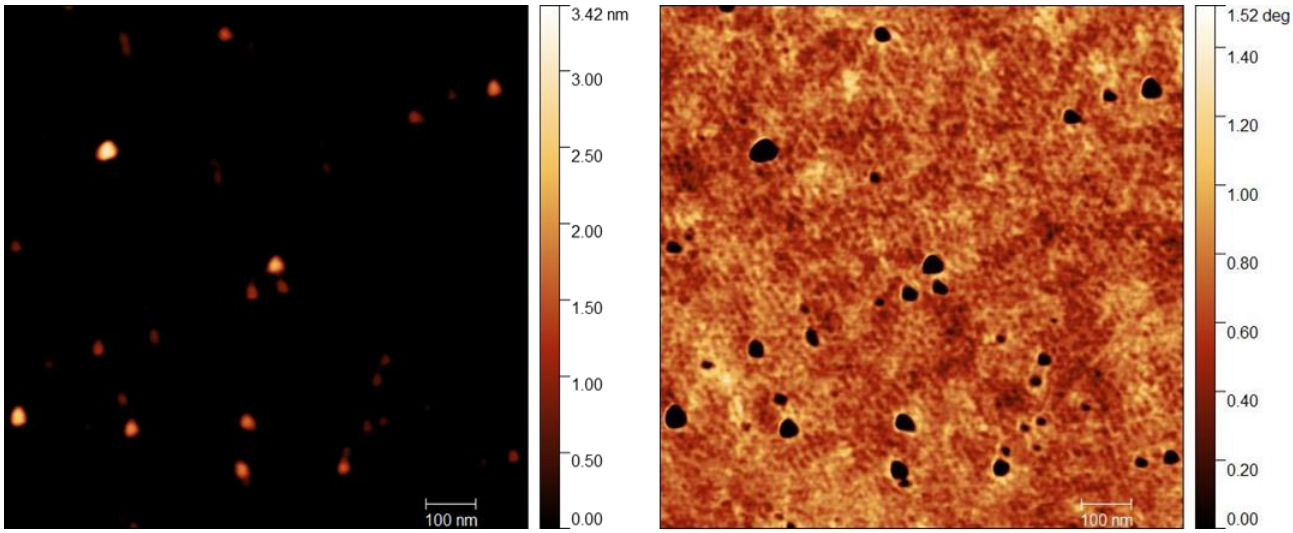

Figure 4-6 AFM topography and phase mapping of Carbon Dots casted over Si wafer

Diffractograms of carbon dot obtained by ball milling of 1B CAs samples has also been collected. In the same angular range, we can observe in Figure 4-7 that a sharp peak appears after ball milling. This signal at 26.6° (i.e. 3.3 Å) is the (002) signal of a more ordinated graphitic structure, which indicates that during ball milling, although there is the disruption of bonds between carbon atoms,

the energy of the impact between samples and agate spheres is enough to promote the crystallization of the resulting carbon dots. This final material in conclusion has a consistently higher crystalline nature compared to all the CAs obtained.

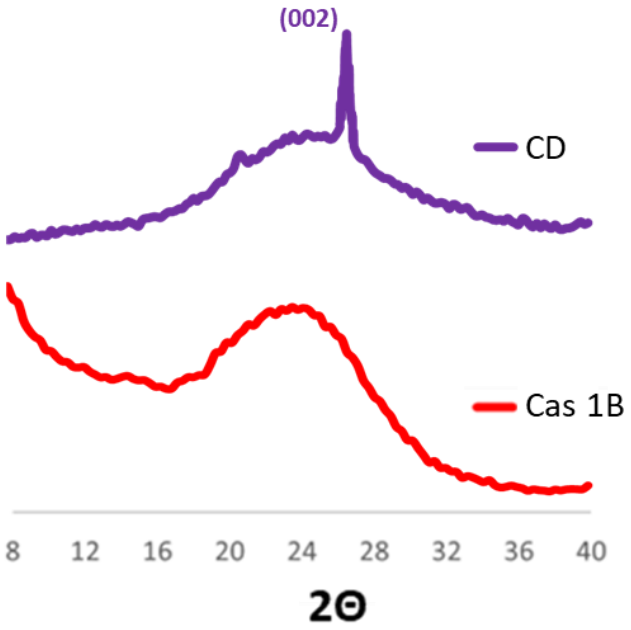

Figure 4-7 XRD Diffractograms of CAs from Route 1 (red line) and carbon dot (purple line) with Miller indexes

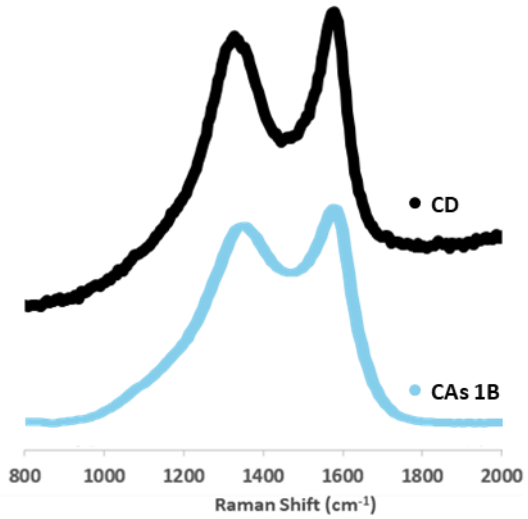

Figure 4-8 Raman spectra of 1B CAs (light blue) and Carbon dots (black)

Raman spectroscopy has also been applied to study the structure of carbon dots and to observe if structural changes occur during ball milling process. Raman spectrum of carbon dots is shown in Figure 4-8 and a very similar shape can be observed with respect to the carbon aerogel sample obtained. The bands appear sharper and more separated than the original sample, however the overall organisation of carbon still resemble a disordered graphite with a I_D/I_G ratio of 0.95 which is in good agreement with previously reported values.

4.3.3 Electrochemical test

Carbon dots obtained from CAs have been studied both as carbonaceous electrodes for supercapacitor and in lithium-ion devices in order to investigate the potential of 0D material for electrochemical devices. The same electrodic composition of CAs, i.e. 80:10:10 of active material, acetylene black and PVDF, have been applied and supercapacitor tests were performed only with KOH 6M as the electrolyte.

CD supercapacitors performance

Cyclic voltammetries collected at different scan rates are showed in Figure 4-9. As well as for the CAs samples, the quasi-rectangular shape typical of supercapacitors is almost lost at high scan rate but it is maintained at lower values. In any case, the curves are symmetrical to the horizontal axis, and this can indicate a good reversibility of the charge accumulation. It seems to be no peaks in the curves that could indicate faradic reactions or side processes due to the functionalisation of the surface during CD synthesis, the process still appears totally capacitive with no transformations occurring in the device.

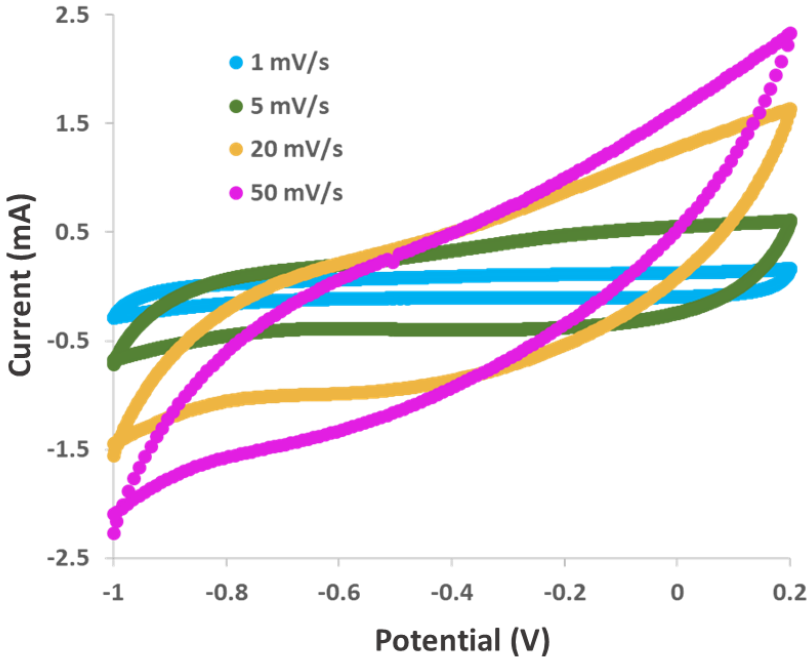

Figure 4-9 Cyclovoltammograms collected at different scan rates for carbon dot electrodes

Capacitance values, calculated by CV using Eq z in chapter 3.3.3, at different scan rate are showed in Figure 4-10 and the range values goes from around $10Fg^{-1}$ at 50 mVs^{-1} to around $53Fg^{-1}$ at $1mVs^{-1}$. As well as for previous experiments capacitance fades with the increase of the scan rate forcing the material to work faster at stressful conditions. with capacitance.

Capacitance offered by carbon dots samples seems to be low compared to literature values, where these materials, both alone and in hybrid materials where CD is usually added to functionalise some carbonaceous structure like carbon nanotubes or graphene oxide, can offer actually outstanding

performances. However, in literature CD are usually applied with different electrolytes such as H_2SO_4 or Na_2SO_4, therefore the comparison only indicates that further studies are needed to extend the library of applied electrolytes.

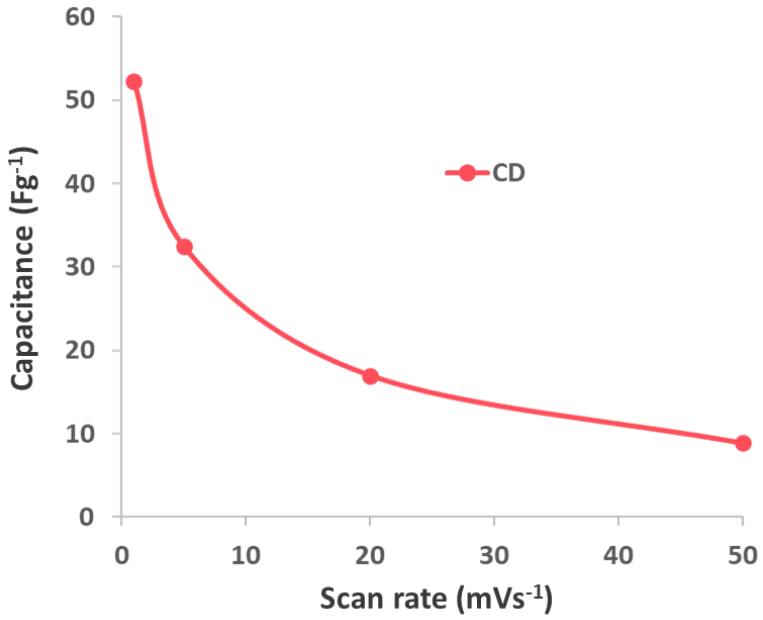

Figure 4-10 Capacitance calculated from CV as a function of the scan rate

Galvanostatic cyclations were also performed on CD-based electrodes and the evolution of potential during a first cycle of discharge and charge at $0.1Ag^{-1}$ is shown in Figure 4-11. A quasi-triangular shape is maintained and confirms the absence of faradic reactions already proved during cyclic voltammetries, however there is a consistent irreversible loss at the begin of the charge process.

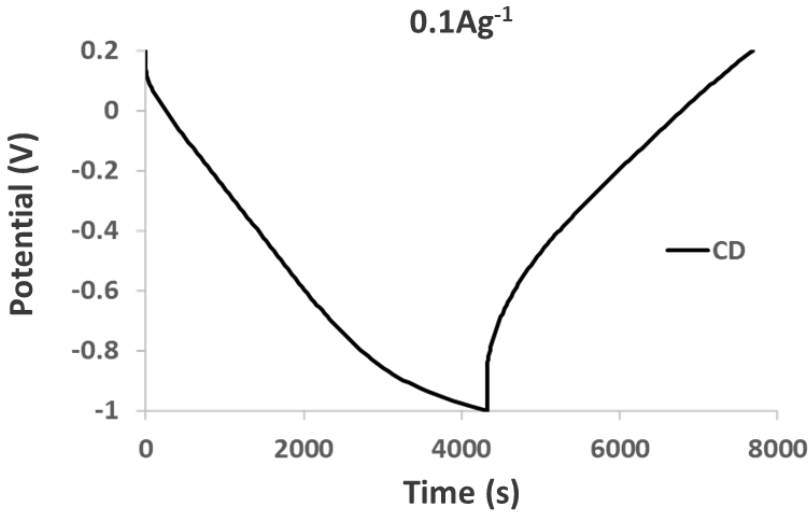

Figure 4-11 evolution of potential during a single cycle of discharge and charge for CD electrode

The potential step at the end of the discharge is almost 0.2V, and after it the potential is maintained pretty linear. This indicates a consistent loss of capacitance and after many cycles it could hinder the device life.

In order to better understand this aspect of the CD electrodes behaviour, the life cycle of a device is shown in Figure 4-12. A CD-based electrode has been cycled at 0.1 Ag^{-1} density of current for a thousand cycles and capacitance was calculated using the same equation proposed in chapter 3.3.3 (Eq 3). After reaching outstanding values in the first cycle (over 100 Fg^{-1}), capacitance fades until reaching a stable trend in the range between the 50th and the 200th cycles around 55 Fg^{-1}.
After the 200th cycle however, a second fast decrease in capacitance occur, and after 1000 cycles the sample reaches performances around 5.2 Fg^{-1}, which is only the 9.4% of retention with respect to the capacitance registered in the interval between cycle 50 and 200.

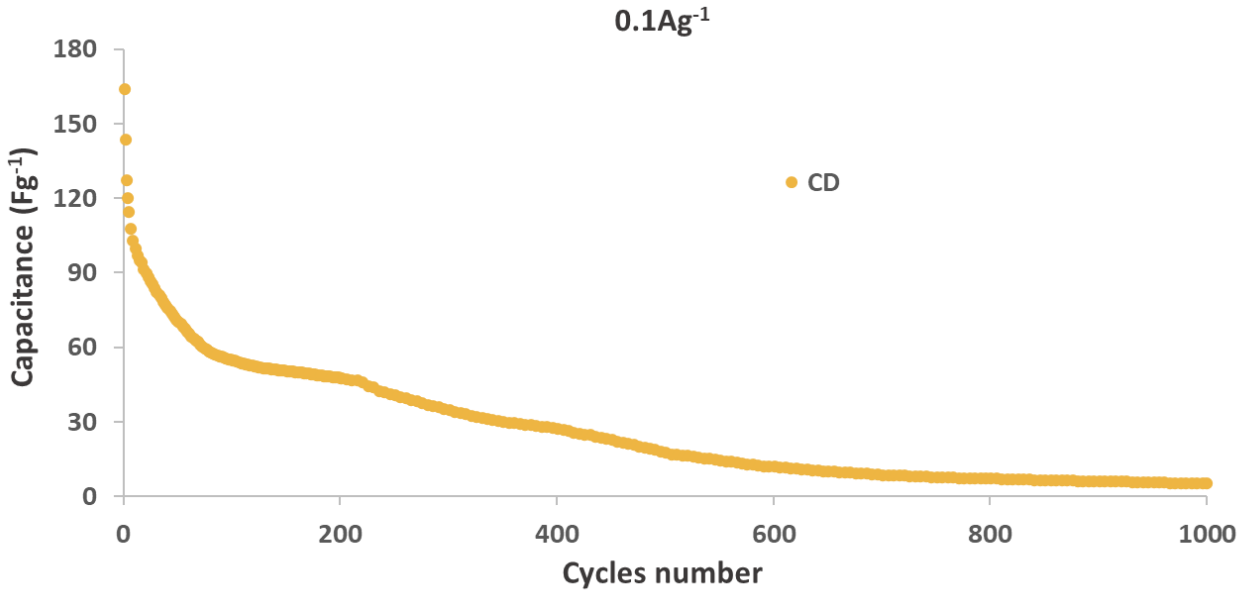

Figure 4-12 life of a CD electrode for prolonged work

It can be concluded that in our system, using KOH as electrolyte, this composition of the electrode mixture and experimental settings, CD do not seem suitable as supercapacitor electrodes, offering low capacitance and also short life. However, since literature still offers promising solution for the application of CD and CD decorated materials as supercapacitors, further investigations on the developed systems seem necessary.

CD Electrochemical performance in Lithium-Ion Batteries

CD were also tested in lithium-ion batteries to evaluate the efficacy of lithiation inside a 0D material with high specific surface. The trend of potential in the first, second, fifth and tenth cycle are shown in Figure 4-13 and since in the first cycle of a lithium-ion device the SEI formation occurs over the anode surface, th first cycle is way longer than the others.
It can be noticed that compare to Figure 3-39 where the discharge and charge cycles of a CAs anode was showed, the first cycle has a different sharp in particular at the beginning of discharge and in general in the shape of all cycles. CAs potential quickly faded until around 1.5V where SEI formation started, on the other hand with CD we observe a less sharp decrease, and the SEI formation seems to start at higher potential. Moreover, comparing the first cycle of CD and CAs t can be noticed that

in Figure 4-13 at the same C rate (i.e. C/10) the first discharge last longer than the CAs first discharge (16.5 against 14 hours) but the charge part of the curve is roughly halved.

Even the shape of subsequent cycles is different comparing CAs and CD. While CAs in Figure 3-39 showed a quick fade below 1V and then a steady decrease until the lower minimum, here the curves show two main mechanism, a first reaction below 1.5V that is compatible with persistent SEI formation even after the first cycle, and then a second reaction below 1V compatible with lithiation of the small graphitic domain of carbon dots.

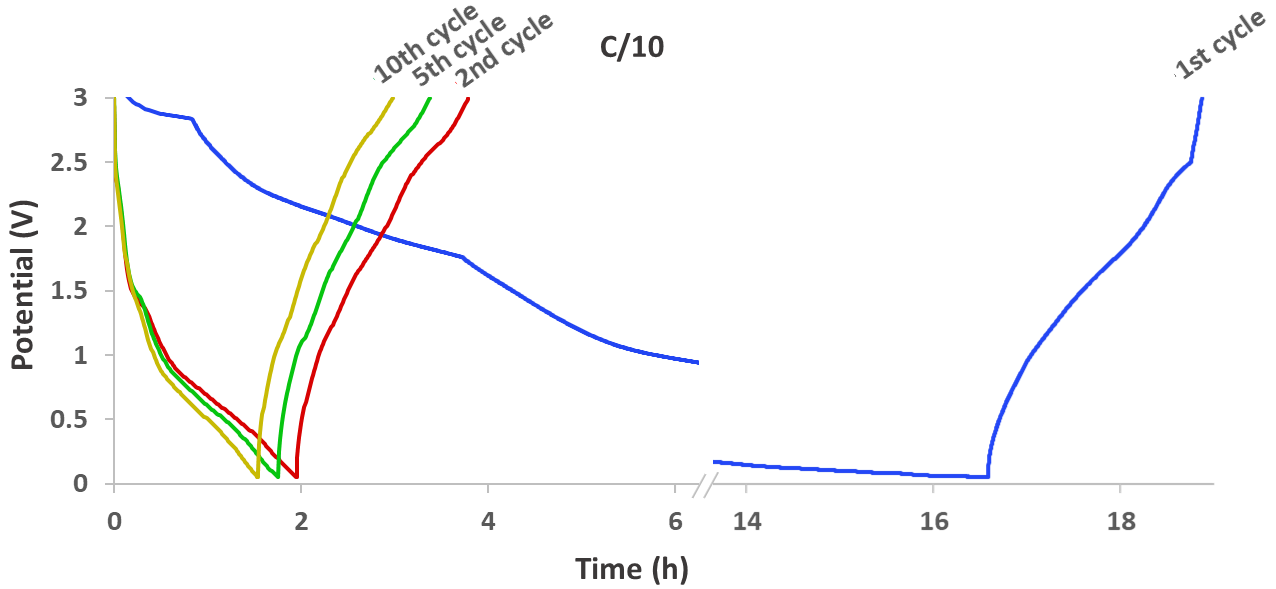

Figure 4-13evolution of potential during a single cycle of discharge and charge of anodes for cycle 1 (blue line). 2 (red line), 5 (green line), and 10 (gold line)

A possible explanation of this behaviour could be a loss in cohesion of the active material on the electrode. Carbon dots have particularly low specific surface and contact with the rest of the electrode even with binder inside the electrode powder, and carbon dots might detach from the rest of the material, thus exposing the underlaying surface. This could lead to the formation of SEI even after the first cycle.

In fact, once the electrochemical tests of CD are over, the separator is found dirty of electrode material, which can happen exactly when the active carbonaceous material is not well retained on the current collector. This continuous loss of capacitance due to the irreversibility of the SEI formation that consumes electrolyte and active surface lead to a consistent loss in capacitance over prolonged cycles.

Looking at Figure 4-14, in fact, the trend of capacitance over a hundred cycles can be seen. Starting from a capacitance slightly below 120 $mAhg^{-1}$, values instantly drop at 100 $mAhg^{-1}$ and are followed by a continuous decrease until reaching values below 40mAh g^{-1} around the 100^{th} cycle, with a retention of 38.6%. Coulombic efficiency on the other hand is soon close to 100% with a slight and temporary loss between the 10^{th} and the 20^{th} cycle.

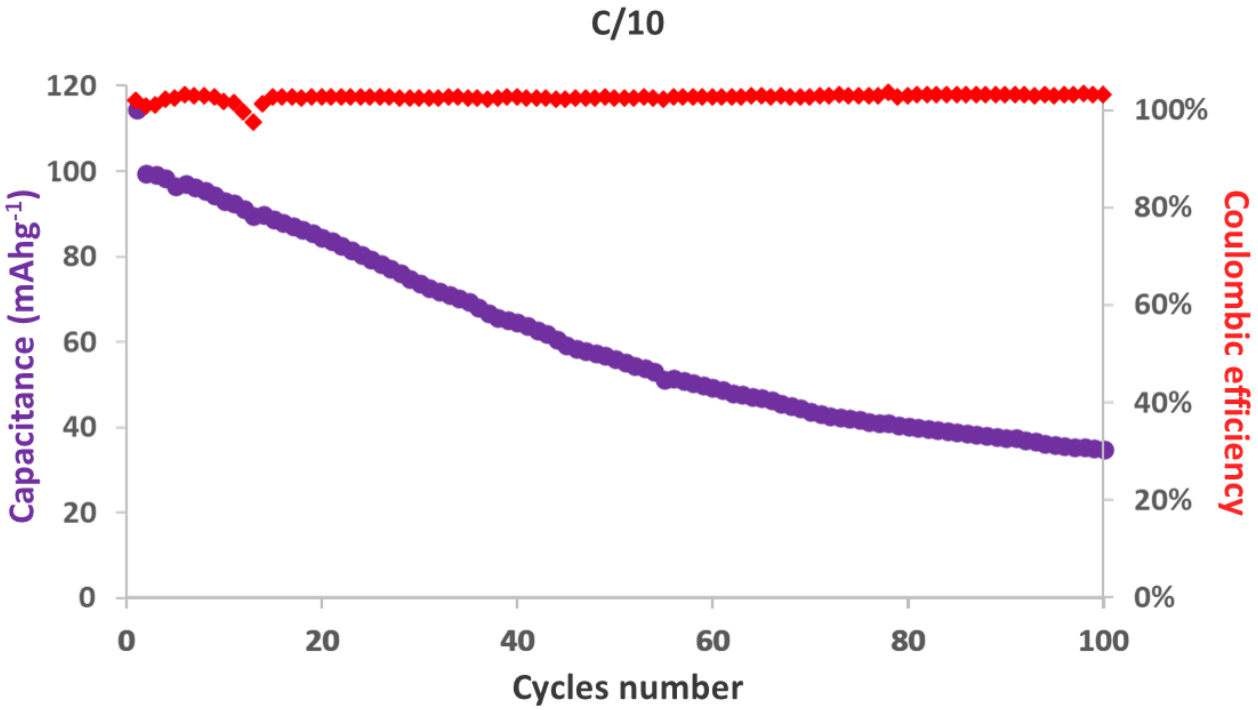

Figure 4-14 capacitance (violet dot) and coulombic efficiency (red diamond) of a CD electrode as a function of cycles number

Comparing 1B CAs to CD it is possible to notice that even if both samples undergo a continuous decrease in performance with CAs offering better initial values, CD actually can offer a better retention of capacitance.

4.3.4 Conclusion

An efficient one-step way to produce Carbon dots have been applied, and the final result is a powder of carbon dots around an average diameter of 28nm confirmed both by SEM and AFM. The CD surface seems functionalised because of the air atmosphere where the synthetic process occurs, while their structure in long and short range seems made of short domains of graphitic nature.
The application of CD as both supercapacitor electrode and lithium-ion anode, has shown that the material has quickly fading performances due probably to a poor contact between the carbon dots and the rest of the electrodic mixture, thus leading to loss in performances, since the electrode is losing active material and electron consuming irreversible reactions that hinders the capacitance. However, CD have demonstrated that they ca n both accumulate charges over the surface and intercalate ions, thus resulting a promising 0D material worth of deeper studies.

5 Advanced characterization: EC-AFM as a powerful tool for studying energy storage devices in operando

5.1 the importance of advanced in operando characterization techniques for functional materials

Numerous ex-situ and preliminary studies can be applied to investigate the structure of materials and their properties.[233] In this study the carbon-based materials have been characterized ex-situ before electrochemical tests by means of SEM, EDX, Raman Spectroscopy, XRD, BET, Tomography and AFM, but many other techniques can be applied to further study a material for energetical application, like FTIR, XPS or TEM.[140,211,234–237] All these different characterizations can easily be applied to study a material before its use and also after it, in a post-mortem analysis, however all of these efforts can only offer information of nature and structure before or after processes occur.[233,238] These techniques can be used to describe the system only before it undergoes its application and then to observe overall transformations, which means that these are just partial information of the real alterations that occurs in a sample, of the real evolution and mechanism of phenomena.[233]

The analysis of a phenomenon by just analysing its resulting product can offer many information and allows to develop interpretations and hypothesis, supported by data, on the system observed. However, the possibility of actually examining the system while it is changing, while it is being tested, could actually offer many more information to truly identifying the mechanism and the evolution of a material.[239] This is what is called in operando analysis: a technique that would allow the study of a process directly in the place where it is occurring (in situ) and when it is occurring, in a real time investigation.[238,240] The proposed techniques present limits and obstacles that hinder the possibility of efficiently adapting systems for in operando measurement, such as necessity of high vacuum for SEM analysis, or inconvenient geometries of the instrument for spectroscopies.[233,238]

In any case, in operando studies are crucial when it comes to functional materials. It allows to deeply examine not just its behaviour and functioning mechanism but also its limits, allowing an operator to effectively intervene on the parameters that are hindering or limiting the outcoming performances.[240,241] Therefore, nowadays, characterization of functional materials should take into account advanced techniques in operando, and this is particularly true also in the field of energy, where achieving such a sophisticated understanding of processes can have the twofold goals of obtaining mechanistic insights for the already known materials and opening new perspectives in the development of new materials with enhanced performances.[239]

Taking as examples the materials produced during this work, the experimental data presented so far, apart from functional tests that give information of electrochemical behaviour of a system, are all data that consider the system prior to its application. All conclusions presented consider the material before the transformations occurring that can only be interpreted by electrochemical data;

however, an actual observation of morphological, structural, and topological modifications is not truly achievable.

It is generally known in lithium-ion batteries that a stable and effective SEI is crucial to achieve high cycling efficiency. A first discharge cycle at low current can actually help the formation of a stable and stress resistant solid electrolyte interphase in carbonaceous electrode. Nevertheless, this stability can be degraded under certain operable battery conditions. There is a huge collection of carbonaceous material applicable for energy storage and best conditions, and most important the mechanism process might actually differ from sample to sample. [242]
For these reasons this study's next steps are considering the study of the electrochemical processes of the proposed material with a in operando AFM-based advanced technique: electrochemical atomic force microscopy (hereinafter EC-AFM).

5.2 EC-AFM: Electrochemical Atomic Force Microscopy

EC-AFM is a technique that combines an Atomic force microscopy along with a potentiostat to apply certain current or potential over the analysed system. it is a well-known technique (a general scheme taken from Chen et al.[243] is showed in Figure 5-1) that has already been studied to characterize materials and to study the mechanism of reactions and synthesis, for example Bertrand et al.[244] observed the modification due to corrosion over the surface of a copper electrode, while Chen et al.[245] investigated the synthesis of polymer/Au nanocomposites. This AFM-based techniques needs to work in liquid, i.e. the electrochemical solution, thus involving all the difficulties of in liquid AFM techniques, such as noisier topography and alterations due to the property of the liquid phase, like bigger resistance to cantilever movements and bigger refractive indexes of liquids that can lead to changes int the optical path of the laser and thus resulting in alteration of the force gradient measured.[233,246,247]

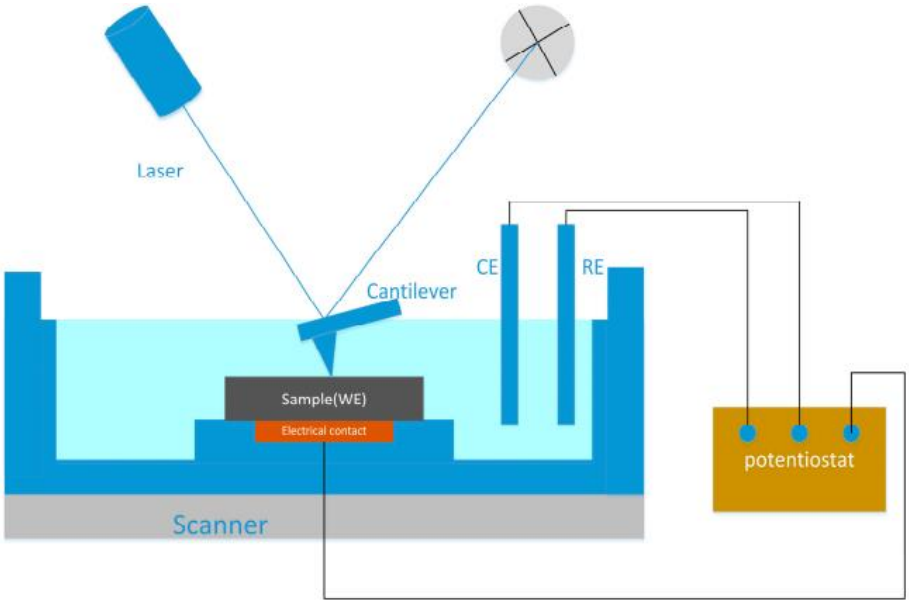

Figure 5-1generic representation of a EC-AFM cell design, image taken from Fig.1 of Chen et al. [243]

Of course, a characterization technique that allows the investigation in situ of electrochemical processes has also been used for energetical application.[247] An example of advanced in situ characterization of lithium-ion batteries is the work of Ramdon et al.[233] that investigated the aging and modification processes occurring over $LiFePO_4$ cathodes in lithium-ion devices.

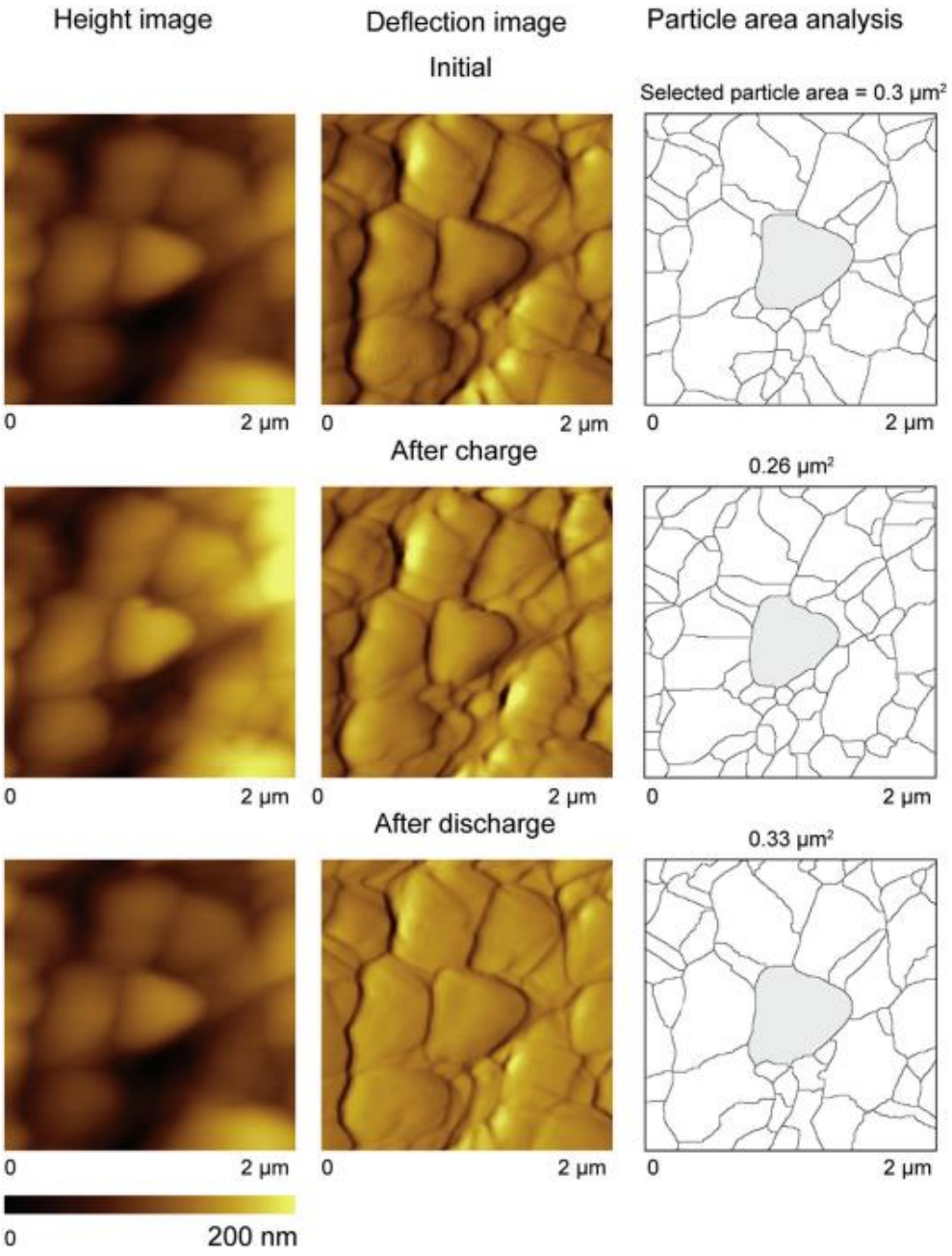

Figure 5-2 Fig. 7 from Ramdon et al.[233] *AFM height and deflection image as well as particle area analysis of LiFePO4 in initial, charged and discharged state.*

In their study, Ramdon et al. wanted to observe the aging phenomenon in Li-ion batteries by in operando observations that could reveal in real time morphological, electrical, and structural changes that occur during cycling. Authors decided to apply EC-AFM and to assemble the cell in dry box to protect the system from degradation. Despite these precautions, and despite this technique might seem ideal to study this system, authors still needed to tune experimental conditions in order to actually observe the phenomenon. For example, a suitable C rate has to be selected and Initial experiments at 1 C and C/6 rates showed that more changes in morphology were observed at C/6 rate. The reason is due to the design of cell in EC-AFM, as shown in Figure 5-1, since the region analysed must be scanned by the tip, the area observed is not actually facing the counter electrode.

This means the counter surface is way inferior to the working electrode's surface and that the area analysed is not facing directly the other electrode.
This creates a heterogenous kinetics over the working electrode with ions diffusion pathways in solution that are actually longer for the different regions. The fractions of the WE actually facing the CE have short pathways, but the scanned area is far from CE and the system needs more time to adjust to the changes imposed by the potentiostat. Sadly, slower C rate also have to deal with the solvent evaporation issue, therefore an optimum value of current must be empirically determined, Ramdon et al. optimized their system around C/6 rate.
AFM images were taken in contact mode using a silicon probe with a 70 nm thick gold reflective coating, and authors used the technique to analyses changes in size for particles. A precise particle evolution is showed in Figure 5-2, it was chosen for its distinct boundaries and separation from surrounding particles and observed with a imaging software, observing a change in order of 25% of the area during battery cyclations. Such a variation was interpreted as the phase change of the particle from the $FePO_4$ phase to the $LiFePO_4$ phase in the outer region of the particles according to a shrinking core model described by Srinivasan et al.[248]
Such a technique could be revealing in the study of the materials proposed in this study. It could enhance the comprehension of the proposed energetical systems and of how to overcome the limitations encountered in the functional tests. Therefore, one of the goals of this project is to further investigate over the application of CAs and CD in electrochemical devices using EC-AFM. The instrument and the cell chosen is the Oxford Instrument Cypher VRS AFM with its electrochemical cell, both showed in Figure 5-3. Such a technique take to the next level our comprehension over those phenomena that are supposed to hinder our processes, like the SEI formation and the loss of capacitance depicted in chapters 3.3.3 and 4.3.3.

Figure 5-3 AFM Cypher VRS instrument and electrochemical cell for integrated EC-AFM

Despite the potential of this instrument and of EC-AFM technique, still, they both present limits that make this technique difficult to apply in all systems. For example, the necessity of a lithium-ion device to work in total absence of humidity and in oxygen-free conditions, makes difficult to investigate systems based on lithium ions when the AFM instrument is not contained in dry room

or at least dry box where the atmosphere can be controlled. The cell is forced to be open since the probe must scan its surface and this hinders us, for now, from observing out material modifications in lithium-ion devices.
Therefore, in the near future efforts are moving over the study of the modifications of carbonaceous electrode surface during charge accumulation. However, again, instrumental limits must be taken into account: the instrument cell is made of certain materials that have their chemical compatibilities. For example, a certain concentrated aggressive chemical specie could be detrimental to the instrumental components, and this would make the measurement not only impossible to be collected, but also damaging for an advanced expensive instrument.
Therefore, this chapter will illustrate our efforts in trying to adapt our system for in operando EC-AFM analysis including our future goals and perspectives.

5.3 Results and discussion

The scope of the study presented in chapter 3.3.3, *Supercapacitors Performances with different electrochemical solutions*, was actually aimed at the identification of the best possible solution to overcome the chemical compatibility limitation of the Cypher VRS AFM electrochemical cell. Since its materials should be working in a pH range consistently lower than that provided by a 6M strong base solution, and since K^+ cations are not compatible with the materials, another solution is necessary.
The starting idea was to study a compatible cation like Na+ and reducing its concentration step by step, in order to first determine if similar performances were achieved. Anyhow, as shown in chapter 3.3.3 in Figure 3-37, the concentration of the base in the electrolyte actually plays a fundamental role in the final performances of the electrodes, and the capacitance is abruptly reduced by it. The idea of using strong bases like KOH or NaOH was then abandoned, and future study will focus on new solvents like acidic solution (H_2SO_4) or salts (Na_2SO_4), that are already used in literature as electrolytes for capacitors, in particular for CD electrodes.[249,250]
Meanwhile, since it is necessary to observe changes on the electrodic surface during cyclations, it was necessary to preliminary observe the possibility of actually efficacy performing imaging of the electrodic surfaces and determining changes before and after cyclations, in a post-mortem ex situ AFM measurement. This measurement of simple topography ex situ had to be proven with in liquid AFM technique, a preliminary study in air was conducted.

5.3.1 Post-mortem AFM analysis of electrodes in air

AFM measurements in air were performed on 1B CAs based electrodes before and after cycling in KOH 1M. Both samples were fixed on the stage by using conductive scotch tape. Image acquiring was conducted in tapping mode on a Veeco AFM Multimode equipped with Nanoscope IIIa and using a RTESP Bruker tip with nominal parameters: radius 8 nm, frequency 300 kHz, spring constant 40 N/m. Images were recorded with a 512 × 512 pixels resolution and corrected by polynomial background filters using the software Gwyddion 2.31. This software was also used to calculate surface roughness of samples.

The goal of this measurement is to efficacy study the possibility of detecting surface modifications over the carbonaceous electrodes applied as supercapacitors in order to demonstrate the prospect of studying in operando the morphology surface change of the electrode over cycling. AFM platform of both Veeco AFM Multimode and Cypher VRS AFM both allow routinary investigation of the morphology in air, and also analysis in liquid and in operando.

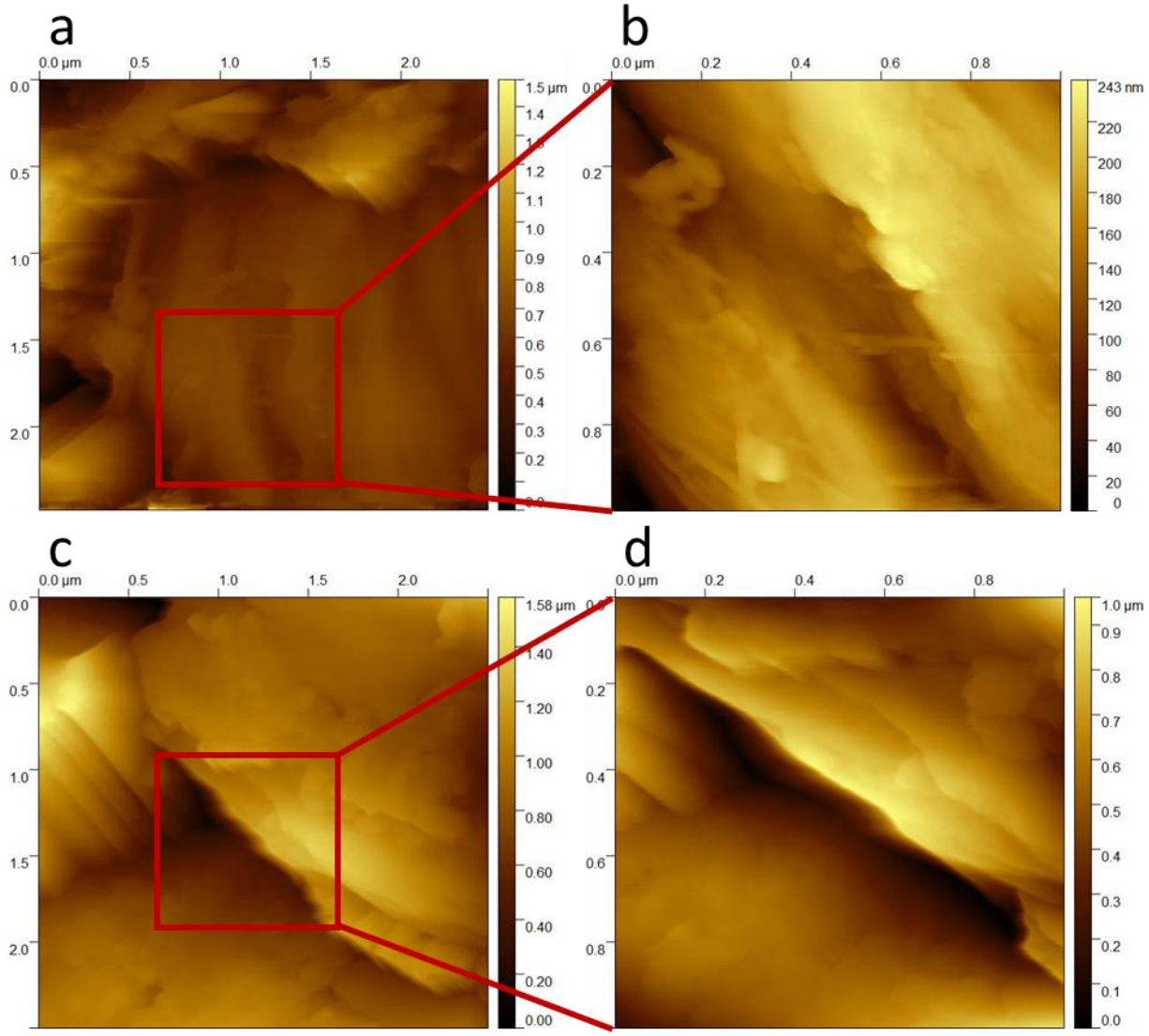

Figure 5-4 AFM images of: pristine electrode 2.5 x 2.5 µm² area (a) and 1 x 1 µm² area (b); post-mortem electrode after cycling in 1M KOH 2.5 x 2.5 µm² area (c) and 1 x 1 µm² area (d).

The acquired images are shown in Figure 5-4, where pristine uncycled electrode are shown in section a and b, while section c and d show the same magnification of a electrode at the end of his life. Images suggest that the surface undergoes a dramatic transformation over cycling. Pristine electrode is characterized by the presence of short and well detached fibrotic structures, which are clearly visible especially in panel (b), coupled with very small round-shaped agglomerates and in general characterized by a rough surface.

Conversely, after cycling, the electrode seems to lose its nanostructure. In fact, nanometric fibres are not visible anymore, while micrometric platelets forming overlapped terraces appear. Such morphological differences qualitatively described above have a quantitative correspondence in the surface roughness, which goes from 36 nm for 1 x 1 μm^2 pristine sample area to 131 nm for 1 x 1 μm^2 post-mortem sample.

AFM post-mortem images demonstrate that during cycling changes and modifications occur over the surface and that the main change is the removal of active material, and in general electrodic mixture, from the electrode. Thus, leading to the loss of capacitance and performances. The small round-shaped agglomerates that are lost in the cycled material are probably detached from the surface and this conclusion seems in good agreement with the hypothesis of chapters 3.3.3 and 4.3.3.

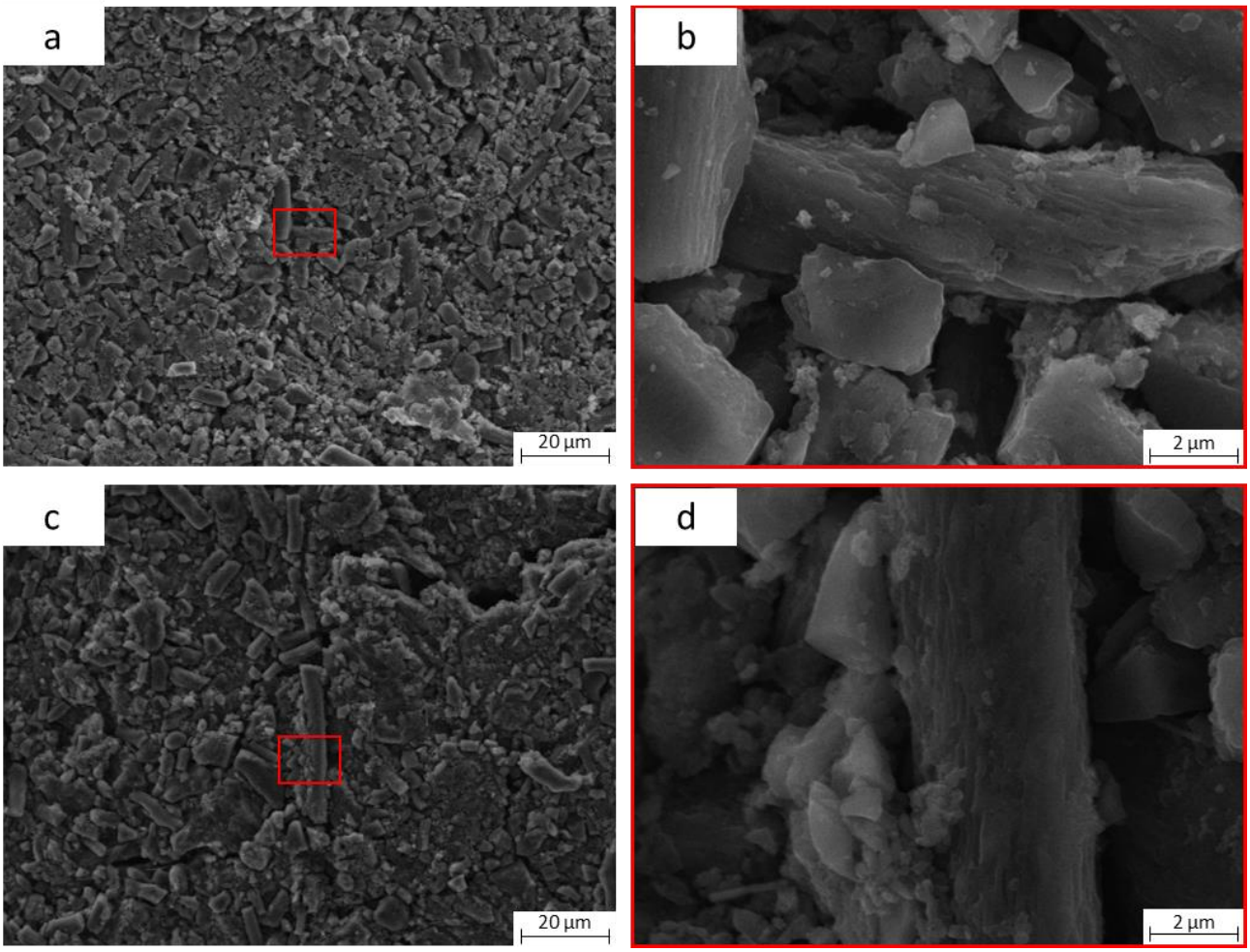

Figure 5-5 SEM micrographs of pristine 1B CAs electrode at 20k and 2k magnifications (respectively a and b) and post-mortem 1B CAs electrode cycled in KOH 1M at 20K and 2K magnifications (respectively c and d)

Therefore, AFM analysis confirms the empirical observations derived from electrochemical data and at the same times works as a first proof of principle of the possibility of obtaining mechanistic insight of the CAs and CD-based carbonaceous electrodes functional performances.

In order to confirm the observation and the conclusions obtained from AFM topography, SEM analysis was also applied over pristine and cycled electrodes and images are shown in Figure 5-5. SEM analysis was performed using a TESCAN Vega thermoionic scanning electron microscopy, and

the results show that the pristine surface actually seem made of short fibrotic elements surrounded by a compact matrix of smaller structures that holds together the electrodic material. Such a matrix being composed by the electrodic mixture assures active surface for charge accumulation and reactions and also guarantees the charge conduction along the surface. In the cycled electrode (c and d of Figure 5-5) the electrode seems more cleaned on the surface. Cyclations have detached the smaller structure of the material from the electrodic matrix and thus leading to the loss of active material and the decline of conductivity of electron among the material. Such detachment could be due both to a low contact and cohesion between the electrodic component, but also to an aggressive electrolyte, KOH is a strong base.

5.4 Conclusion and future perspective: AFM in liquid and in operando

AFM analysis in air confirms the hypothesis made in chapter 3.3.3, is a preliminary proof of principle for the perspective of applying AFM system for future studies and also allowed to identify a possible strategy to improve the material performance, i.e. moving to a milder electrolyte and increase the cohesion of electrodic mixture.

In order to move to C-AFM analysis, however, a second test must be performed: since the techniques is meant to work in liquid (i.e. the electrolyte), it is necessary, after having demonstrate the possibility of detecting differences in air, to demonstrate that the same thing can be done in liquid. This technique brings all the issue already described in chapter 5.1 and requires first to test the materials in different solutions, like Na_2SO_4. Once this second step is performed the functional in operando characterization with electrochemical AFM will take place.

The idea of using EC-AFM involves the assembling of a three-electrode electrochemical cell into the AFM sample holder and to apply the desired electrochemical conditions (i.e. a certain potential or current value). The study of the surface of the working electrode change over cycling will provide mechanistic insights into the device life, giving indications on the possible material improvements.

The work presented in this study has brought the research over carbonaceous material taken into consideration to open broad perspectives regarding the structural and functional characterization of material for energy transition.

6 Appendix – XRD Characterization

Along with the main project discussed in the previous chapters, during the PhD I had the opportunity of working autonomously with X-Ray Diffractometer and achieving expertise with this technique. Thanks to the knowledge acquired I was able to develop independent collaborations with other research groups and make service measurement for other projects and works, which resulted in extra publications co-authored by other members of the research group I belong to and researchers from other departments.

XRD spectra have been collected using a BRUKER D8 ADVANCE diffractometer in Bragg-Brentano geometry equipped with Mo tube (Kα 0.71 Å) available at CNIS-SNN Lab (Research center on nanotechnologies applied to engineering - Laboratory for Nanotechnologies and Nanosciences of Sapienza) in various 2Θ range, voltage, current and step size according to the particular sets of samples. In the following paragraphs, two of the most significant examples of the performed measurements will be briefly described.

6.1 Study of calcium carbonate polymorphs for biorestoration.

A notable example of this collateral activity is the contribution offered to the group of Prof. T. Rinaldi from the Department of Biology and Biotechnology of Sapienza Charles Darwin, and in particular to the PhD student of her group Francesca Benedetti. This work is aimed at the biorestoration of cultural heritage, and in particular towards the use of biogenic calcium carbonate to repair damaged surfaces of calcareous minerals, such as travertine, calcarenite or marble.

To counteract the natural degradation of stone artworks, eco-friendly solutions such as bacterial biomineralizations are being studied and this project is aimed at the exploitation of both pure cultures and indigenous bacteria naturally found over the surface of minerals to induce biomineralization and restore ruined surfaces of artworks. Thanks to XRD investigation it was possible to investigate the polymorph of $CaCO_3$ produced *via* this method, to investigate over the best combination of bacterium and cultural medium to obtain the desired crystalline lattice and to deep understand the nature of the process of biorestoration when these bacteria are generating calcium carbonate over the surface of minerals.

Calcium carbonate exists in three main polymorphs, namely calcite, the most stable in nature, vaterite, a metastable phase that naturally transforms into calcite, and aragonite. Artwork in the world are made of calcite lattice with different morphology and porosity that discriminates between different carbonate rocks. By means of XRD we studied both what is produced by bacteria alone and what is produced by bacteria on the surface of minerals.

In the first study, made with pure bacteria cultures in two different cultural media (namely YPDuc and BPuc), it has been observed that bacteria tend to produce vaterite. Despite being a metastable phase, the thus obtained vaterite is maintained even after six months from its synthesis. XRD spectra collected for the first part of this work are shown in Figure 6-1. Spectra from *a* to *c* were collected

on $CaCO_3$ produced with a first medium, while spectra from *d* to *g* with a different one and it can be seen that the relative quantities of calcite and vaterite can vary in the different samples but pure bacteria (samples from *a* to *f*) tend to produce vaterite as the main component. Calcite can only be seen only for a few weak peaks with YPDuc (*a-c*) medium and as a minority component with BPuc (*d-f*). However, when BPuc is used with microbial community native of a calcareous mineral, vaterite peaks become very low and calcite seems the predominant component.

This first study demonstrated that it is possible to tune the yield of one polymorph by adjusting conditions, i.e. by feeding the chosen bacterium with corresponding medium. In any case however, being the artworks made of calcite instead of vaterite. Only calcite can actually restore the ruined surfaces without changing it and efficiently restoring the artwork. For this reason, the carbonatogenesis was studied not in vitro but also on the surface of minerals.

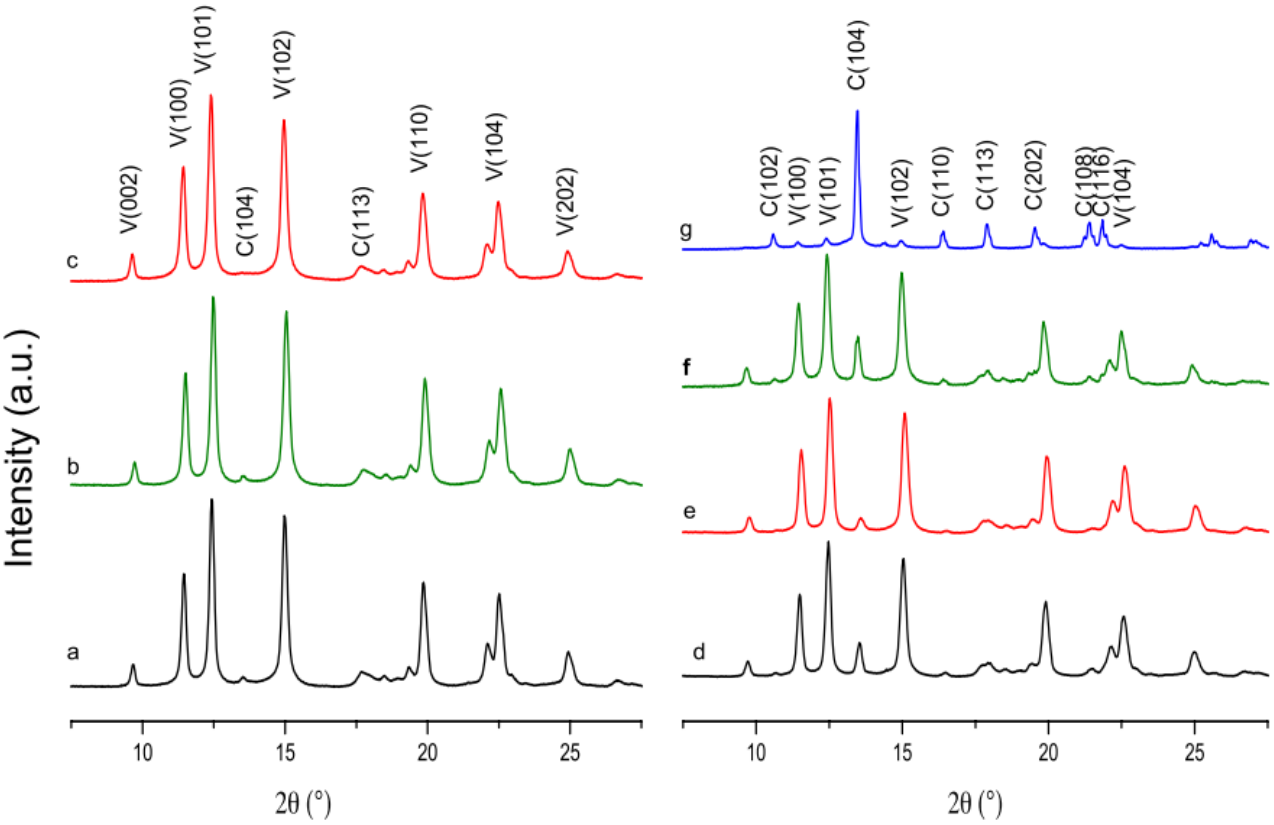

Figure 6-1 XRD diffractograms of the of biogenic $CaCO_3$ precipitates. In the left spectra calcium carbonate produced by (a) L. fusiformis 3.20 (b) P. psychrodurans 7Mo (c) L. lenta Vetro 1 in YPDuc breeding ground are shown. In the right spectra calcium carbonate produced by (d) L. fusiformis 3.20 (e) P. psychrodurans 7Mo (f) L. lenta Vetro1 and (g) microbial community in BPuc breeding grounds are shown. Peaks of Vaterite (V) and Calcite (C) are assigned over each peak.

When carbonatogenesis occurs over the surface of a mineral, the calcium carbonate precipitates over preexisting crystalline planes. For this reason, the following step of the study currently in progress is focusing on the applicative study of the biogeneration directly on the minerals surfaces. Preliminary results obtained so far suggest that once in contact with minerals of calcium carbonate, the $CaCO_3$ produced generates crystalline seeds that continues to grow over the preexisting crystalline planes of calcite, thus producing actually calcite even when in vitro the same bacterium with the same breeding ground used to make vaterite.

6.2 Study of the strain induced by Ge doping in Si lattice.

This second example illustrates my contribution to a project developed in the same group I belong to, by PhD students Giancarlo La Penna, Chiara Mancini and Anacleto Proietti, all under the supervision of Prof. M. Rossi. The aim of this project is the detection and evaluation of the strain in crystalline silicon lattice induced by the substitutional doping of Ge in the silicon crystals. The introduction of Ge in the lattice induces a distortion of crystalline planes and an increase in this parameter. Since XRD is sensitive to the plane distance, it has been hypothesized that the phenomenon could be investigated by using this technique, besides Raman spectroscopy and tip enhanced Raman Spectroscopy (TERS).

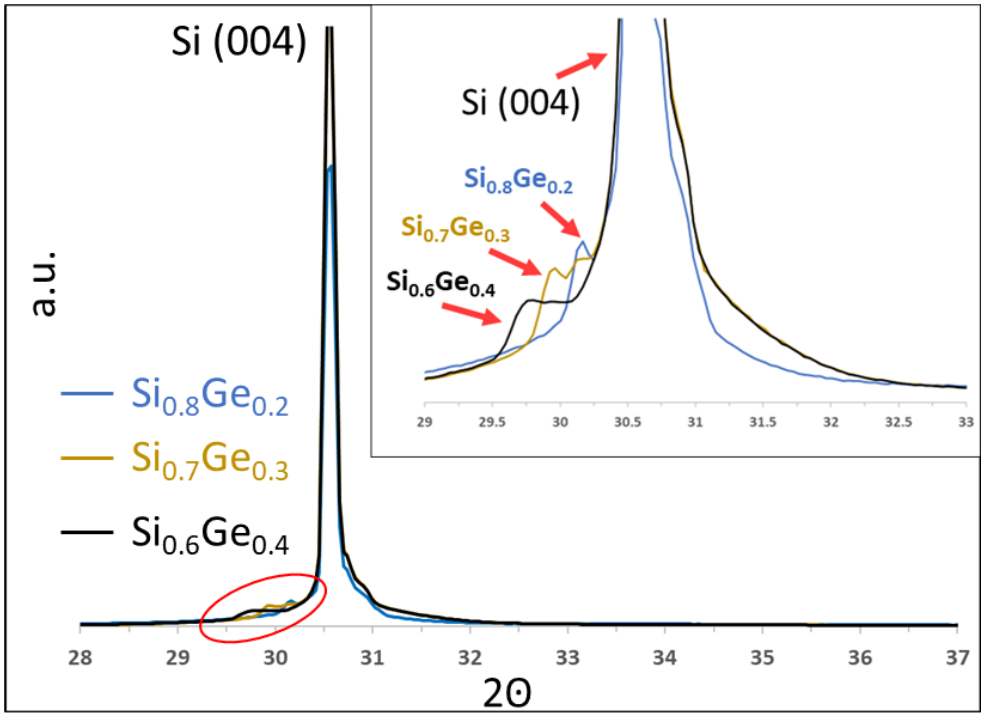

Figure 6-2 XRD spectra of three different samples of $Si_{1-x}Ge_x$ thin film grown over Si crystal in the range of Si (004) peak, with insert of a magnification of the circled area

More in detail, the shift of some specific peaks at different angles could indicate a strain internal to the crystal lattice, higher plane distance meaning lower 2Θ angle according to Bragg's Law.
The observed samples were made of a thin (from 20 to 50 nm) film of $Si_{1-x}Ge_x$ with x in the range from 0.2 to 0.4, grown over a crystalline (004) Si lattice. Since X ray penetrates several microns deep into the investigated sample, however, the signal of Si (004) is predominant. In any case, thanks to the high power (over 2kW) reached by the available instrument it has been possible to discriminate the signal of a nanodimensional film as a small lateral peak in the left trail of Silicon (004) peaks, representing the same reflection when there is strain induced by the presence of germanium.
As shown in Figure 6-2 this strain, and so the shift in 2Θ position of the peak, is higher for samples with higher germanium content. These results demonstrate the possibility of studying the strain induced by a heteroatom (Ge) in the crystalline domains of Si.

7 List of Research Products

7.1 Papers

1) T. Singh; P. Atanasio; D. Schiavi; V. Di Lorenzo; F. A. Scaramuzzo; D. Passeri; G. M. Balestra; M. Rossi, "Preliminary Results Towards the Mechanical Characterization of Cellulose Nanofibers Using HarmoniX Mode Atomic Force Microscopy, AIP Conf. Proc., 2021, 2416, 020011
2) F.A. Scaramuzzo, M. Pasquali, P. Atanasio, E. Gualtieri. “Caratterizzazione elettrochimica di celle al litio o di celle ibride ad alligazione/conversione con anodi a base di nanostrutture di silicio o elettrodi ibridi silicio/carbonio”. Report tecnico ad ENEA e Ministero della transizione ecologica RdS/PTR2021/253
3) F. Benedetti, M. Kratter, P. Atanasio, F. Mura, M. Beccaccioli, J. Scifo, M. Rossi, L. Nigro, T. Rinaldi. "Isolation of carbonatogenic bacteria for biorestoration", Journal of Cultural Heritage, 2023, 64, 282-289

7.2 Patents

1) P. Atanasio, F.A. Scaramuzzo, M. Rossi, M. Pasquali, A. Capasso, “Elettrodi ibridi carbonio/materiale attivo per accumulatori agli ioni di litio Carbon/active material electrodes for lithium ion batteries”, patent IT202100017024A1

7.3 Oral Presentations

1) P. Atanasio (presenting author), N. Lisi, F. A. Scaramuzzo, M. Rossi, M. Pasquali. Preparation of Carbon/ Silicon Hybrid Nanostructured Anodes for Lithium ion Batteries by CVD and Liquid Phase Deposition. Nanoinnovation 2021, 24 settembre 2021.
2) P. Atanasio (presenting author), F. A. Scaramuzzo, M. Pasquali, M. Rossi. Structural and electrochemical characterization of cellulose derived carbon aerogels. Giornate dell'elettrochimica Italiane, 18 settembre 2023, Cefalù.
3) P. Atanasio (presenting author), F. A. Scaramuzzo, A. Proietti, M. Pasquali, M. Rossi. Rice Husk Waste- Derived Carbon Aerogels: A Sustainable Approach for Advanced Supercapacitor Electrodes. Nanoinnovation2023, 22 settembre 2023, Roma.
4) F. Benedetti (presenting author), M. Kratter, P. Atanasio, L. Buccini, D.Passeri, M. Rossi, F. Trippetta, T. Rinaldi, "Biomineralization activity of bacteria for ornamental stones restoration". The Geoscience paradigm: resources, risk and future perspectives, 2023, Potenza.
5) F. Benedetti (presenting author), M. Kratter, P. Atanasio, F. Mura, F. Trippetta, S. Ronca, M. Brandano, M. Rossi, O. Russina, T. Rinaldi. Applications of the microbially induced calcium carbonate precipitation. XXI INQUA Congress 2023, Roma.

7.4 Poster Presentation

1) P. Atanasio (presenting author), N. Lisi, F. A. Scaramuzzo, M. Rossi, M. Pasquali (2021). Preparation of carbon/silicon hybrid nanostructured anodes for lithium ion batteries by CVD and liquid phase deposition. Nanoinnovation2021. Roma.
2) P. Atanasio (presenting author), E. Gualtieri, F. A. Scaramuzzo, M. Pasquali, M. Rossi (2022). Rice Husk Derived Carbon Aerogels for Supercapacitor Applications. Advanced Inorganic Materials AIM 2022, Bari.
3) P. Atanasio (presenting author), F. A. Scaramuzzo, N. Lisi, F. Mura, M. Rossi, M. Pasquali (2022). Innovative CNW/Si nanoparticles composites architectures as electrodes for lithium-ion batteries. Giornate dell'elettrochimica italiana 2022, Orvieto.
4) P. Atanasio (presenting author), F. A. Scaramuzzo, M. Pasquali,M. Rossi. Facile synthesis of carbon aerogels for supercapacitors from Rice husk agricultural wastes. FEMS EUROMAT2023, Francoforte.
5) P. Atanasio (presenting author), F. A. Scaramuzzo, A. Proietti, M. Pasquali,M. Rossi. Rice Husk Waste- Derived Carbon Aerogels: A Sustainable Approach for Advanced Supercapacitor Electrodes. Nanoinnovation2023, Roma.
6) E. Gualtieri (presenting author), P. Atanasio, F. A. Scaramuzzo, A. Dell'Era M. Pasquali (2022). Silicon/ carbon composite anodes from rice husk for lithium-ion batteries: optimizing the Si/C ratio to enhance battery performances and durability. Advanced Inorganic Materials AIM 2022, Bari.

8 Acknowledgement

Supervisor of this PhD thesis, Prof. Marco Rossi and cosupervisor Prof. Francesca A. Scaramuzzo must be thanked or their guide and proactive participation in the realization of this project, along with Prof. Antonio D'Alessandro, director of the Interdepartmental research centre on nanotechnologies applied to engineering of Sapienza (CNIS) and Prof. Mauro Pasquali, in charge of Element Laboratory of SBAI Department, for their collaboration and the possibility of working in their laboratories.

I must also thank Prof. Roberto Li Voti, Director of Department of Basic and Applied Science for Engineering (SBAI) of Sapienza for having allowed me to work on this interesting topic along with the PhD coordinator of the PhD school of Mathematical Models for Engineering, Electromagnetism and Nanoscience, Prof. Lorenzo Giacomelli.

For their valuable help and fruitful discussion with analysis I also want to thank Prof. Andrea Balducci from the Institute for Technical Chemistry and Environmental Chemistry, University of Jena "F. Schiller", and Center for Energy and Environmental Chemistry (CEEC), Jena, Germany, along with Sapienza's professors, technicians and PhD coworkers: Prof. Daniele Passeri, Dr Rubia Y. S. Zampiva, Dr Francesco Mura, Dr Gianluca Zanellato, Dr. Stefano Graziani, Dr. Anastasia Fornari, Dr. Luca Buccini, Dr. Giancarlo La Penna, Dr. Chiara Mancini, Dr. Anacleto Proietti.

I also want to acknowledge the support of: (i) project Infrastructure for ENergy TRAnsition aNd Circular Economy @ EuroNanoLab (iENTRANCE@ENL) and its partners; (ii) ENEA (Agenzia nazionale per le nuove tecnologie, l'energia e lo sviluppo economico sostenibile) for the three-year 2022-2024 plan of research on national electric system (PIANO TRIENNALE DI REALIZZAZIONE 2022-2024 DELLA RICERCA DI SISTEMA ELETTRICO NAZIONALE).

9 Bibliography

1. Berardi, U. & Jafarpur, P. Assessing the impact of climate change on building heating and cooling energy demand in Canada. *Renewable and Sustainable Energy Reviews* **121**, (2020).
2. Bobrova, Y., Eyre, N., Fawcett, T., Nolden, C. & Papachristos, G. Energy supply/ demand policy asymmetry: A meta-narrative review for a systems explanation. *Science Talks* **5**, 100125 (2023).
3. Dawood, F., Anda, M. & Shafiullah, G. M. Hydrogen production for energy: An overview. *International Journal of Hydrogen Energy* vol. 45 3847–3869 Preprint at https://doi.org/10.1016/j.ijhydene.2019.12.059 (2020).
4. Londoño-Pulgarin, D., Cardona-Montoya, G., Restrepo, J. C. & Muñoz-Leiva, F. Fossil or bioenergy? Global fuel market trends. *Renewable and Sustainable Energy Reviews* **143**, (2021).
5. IEA—International Energy Agency. *Https://Www.Iea.Org/Data-and-Statistics*.
6. Tian, J., Yu, L., Xue, R., Zhuang, S. & Shan, Y. Global low-carbon energy transition in the post-COVID-19 era. *Appl Energy* **307**, (2022).
7. Lu, W. C. The impacts of information and communication technology, energy consumption, financial development, and economic growth on carbon dioxide emissions in 12 Asian countries. *Mitig Adapt Strateg Glob Chang* **23**, 1351–1365 (2018).
8. Shao, X., Zhong, Y., Liu, W. & Li, R. Y. M. Modeling the effect of green technology innovation and renewable energy on carbon neutrality in N-11 countries? Evidence from advance panel estimations. *J Environ Manage* **296**, (2021).
9. Tzeremes, P., Dogan, E. & Alavijeh, N. K. Analyzing the nexus between energy transition, environment and ICT: A step towards COP26 targets. *J Environ Manage* **326**, (2023).
10. Yue, T., Shen, B. & Gao, P. Carbon material/MnO2 as conductive skeleton for supercapacitor electrode material: A review. *Renewable and Sustainable Energy Reviews* vol. 158 Preprint at https://doi.org/10.1016/j.rser.2022.112131 (2022).
11. Zhang, Z. *et al.* Recent advances in carbon dioxide utilization. *Renewable and Sustainable Energy Reviews* vol. 125 Preprint at https://doi.org/10.1016/j.rser.2020.109799 (2020).
12. Kakoulaki, G. *et al.* Green hydrogen in Europe – A regional assessment: Substituting existing production with electrolysis powered by renewables. *Energy Convers Manag* **228**, (2021).
13. Balibar, S. Energy transitions after COP21 and 22. *Comptes Rendus Physique* vol. 18 479–487 Preprint at https://doi.org/10.1016/j.crhy.2017.10.003 (2017).
14. United Nation Climate Change Conference COP26 GOALS. https://webarchive.nationalarchives.gov.uk/ukgwa/20230311034236/https://ukcop26.org/cop26-goals/.
15. Energy Institute - Statistical Review of World Energy (2023) – with major processing by Our World in Data. “Share of primary energy consumption that comes from renewables – Using the substitution method” [dataset]. Energy Institute, “Statistical Review of World Energy” [original data]. *2023*.

16. Minakshi, M. & Wickramaarachchi, K. Electrochemical aspects of supercapacitors in perspective: From electrochemical configurations to electrode materials processing. *Progress in Solid State Chemistry* vol. 69 Preprint at https://doi.org/10.1016/j.progsolidstchem.2023.100390 (2023).
17. *Dresselhaus*. www.nature.com (2001).
18. Soloveichik, G. L. Battery technologies for large-scale stationary energy storage. *Annual Review of Chemical and Biomolecular Engineering* vol. 2 503–527 Preprint at https://doi.org/10.1146/annurev-chembioeng-061010-114116 (2011).
19. Mansi *et al.* Recent advances on core-shell metal-organic frameworks for energy storage applications: Controlled assemblies and design strategies. *Coordination Chemistry Reviews* vol. 499 Preprint at https://doi.org/10.1016/j.ccr.2023.215497 (2024).
20. Ren, W. *et al.* Metallized stacked polymer film capacitors for high-temperature capacitive energy storage. *Energy Storage Mater* **65**, (2024).
21. Rajkumar, P., Thirumal, V., Radhika, G., Yoo, K. & Kim, J. Facile preparation of bio-waste-derived porous carbon for high-performance electrode material for energy storage applications: Li-ion capacitor and Li-ion batteries. *Biomass Convers Biorefin* (2024) doi:10.1007/s13399-024-05300-2.
22. Boretti, A. A market opportunity in power generation for hydrogen energy storage systems. *International Journal of Hydrogen Energy* Preprint at https://doi.org/10.1016/j.ijhydene.2023.07.162 (2023).
23. Tawalbeh, M., Khan, H. A. & Al-Othman, A. Insights on the applications of metal oxide nanosheets in energy storage systems. *Journal of Energy Storage* vol. 60 Preprint at https://doi.org/10.1016/j.est.2023.106656 (2023).
24. Tawalbeh, M., Al-Othman, A. & El Haj Assad, M. Graphene oxide – Nafion composite membrane for effective methanol crossover reduction in passive direct methanol fuel cells. *2018 5th International Conference on Renewable Energy: Generation and Applications (ICREGA)* (2018).
25. Sharaf, O. Z. & Orhan, M. F. An overview of fuel cell technology: Fundamentals and applications. *Renewable and Sustainable Energy Reviews* vol. 32 810–853 Preprint at https://doi.org/10.1016/j.rser.2014.01.012 (2014).
26. Wilberforce, T., Alaswad, A., Palumbo, A., Dassisti, M. & Olabi, A. G. Advances in stationary and portable fuel cell applications. *Int J Hydrogen Energy* **41**, 16509–16522 (2016).
27. Hu, C., Liu, D., Xiao, Y. & Dai, L. Functionalization of graphene materials by heteroatom-doping for energy conversion and storage. *Progress in Natural Science: Materials International* vol. 28 121–132 Preprint at https://doi.org/10.1016/j.pnsc.2018.02.001 (2018).
28. Hassan, N. Catalytic performance of nanostructured materials recently used for developing fuel cells' electrodes. *International Journal of Hydrogen Energy* vol. 46 39315–39368 Preprint at https://doi.org/10.1016/j.ijhydene.2021.09.177 (2021).

29. Meesala, Y., Jena, A., Chang, H. & Liu, R. S. Recent Advancements in Li-Ion Conductors for All-Solid-State Li-Ion Batteries. *ACS Energy Letters* vol. 2 2734–2751 Preprint at https://doi.org/10.1021/acsenergylett.7b00849 (2017).
30. Saddique, J. *et al.* Opportunities and challenges of nano Si/C composites in lithium ion battery: A mini review. *Journal of Alloys and Compounds* vol. 978 Preprint at https://doi.org/10.1016/j.jallcom.2024.173507 (2024).
31. You, S., Tan, H. T., Wei, L., Tan, W. & Chao Li, C. Design Strategies of Si/C Composite Anode for Lithium-Ion Batteries. *Chemistry - A European Journal* vol. 27 12237–12256 Preprint at https://doi.org/10.1002/chem.202100842 (2021).
32. Xu, J. *et al.* High-Energy Lithium-Ion Batteries: Recent Progress and a Promising Future in Applications. *Energy and Environmental Materials* vol. 6 Preprint at https://doi.org/10.1002/eem2.12450 (2023).
33. Yu, J. *et al.* Uniform carbon coating on silicon nanoparticles by dynamic CVD process for electrochemical lithium storage. *Ind Eng Chem Res* **53**, 12697–12704 (2014).
34. Roy, P. & Srivastava, S. K. Nanostructured anode materials for lithium ion batteries. *Journal of Materials Chemistry A* vol. 3 2454–2484 Preprint at https://doi.org/10.1039/c4ta04980b (2015).
35. Fergus, J. W. Recent developments in cathode materials for lithium ion batteries. *Journal of Power Sources* vol. 195 939–954 Preprint at https://doi.org/10.1016/j.jpowsour.2009.08.089 (2010).
36. Xu, J. *et al.* High-Energy Lithium-Ion Batteries: Recent Progress and a Promising Future in Applications. *Energy and Environmental Materials* vol. 6 Preprint at https://doi.org/10.1002/eem2.12450 (2023).
37. Lipu, M. S. H. *et al.* A review of state of health and remaining useful life estimation methods for lithium-ion battery in electric vehicles: Challenges and recommendations. *Journal of Cleaner Production* vol. 205 115–133 Preprint at https://doi.org/10.1016/j.jclepro.2018.09.065 (2018).
38. Zeng, X. *et al.* Commercialization of Lithium Battery Technologies for Electric Vehicles. *Advanced Energy Materials* vol. 9 Preprint at https://doi.org/10.1002/aenm.201900161 (2019).
39. Simon, P. & Gogotsi, Y. Perspectives for electrochemical capacitors and related devices. *Nature Materials* vol. 19 1151–1163 Preprint at https://doi.org/10.1038/s41563-020-0747-z (2020).
40. Winter, M. & Brodd, R. J. What are batteries, fuel cells, and supercapacitors? *Chem Rev* **104**, 4245–4269 (2004).
41. Permatasari, F. A., Irham, M. A., Bisri, S. Z. & Iskandar, F. Carbon-based quantum dots for supercapacitors: Recent advances and future challenges. *Nanomaterials* vol. 11 1–34 Preprint at https://doi.org/10.3390/nano11010091 (2021).

42. Lu, Y. *et al.* Syntheses and Energy Storage Applications of MxSy (M = Cu, Ag, Au) and Their Composites: Rechargeable Batteries and Supercapacitors. *Advanced Functional Materials* vol. 27 Preprint at https://doi.org/10.1002/adfm.201703949 (2017).
43. Gamal, H., Elshahawy, A. M., Medany, S. S., Hefnawy, M. A. & Shalaby, M. S. Recent advances of vanadium oxides and their derivatives in supercapacitor applications: A comprehensive review. *Journal of Energy Storage* vol. 76 Preprint at https://doi.org/10.1016/j.est.2023.109788 (2024).
44. Dong, L. *et al.* Multivalent metal ion hybrid capacitors: A review with a focus on zinc-ion hybrid capacitors. *Journal of Materials Chemistry A* vol. 7 13810–13832 Preprint at https://doi.org/10.1039/c9ta02678a (2019).
45. Yun, H. & He, R. One-dimensional partial differential model for asymmetric hybrid supercapacitor. *J Power Sources* **562**, (2023).
46. Ike, I. S., Sigalas, I. & Iyuke, S. Understanding performance limitation and suppression of leakage current or self-discharge in electrochemical capacitors: A review. *Physical Chemistry Chemical Physics* vol. 18 661–680 Preprint at https://doi.org/10.1039/c5cp05459a (2015).
47. Forouzandeh, P., Kumaravel, V. & Pillai, S. C. Electrode materials for supercapacitors: A review of recent advances. *Catalysts* vol. 10 1–73 Preprint at https://doi.org/10.3390/catal10090969 (2020).
48. Li, Z. *et al.* Atom-economical construction of carbon nanotube architectures for flexible supercapacitors with ultrahigh areal and volumetric capacities. *J Mater Chem A Mater* **6**, 21287–21294 (2018).
49. Kate, R. S., Khalate, S. A. & Deokate, R. J. Overview of nanostructured metal oxides and pure nickel oxide (NiO) electrodes for supercapacitors: A review. *Journal of Alloys and Compounds* vol. 734 89–111 Preprint at https://doi.org/10.1016/j.jallcom.2017.10.262 (2018).
50. Lemian, D. & Bode, F. Battery-Supercapacitor Energy Storage Systems for Electrical Vehicles: A Review. *Energies* vol. 15 Preprint at https://doi.org/10.3390/en15155683 (2022).
51. Xing, F., Bi, Z., Su, F., Liu, F. & Wu, Z. S. Unraveling the Design Principles of Battery-Supercapacitor Hybrid Devices: From Fundamental Mechanisms to Microstructure Engineering and Challenging Perspectives. *Advanced Energy Materials* vol. 12 Preprint at https://doi.org/10.1002/aenm.202200594 (2022).
52. Xiao, J., Momen, R. & Liu, C. Application of carbon quantum dots in supercapacitors: A mini review. *Electrochemistry Communications* vol. 132 Preprint at https://doi.org/10.1016/j.elecom.2021.107143 (2021).
53. Li, L. *et al.* Carbon-based materials for fast charging lithium-ion batteries. *Carbon* vol. 183 721–734 Preprint at https://doi.org/10.1016/j.carbon.2021.07.053 (2021).
54. Zhao, L. F. *et al.* Hard Carbon Anodes: Fundamental Understanding and Commercial Perspectives for Na-Ion Batteries beyond Li-Ion and K-Ion Counterparts. *Advanced Energy Materials* vol. 11 Preprint at https://doi.org/10.1002/aenm.202002704 (2021).

55. Zhang, S., Su, Y., Zhu, S., Zhang, H. & Zhang, Q. Effects of pretreatment and FeCl3 preload of rice husk on synthesis of magnetic carbon composites by pyrolysis for supercapacitor application. *J Anal Appl Pyrolysis* **135**, 22–31 (2018).
56. Wei, J. S. *et al.* A new generation of energy storage electrode materials constructed from carbon dots. *Materials Chemistry Frontiers* vol. 4 729–749 Preprint at https://doi.org/10.1039/c9qm00554d (2020).
57. Gutru, R. *et al.* Recent progress in heteroatom doped carbon based electrocatalysts for oxygen reduction reaction in anion exchange membrane fuel cells. *International Journal of Hydrogen Energy* vol. 48 3593–3631 Preprint at https://doi.org/10.1016/j.ijhydene.2022.10.177 (2023).
58. ul Haque, S., Nasar, A., Duteanu, N. & Inamuddin. Carbon based-nanomaterials used in biofuel cells – A review. *Fuel* vol. 331 Preprint at https://doi.org/10.1016/j.fuel.2022.125634 (2022).
59. Mashkour, M. & Rahimnejad, M. Effect of various carbon-based cathode electrodes on the performance of microbial fuel cell. *Biofuel Research Journal* **2**, 296–300 (2015).
60. Wu, H. *et al.* Stable Li-ion battery anodes by in-situ polymerization of conducting hydrogel to conformally coat silicon nanoparticles. *Nat Commun* **4**, (2013).
61. Wu, Y. P., Rahm, E. & Holze, R. *Carbon Anode Materials for Lithium Ion Batteries*.
62. Lu, J., Chen, Z., Pan, F., Cui, Y. & Amine, K. High-Performance Anode Materials for Rechargeable Lithium-Ion Batteries. *Electrochemical Energy Reviews* vol. 1 35–53 Preprint at https://doi.org/10.1007/s41918-018-0001-4 (2018).
63. Si, Q. *et al.* Highly reversible carbon-nano-silicon composite anodes for lithium rechargeable batteries. *J Power Sources* **189**, 761–765 (2009).
64. Lee, J. H., Kim, W. J., Kim, J. Y., Lim, S. H. & Lee, S. M. Spherical silicon/graphite/carbon composites as anode material for lithium-ion batteries. *J Power Sources* **176**, 353–358 (2008).
65. Shen, G. *et al.* Waste biomass garlic stem-derived porous carbon materials as high-capacity and long-cycling anode for lithium/sodium-ion batteries. *J Colloid Interface Sci* **653**, 1588–1599 (2024).
66. Fujimoto, H. *et al.* Phase Diagram of Li-Graphite Intercalation Compound Formed by the Charge/Discharge Reaction in Li-Ion Battery. *J Electrochem Soc* **169**, 070507 (2022).
67. Yang, Z. *et al.* Electrochemical energy storage for green grid. *Chemical Reviews* vol. 111 3577–3613 Preprint at https://doi.org/10.1021/cr100290v (2011).
68. Wang, G., Yu, M. & Feng, X. Carbon materials for ion-intercalation involved rechargeable battery technologies. *Chemical Society Reviews* vol. 50 2388–2443 Preprint at https://doi.org/10.1039/d0cs00187b (2021).
69. Shi, W. *et al.* Enabling Superior Sodium Capture for Efficient Water Desalination by a Tubular Polyaniline Decorated with Prussian Blue Nanocrystals. *Advanced Materials* **32**, (2020).
70. Grey, C. P. & Tarascon, J. M. Sustainability and in situ monitoring in battery development. *Nature Materials* vol. 16 45–56 Preprint at https://doi.org/10.1038/nmat4777 (2016).

71. Liu, Y., Zhang, S. & Zhu, T. Germanium-Based Electrode Materials for Lithium-Ion Batteries. *ChemElectroChem* **1**, 706–713 (2014).
72. Xiao, C., Usiskin, R. & Maier, J. Passivation Layers in Lithium and Sodium Batteries: Potential Profiles, Stabilities, and Voltage Drops. *Adv Funct Mater* **31**, (2021).
73. Spotte-Smith, E. W. C. *et al.* Toward a Mechanistic Model of Solid-Electrolyte Interphase Formation and Evolution in Lithium-Ion Batteries. *ACS Energy Lett* **7**, 1446–1453 (2022).
74. Xu, R. *et al.* Artificial Interphases for Highly Stable Lithium Metal Anode. *Matter* vol. 1 317–344 Preprint at https://doi.org/10.1016/j.matt.2019.05.016 (2019).
75. Liu, W., Liu, P. & Mitlin, D. Review of Emerging Concepts in SEI Analysis and Artificial SEI Membranes for Lithium, Sodium, and Potassium Metal Battery Anodes. *Advanced Energy Materials* vol. 10 Preprint at https://doi.org/10.1002/aenm.202002297 (2020).
76. Kim, M. *et al.* Sorghum biomass-derived porous carbon electrodes for capacitive deionization and energy storage. *Microporous and Mesoporous Materials* **312**, (2021).
77. Frackowiak, E. & Beguin, F. *Carbon Materials for the Electrochemical Storage of Energy in Capacitors*. *Carbon* vol. 39 (2001).
78. Sharma, P. & Bhatti, T. S. A review on electrochemical double-layer capacitors. *Energy Convers Manag* **51**, 2901–2912 (2010).
79. Li, J. *et al.* A nitrogen-doped mesopore-dominated carbon electrode allied with anti-freezing EMIBF4-GBL electrolyte for superior low-temperature supercapacitors. *J Mater Chem A Mater* **8**, 10386–10394 (2020).
80. Hung, P. yan *et al.* Specializing liquid electrolytes and carbon-based materials in EDLCs for low-temperature applications. *Journal of Energy Chemistry* vol. 68 580–602 Preprint at https://doi.org/10.1016/j.jechem.2021.12.012 (2022).
81. Zhong, C. *et al.* A review of electrolyte materials and compositions for electrochemical supercapacitors. *Chemical Society Reviews* vol. 44 7484–7539 Preprint at https://doi.org/10.1039/c5cs00303b (2015).
82. Li, G., Gao, X., Wang, K. & Cheng, Z. Porous carbon nanospheres with high EDLC capacitance. *Diam Relat Mater* **88**, 12–17 (2018).
83. Shao, H., Wu, Y. C., Lin, Z., Taberna, P. L. & Simon, P. Nanoporous carbon for electrochemical capacitive energy storage. *Chemical Society Reviews* vol. 49 3005–3039 Preprint at https://doi.org/10.1039/d0cs00059k (2020).
84. Chmiola, J. *et al.* Anomalous Increase in Carbon Capacitance at Pore Sizes Less Than 1 Nanometer. *Science (1979)* **313**, 1760–1763 (2006).
85. Wu, H. *et al.* Stable Li-ion battery anodes by in-situ polymerization of conducting hydrogel to conformally coat silicon nanoparticles. *Nat Commun* **4**, (2013).
86. Jagodar, A. *et al.* Growth of graphene nanowalls in low-temperature plasma: Experimental insight in initial growth and importance of wall conditioning. *Appl Surf Sci* **643**, (2024).
87. Liu, N., Huo, K., McDowell, M. T., Zhao, J. & Cui, Y. Rice husks as a sustainable source of nanostructured silicon for high performance Li-ion battery anodes. *Sci Rep* **3**, (2013).

88. Barcaro, E., Marangon, V., Mutarelli, M. & Hassoun, J. A lithium-ion battery with cycling stability promoted by the progressive activation of a silicon oxide anode in graphene-amorphous carbon matrix. *J Power Sources* **595**, 234059 (2024).
89. Han, D. *et al.* Pre-lithiated silicon/carbon nanosphere anode with enhanced cycling ability and coulombic efficiency for lithium-ion batteries. *J Energy Storage* **79**, (2024).
90. Choi, M., Kim, J. C. & Kim, D. W. Waste Windshield-Derived Silicon/Carbon Nanocomposites as High-Performance Lithium-Ion Battery Anodes. *Sci Rep* **8**, (2018).
91. Di, F. *et al.* Surface modification and functional structure space design to improve the cycle stability of silicon based materials as anode of lithium ion batteries. *Coatings* vol. 11 Preprint at https://doi.org/10.3390/coatings11091047 (2021).
92. Duan, J. *et al.* The design and regulation of porous silicon-carbon composites for enhanced electrochemical lithium storage performance. *Journal of Industrial and Engineering Chemistry* **131**, 410–421 (2024).
93. Lai, P., Liu, C., Sun, Z., Nie, E. & Zhang, Z. Investigation of porous multi-carbon layers constructed on submicron silicon flakes for high-performance Li-ion batteries anode. *Solid State Sci* **148**, 107408 (2024).
94. Chae, S., Choi, S., Kim, N., Sung, J. & Cho, J. Graphit- und-Silicium-Anoden für Lithiumionen-Hochenergiebatterien. *Angewandte Chemie* **132**, 112–138 (2020).
95. Dimov, N., Kugino, S. & Yoshio, M. Carbon-coated silicon as anode material for lithium ion batteries: Advantages and limitations. *Electrochim Acta* **48**, 1579–1587 (2003).
96. Soukupová, G. *et al.* Novel silicon nanoparticles-based carbonized polypyrrole nanotube composites as anode materials for Li-ion batteries. *J Power Sources* **593**, (2024).
97. Guo, J., Chen, X. & Wang, C. Carbon scaffold structured silicon anodes for lithium-ion batteries. *J Mater Chem* **20**, 5035–5040 (2010).
98. Terranova, M. L., Orlanducci, S., Tamburri, E., Guglielmotti, V. & Rossi, M. Si/C hybrid nanostructures for Li-ion anodes: An overview. *Journal of Power Sources* vol. 246 167–177 Preprint at https://doi.org/10.1016/j.jpowsour.2013.07.065 (2014).
99. Guo, J., Sun, A. & Wang, C. A porous silicon-carbon anode with high overall capacity on carbon fiber current collector. *Electrochem commun* **12**, 981–984 (2010).
100. Xiang, Z. *et al.* Submicro-sized porous SiO2/C and SiO2/C/graphene spheres for lithium ion batteries. *Journal of Solid State Electrochemistry* **21**, 2425–2432 (2017).
101. Zhang, Y. C. *et al.* Rice husk-derived hierarchical silicon/nitrogen-doped carbon/carbon nanotube spheres as low-cost and high-capacity anodes for lithium-ion batteries. *Nano Energy* **25**, 120–127 (2016).
102. Sohn, M. *et al.* Microstructure Controlled Porous Silicon Particles as a High Capacity Lithium Storage Material via Dual Step Pore Engineering. *Adv Funct Mater* **28**, (2018).
103. Zhao, L., Bennett, J. C., George, A. & Obrovac, M. N. SiC-Free Carbon-Silicon Alloys Prepared by Delithiation as Lithium-Ion Battery Negative Electrodes. *Chemistry of Materials* **31**, 3883–3890 (2019).

104. Kim, S. O. & Manthiram, A. A facile, low-cost synthesis of high-performance silicon-based composite anodes with high tap density for lithium-ion batteries. *J Mater Chem A Mater* **3**, 2399–2406 (2015).
105. Sui, D. *et al.* A high-performance ternary Si composite anode material with crystal graphite core and amorphous carbon shell. *J Power Sources* **384**, 328–333 (2018).
106. Ren, Y. *et al.* Preparation and characterization of silicon monoxide/graphite/carbon nanotubes composite as anode for lithium-ion batteries. *Journal of Solid State Electrochemistry* **16**, 1453–1460 (2012).
107. Parekh, M. H., Sediako, A. D., Naseri, A., Thomson, M. J. & Pol, V. G. In Situ Mechanistic Elucidation of Superior Si-C-Graphite Li-Ion Battery Anode Formation with Thermal Safety Aspects. *Adv Energy Mater* **10**, (2020).
108. Rattes, A. L. R. & Oliveira, W. P. Spray drying conditions and encapsulating composition effects on formation and properties of sodium diclofenac microparticles. *Powder Technol* **171**, 7–14 (2007).
109. Sosnik, A. & Seremeta, K. P. Advantages and challenges of the spray-drying technology for the production of pure drug particles and drug-loaded polymeric carriers. *Advances in Colloid and Interface Science* vol. 223 40–54 Preprint at https://doi.org/10.1016/j.cis.2015.05.003 (2015).
110. Carné-Sánchez, A., Imaz, I., Cano-Sarabia, M. & Maspoch, D. A spray-drying strategy for synthesis of nanoscale metal-organic frameworks and their assembly into hollow superstructures. *Nat Chem* **5**, 203–211 (2013).
111. Jung, D. S., Hwang, T. H., Park, S. Bin & Choi, J. W. Spray drying method for large-scale and high-performance silicon negative electrodes in Li-ion batteries. *Nano Lett* **13**, 2092–2097 (2013).
112. Paireau, C. *et al.* Si/C composites prepared by spray drying from cross-linked polyvinyl alcohol as Li-ion batteries anodes. *Electrochim Acta* **174**, 361–368 (2015).
113. Gan, L. *et al.* A facile synthesis of graphite/silicon/graphene spherical composite anode for lithium-ion batteries. *Electrochim Acta* **104**, 117–123 (2013).
114. Xu, Q. *et al.* Watermelon-Inspired Si/C Microspheres with Hierarchical Buffer Structures for Densely Compacted Lithium-Ion Battery Anodes. *Adv Energy Mater* **7**, (2017).
115. Yi, Z., Qian, Y., Cao, C., Lin, N. & Qian, Y. Porous Si/C microspheres decorated with stable outer carbon interphase and inner interpenetrated Si@C channel for enhanced lithium storage. *Carbon N Y* **149**, 664–671 (2019).
116. Askaruly, K. *et al.* The electrochemical behavior of silica and activated carbon materials derived from the rice husk waste for li-ion cells. *Diam Relat Mater* **133**, (2023).
117. Shen, T. *et al.* Encapsulating silicon nanoparticles into mesoporous carbon forming pomegranate-structured microspheres as a high-performance anode for lithium ion batteries. *J Mater Chem A Mater* **5**, 11197–11203 (2017).

118. Jeong, M. G. *et al.* Self-Rearrangement of Silicon Nanoparticles Embedded in Micro-Carbon Sphere Framework for High-Energy and Long-Life Lithium-Ion Batteries. *Nano Lett* **17**, 5600–5606 (2017).
119. Chang, P. *et al.* Constructing Three-Dimensional Honeycombed Graphene/Silicon Skeletons for High-Performance Li-Ion Batteries. *ACS Appl Mater Interfaces* **9**, 31879–31886 (2017).
120. Lu, M., Tian, Y., Zheng, X., Gao, J. & Huang, B. *Preparation, Characterization and Electrochemical Performance of Silicon Coated Natural Graphite as Anode for Lithium Ion Batteries*. *Int. J. Electrochem. Sci* vol. 7 www.electrochemsci.org (2012).
121. Jeong, S. *et al.* Hard carbon coated nano-Si/graphite composite as a high performance anode for Li-ion batteries. *J Power Sources* **329**, 323–329 (2016).
122. Uono, H., Kim, B.-C., Fuse, T., Ue, M. & Yamaki, J. Optimized Structure of Silicon/Carbon/Graphite Composites as an Anode Material for Li-Ion Batteries. *J Electrochem Soc* **153**, A1708 (2006).
123. Son, I. H., Park, J. H., Kwon, S., Choi, J. W. & Rümmeli, M. H. Graphene coating of silicon nanoparticles with CO2-enhanced chemical vapor deposition. *Small* **12**, 658–667 (2016).
124. Natali, M., Passeri, D., Rossi, M., Dikonimos, T. & Lisi, N. *Plasma Enhanced Hot Filament CVD Growth of Thick Carbon Nanowall Layers*.
125. Ko, M. *et al.* Scalable synthesis of silicon-nanolayer-embedded graphite for high-energy lithium-ion batteries. *Nat Energy* **1**, (2016).
126. Chen, Y., Zhang, X., Tian, Y. & Zhao, X. Synthesis and characterization of silicon nanoparticles inserted into graphene sheets as high performance anode material for lithium ion batteries. *J Nanomater* **2014**, (2014).
127. Lee, J. H. & Park, S. J. Recent advances in preparations and applications of carbon aerogels: A review. *Carbon* vol. 163 1–18 Preprint at https://doi.org/10.1016/j.carbon.2020.02.073 (2020).
128. Li, J., Wang, X., Huang, Q., Gamboa, S. & Sebastian, P. J. Studies on preparation and performances of carbon aerogel electrodes for the application of supercapacitor. *J Power Sources* **158**, 784–788 (2006).
129. Worsley, M. A., Satcher, J. H. & Baumann, T. F. Synthesis and characterization of monolithic carbon aerogel nanocomposites containing double-walled carbon nanotubes. *Langmuir* **24**, 9763–9766 (2008).
130. Bauli, C. R., Rocha, D. B., de Oliveira, S. A. & Rosa, D. S. Cellulose nanostructures from wood waste with low input consumption. *J Clean Prod* **211**, 408–416 (2019).
131. Kumar, Y. *et al.* Wind energy: Trends and enabling technologies. *Renewable and Sustainable Energy Reviews* vol. 53 209–224 Preprint at https://doi.org/10.1016/j.rser.2015.07.200 (2016).
132. Scaramuzzo, F. A. *et al.* Efficient photocurrent generation using a combined Ni-TiO2 nanotubes anode. *J Appl Electrochem* **45**, 727–733 (2015).

133. DuChanois, R. M., Porter, C. J., Violet, C., Verduzco, R. & Elimelech, M. Membrane Materials for Selective Ion Separations at the Water–Energy Nexus. *Advanced Materials* vol. 33 Preprint at https://doi.org/10.1002/adma.202101312 (2021).
134. Zimmerman, J. B., Anastas, P. T., Erythropel, H. C. & Leitner, W. *Designing for a Green Chemistry Future*. https://www.science.org.
135. Harper, G. *et al.* Recycling lithium-ion batteries from electric vehicles. *Nature* vol. 575 75–86 Preprint at https://doi.org/10.1038/s41586-019-1682-5 (2019).
136. Dodson, J. R. *et al.* Bio-derived materials as a green route for precious & critical metal recovery and re-use. *Green Chemistry* **17**, 1951–1965 (2015).
137. Clark, J. H. Green chemistry: Today (and tomorrow). *Green Chemistry* **8**, 17–21 (2006).
138. Bressi, V., Ferlazzo, A., Iannazzo, D. & Espro, C. Graphene quantum dots by eco-friendly green synthesis for electrochemical sensing: Recent advances and future perspectives. *Nanomaterials* vol. 11 Preprint at https://doi.org/10.3390/nano11051120 (2021).
139. EU COM(2020) 98. *A New Circular Economy Action Plan For a Cleaner and More Competitive Europe*. https://www.un.org/sustainabledevelopment/sustainable-consumption-production/ (2020).
140. Dell'Era, A. *et al.* Synthesis, characterization, and electrochemical behavior of LiMnxFe(1-x)PO4 composites obtained from phenylphosphonate-based organic-inorganic hybrids. *Materials* **11**, (2018).
141. Dell'Era, A. *et al.* Spinning disk reactor technique for the synthesis of nanometric sulfur TiO2Core-Shell powder for lithium batteries. *Applied Sciences (Switzerland)* **9**, (2019).
142. La Monaca, A. *et al.* 1,3-Dioxolane: A Strategy to Improve Electrode Interfaces in Lithium Ion and Lithium-Sulfur Batteries. *ChemElectroChem* **5**, 1272–1278 (2018).
143. Tarquini, G. *et al.* Polysulfide solution effects on Li[sbnd]S batteries performances. *Journal of Electroanalytical Chemistry* **870**, (2020).
144. Gao, Y., Pan, Z., Sun, J., Liu, Z. & Wang, J. High-Energy Batteries: Beyond Lithium-Ion and Their Long Road to Commercialisation. *Nano-Micro Letters* vol. 14 Preprint at https://doi.org/10.1007/s40820-022-00844-2 (2022).
145. Scaramuzzo, F. A. *et al.* TiO2 nanotubes photo-anode: An innovative cell design. *Chem Eng Trans* **41**, 223–228 (2014).
146. Egorov, V. & O'Dwyer, C. Architected porous metals in electrochemical energy storage. *Current Opinion in Electrochemistry* vol. 21 201–208 Preprint at https://doi.org/10.1016/j.coelec.2020.02.011 (2020).
147. Kalair, A., Abas, N., Saleem, M. S., Kalair, A. R. & Khan, N. Role of energy storage systems in energy transition from fossil fuels to renewables. *Energy Storage* **3**, (2021).
148. Qin, B., Wu, Y., Qiu, R. & Ruan, J. Preparing La-Doped LiAl5O8 from the Electrode Materials of Waste Lithium-Ion Batteries. *ACS Sustain Chem Eng* (2022) doi:10.1021/acssuschemeng.2c05893.

149. Dell'Era, A. *et al.* Carbon powder material obtained from an innovative high pressure water jet recycling process of tires used as anode in alkali ion (Li, Na) batteries. *Solid State Ion* **324**, 20–27 (2018).
150. Kazemi Shariat Panahi, H. *et al.* Bioethanol production from food wastes rich in carbohydrates. *Current Opinion in Food Science* vol. 43 71–81 Preprint at https://doi.org/10.1016/j.cofs.2021.11.001 (2022).
151. Devi, A. *et al.* Lignocellulosic Biomass Valorization for Bioethanol Production: a Circular Bioeconomy Approach. *Bioenergy Research* vol. 15 1820–1841 Preprint at https://doi.org/10.1007/s12155-022-10401-9 (2022).
152. Souza Piao, R. *et al.* Barriers toward circular economy transition: Exploring different stakeholders' perspectives. *Corp Soc Responsib Environ Manag* (2023) doi:10.1002/csr.2558.
153. Fuss, M., Barros, R. T. V. & Poganietz, W. R. The role of a socio-integrated recycling system in implementing a circular economy – The case of Belo Horizonte, Brazil. *Waste Management* **121**, 215–225 (2021).
154. Troschinetz, A. M. & Mihelcic, J. R. Sustainable recycling of municipal solid waste in developing countries. *Waste Management* **29**, 915–923 (2009).
155. Fehrer, J. A. & Wieland, H. A systemic logic for circular business models. *J Bus Res* **125**, 609–620 (2021).
156. Verleye, K. *et al.* Pushing Forward the Transition to a Circular Economy by Adopting an Actor Engagement Lens. *J Serv Res* **27**, 69–88 (2024).
157. Bidmon, C. M. & Knab, S. F. The three roles of business models in societal transitions: New linkages between business model and transition research. *J Clean Prod* **178**, 903–916 (2018).
158. Ellen MacArthur Foundation. *"Growth within: A Circular Economy Vision for a Competitive Europe."* (2015).
159. Acerbi, F. & Taisch, M. A literature review on circular economy adoption in the manufacturing sector. *Journal of Cleaner Production* vol. 273 Preprint at https://doi.org/10.1016/j.jclepro.2020.123086 (2020).
160. Corvellec, H., Stowell, A. F. & Johansson, N. Critiques of the circular economy. *J Ind Ecol* **26**, 421–432 (2022).
161. Baxter, W., Aurisicchio, M. & Childs, P. Contaminated Interaction: Another Barrier to Circular Material Flows. *J Ind Ecol* **21**, 507–516 (2017).
162. Velis, C. A. & Vrancken, K. C. Which material ownership and responsibility in a circular economy? *Waste Management and Research* vol. 33 773–774 Preprint at https://doi.org/10.1177/0734242X15599305 (2015).
163. Cullen, J. M. Circular Economy: Theoretical Benchmark or Perpetual Motion Machine? *Journal of Industrial Ecology* vol. 21 483–486 Preprint at https://doi.org/10.1111/jiec.12599 (2017).
164. Mavropoulos, A. & Nilsen, A. W. *Industry 4.0 and Circular Economy: Towards a Wasteless Future or a Wasteful Planet?* (Hoboken, NJ, 2020).
165. Traven, L. Circular economy and the waste management hierarchy: Friends or foes of sustainable economic growth? A critical appraisal illustrated by the case of the Republic of

Croatia. *Waste Management and Research* vol. 37 1–2 Preprint at https://doi.org/10.1177/0734242X18818985 (2019).

166. Tian, Y. X. *et al.* Hierarchical Porous Carbon Prepared through Sustainable CuCl 2 Activation of Rice Husk for High-Performance Supercapacitors. *ChemistrySelect* **4**, 2314–2319 (2019).
167. Zhang, S., Zhang, Q., Zhu, S., Zhang, H. & Liu, X. Porous Carbons Derived from Desilication Treatment and Mixed Alkali Activation of Rice Husk Char for Supercapacitors. *Energy Sources, Part A: Recovery, Utilization and Environmental Effects* **43**, 282–290 (2021).
168. Tang, L., Feng, Y., He, W. & Yang, F. Combination of graphene oxide with flax-derived cellulose dissolved in NaOH/urea medium to generate hierarchically structured composite carbon aerogels. *Ind Crops Prod* **130**, 179–183 (2019).
169. Kumar, M., Ambika, S., Hassani, A. & Nidheesh, P. V. Waste to catalyst: Role of agricultural waste in water and wastewater treatment. *Science of the Total Environment* vol. 858 Preprint at https://doi.org/10.1016/j.scitotenv.2022.159762 (2023).
170. Saleem, M. Possibility of utilizing agriculture biomass as a renewable and sustainable future energy source. *Heliyon* vol. 8 Preprint at https://doi.org/10.1016/j.heliyon.2022.e08905 (2022).
171. Hai, T. *et al.* Reduction in environmental CO2 by utilization of optimized energy scheme for power and fresh water generations based on different uses of biomass energy. *Chemosphere* 137847 (2023) doi:10.1016/j.chemosphere.2023.137847.
172. Sundarraj Antony, A., Allwyn Sundarraj, A. & Vasudevan Ranganathan, T. *A Review on Cellulose and Its Utilization from Agro-industrial Waste*. vol. 10 https://www.researchgate.net/publication/324442289 (2018).
173. Jeong, S. S., Böckenfeld, N., Balducci, A., Winter, M. & Passerini, S. Natural cellulose as binder for lithium battery electrodes. *J Power Sources* **199**, 331–335 (2012).
174. Sam, D. K. *et al.* Synthesis of biomass-based carbon aerogels in energy and sustainability. *Carbohydrate Research* vol. 491 Preprint at https://doi.org/10.1016/j.carres.2020.107986 (2020).
175. Wu, H. *et al.* Highly flexible, foldable and stretchable Ni-Co layered double hydroxide/polyaniline/bacterial cellulose electrodes for high-performance all-solid-state supercapacitors. *J Mater Chem A Mater* **6**, 16617–16626 (2018).
176. Cui, J. *et al.* Microsized Porous SiOx@C Composites Synthesized through Aluminothermic Reduction from Rice Husks and Used as Anode for Lithium-Ion Batteries. *ACS Appl Mater Interfaces* **8**, 30239–30247 (2016).
177. Liu, N., Huo, K., McDowell, M. T., Zhao, J. & Cui, Y. Rice husks as a sustainable source of nanostructured silicon for high performance Li-ion battery anodes. *Sci Rep* **3**, (2013).
178. Jyothsna, G., Bahurudeen, A. & K Sahu, P. Sustainable utilisation of rice husk for cleaner energy: A circular economy between agricultural, energy and construction sectors. *Materials Today Sustainability* **25**, (2024).

179. Vassilev, S. V., Baxter, D., Andersen, L. K. & Vassileva, C. G. An overview of the chemical composition of biomass. *Fuel* vol. 89 913–933 Preprint at https://doi.org/10.1016/j.fuel.2009.10.022 (2010).
180. Thy, P., Lesher, C. E. & Jenkins, B. M. *Experimental Determination of High-Temperature Elemental Losses from Biomass Slag*. www.elsevier.com/locate/fuel.
181. Thy, P., Jenkins, B. M., Grundvig, S., Shiraki, R. & Lesher, C. E. High temperature elemental losses and mineralogical changes in common biomass ashes. *Fuel* **85**, 783–795 (2006).
182. Soltani, N., Bahrami, A., Pech-Canul, M. I. & González, L. A. Review on the physicochemical treatments of rice husk for production of advanced materials. *Chemical Engineering Journal* vol. 264 899–935 Preprint at https://doi.org/10.1016/j.cej.2014.11.056 (2015).
183. Pode, R. Potential applications of rice husk ash waste from rice husk biomass power plant. *Renewable and Sustainable Energy Reviews* vol. 53 1468–1485 Preprint at https://doi.org/10.1016/j.rser.2015.09.051 (2016).
184. Li, B. *et al.* Rice husk-derived hybrid lithium-ion capacitors with ultra-high energy. *J Mater Chem A Mater* **5**, 24502–24507 (2017).
185. Cui, J. *et al.* High surface area C/SiO2 composites from rice husks as a high-performance anode for lithium ion batteries. *Powder Technol* **311**, 1–8 (2017).
186. Jin, H. *et al.* Synthesis of porous carbon nano-onions derived from rice husk for high-performance supercapacitors. *Appl Surf Sci* **488**, 593–599 (2019).
187. Jian, F. M. *et al.* A silicon transporter in rice. *Nature* **440**, 688–691 (2006).
188. Xing, A., Tian, S., Tang, H., Losic, D. & Bao, Z. Mesoporous silicon engineered by the reduction of biosilica from rice husk as a high-performance anode for lithium-ion batteries. *RSC Adv.* **3**, 10145–10149 (2013).
189. Hillier, N., Yong, S. & Beeby, S. The good, the bad and the porous: A review of carbonaceous materials for flexible supercapacitor applications. in *Energy Reports* vol. 6 148–156 (Elsevier Ltd, 2020).
190. Kim, H. *et al.* Facile One-Pot Synthesis of Bimetallic Co/Mn-MOFs@Rice Husks, and its Carbonization for Supercapacitor Electrodes. *Sci Rep* **9**, (2019).
191. Sathyamoorthi, S., Phattharasupakun, N. & Sawangphruk, M. Environmentally benign non-fluoro deep eutectic solvent and free-standing rice husk-derived bio-carbon based high-temperature supercapacitors. *Electrochim Acta* **286**, 148–157 (2018).
192. Chien, H. C., Cheng, W. Y., Wang, Y. H. & Lu, S. Y. Ultrahigh specific capacitances for supercapacitors achieved by nickel cobaltite/carbon aerogel composites. *Adv Funct Mater* **22**, 5038–5043 (2012).
193. Yu, S., Song, S., Li, R. & Fang, B. The lightest solid meets the lightest gas: An overview of carbon aerogels and their composites for hydrogen related applications. *Nanoscale* **12**, 19536–19556 (2020).
194. Lee, J. H. & Park, S. J. Recent advances in preparations and applications of carbon aerogels: A review. *Carbon* vol. 163 1–18 Preprint at https://doi.org/10.1016/j.carbon.2020.02.073 (2020).

195. Hu, L., He, R., Lei, H. & Fang, D. Carbon Aerogel for Insulation Applications: A Review. *International Journal of Thermophysics* vol. 40 Preprint at https://doi.org/10.1007/s10765-019-2505-5 (2019).
196. Wang, L. *et al.* Multi-functionalized carbon aerogels derived from chitosan. *J Colloid Interface Sci* **605**, 790–802 (2022).
197. Liu, Y., Liu, J. & Song, P. Recent advances in polysaccharide-based carbon aerogels for environmental remediation and sustainable energy. *Sustainable Materials and Technologies* vol. 27 Preprint at https://doi.org/10.1016/j.susmat.2020.e00240 (2021).
198. Meng, Y. *et al.* A lignin-based carbon aerogel enhanced by graphene oxide and application in oil/water separation. *Fuel* **278**, (2020).
199. Gan, G. *et al.* Carbon Aerogels for Environmental Clean-Up. *European Journal of Inorganic Chemistry* vol. 2019 3126–3141 Preprint at https://doi.org/10.1002/ejic.201801512 (2019).
200. Baumann, T. F., Worsley, M. A., Han, T. Y. J. & Satcher, J. H. High surface area carbon aerogel monoliths with hierarchical porosity. *J Non Cryst Solids* **354**, 3513–3515 (2008).
201. Ma, C. B., Du, B. & Wang, E. Self-Crosslink Method for a Straightforward Synthesis of Poly(Vinyl Alcohol)-Based Aerogel Assisted by Carbon Nanotube. *Adv Funct Mater* **27**, (2017).
202. Justh, N. *et al.* Photocatalytic properties of TiO 2 @polymer and TiO 2 @carbon aerogel composites prepared by atomic layer deposition. *Carbon N Y* **147**, 476–482 (2019).
203. Zuo, L. *et al.* Polymer/Carbon-Based Hybrid Aerogels: Preparation, Properties and Applications. *Materials* vol. 8 6806–6848 Preprint at https://doi.org/10.3390/ma8105343 (2015).
204. Chen, T. *et al.* Bio-Inspired Biomass-Derived Carbon Aerogels with Superior Mechanical Property for Oil–Water Separation. *ACS Sustain Chem Eng* **8**, 6458–6465 (2020).
205. Anoshkin, I. V., Campion, J., Lioubtchenko, D. V. & Oberhammer, J. Freeze-Dried Carbon Nanotube Aerogels for High-Frequency Absorber Applications. *ACS Appl Mater Interfaces* **10**, 19806–19811 (2018).
206. Yamamoto, T., Nishimura, T., Suzuki, T. & Tamon, H. *Control of Mesoporosity of Carbon Gels Prepared by Sol±gel Polycondensation and Freeze Drying*. www.elsevier.com/locate/jnoncrysol.
207. Bauli, C. R., Rocha, D. B., de Oliveira, S. A. & Rosa, D. S. Cellulose nanostructures from wood waste with low input consumption. *J Clean Prod* **211**, 408–416 (2019).
208. Cai, T., Wang, H., Jin, C., Sun, Q. & Nie, Y. Fabrication of nitrogen-doped porous electrically conductive carbon aerogel from waste cabbage for supercapacitors and oil/water separation. *Journal of Materials Science: Materials in Electronics* **29**, 4334–4344 (2018).
209. Dini, D. *et al.* Review—Multiscale Characterization of Li-Ion Batteries through the Combined Use of Atomic Force Microscopy and X-ray Microscopy and Considerations for a Correlative Analysis of the Reviewed Data. *J Electrochem Soc* **168**, 126522 (2021).
210. Zu, G. *et al.* Nanocellulose-derived highly porous carbon aerogels for supercapacitors. *Carbon N Y* **99**, 203–211 (2016).

211. Kim, H. *et al.* Facile One-Pot Synthesis of Bimetallic Co/Mn-MOFs@Rice Husks, and its Carbonization for Supercapacitor Electrodes. *Sci Rep* **9**, (2019).
212. Zhu, S. *et al.* The photoluminescence mechanism in carbon dots (graphene quantum dots, carbon nanodots, and polymer dots): current state and future perspective. *Nano Research* vol. 8 355–381 Preprint at https://doi.org/10.1007/s12274-014-0644-3 (2015).
213. Semeniuk, M. *et al.* Future Perspectives and Review on Organic Carbon Dots in Electronic Applications. *ACS Nano* **13**, 6224–6255 (2019).
214. The Royal Swedish Academy of Sciences. The Nobel Prize in Chemistry 2023. *PRESS RELEASE - The Royal Swedish Academy of Sciences* 1–1 (2023).
215. Wei, J. S. *et al.* Integrating Carbon Dots with Porous Hydrogels to Produce Full Carbon Electrodes for Electric Double-Layer Capacitors. *ACS Appl Energy Mater* **3**, 6907–6914 (2020).
216. Wei, J. S. *et al.* Robust Negative Electrode Materials Derived from Carbon Dots and Porous Hydrogels for High-Performance Hybrid Supercapacitors. *Advanced Materials* **31**, (2019).
217. Calabro, R. L., Yang, D. S. & Kim, D. Y. Controlled Nitrogen Doping of Graphene Quantum Dots through Laser Ablation in Aqueous Solutions for Photoluminescence and Electrocatalytic Applications. *ACS Appl Nano Mater* **2**, 6948–6959 (2019).
218. Ahirwar, S., Mallick, S. & Bahadur, D. Electrochemical Method to Prepare Graphene Quantum Dots and Graphene Oxide Quantum Dots. *ACS Omega* **2**, 8343–8353 (2017).
219. Wu, M. *et al.* Preparation of functionalized water-soluble photoluminescent carbon quantum dots from petroleum coke. *Carbon N Y* **78**, 480–489 (2014).
220. Li, M. *et al.* Solvothermal conversion of coal into nitrogen-doped carbon dots with singlet oxygen generation and high quantum yield. *Chemical Engineering Journal* **320**, 570–575 (2017).
221. Shaker, M., Riahifar, R. & Li, Y. A review on the superb contribution of carbon and graphene quantum dots to electrochemical capacitors' performance: Synthesis and application. *FlatChem* vol. 22 Preprint at https://doi.org/10.1016/j.flatc.2020.100171 (2020).
222. Yang, X. *et al.* Integrated Carbon Dots-Matrix Structures: An Efficient Strategy for High-Performance Electric Double Layer Capacitors. *ACS Appl Energy Mater* **3**, 4958–4964 (2020).
223. Dang, Y. Q. *et al.* Electrochemical and capacitive properties of carbon dots/reduced graphene oxide supercapacitors. *Nanomaterials* **6**, (2016).
224. Yang, Z. *et al.* Zero-Dimensional Carbon Nanomaterials for Fluorescent Sensing and Imaging. *Chemical Reviews* vol. 123 11047–11136 Preprint at https://doi.org/10.1021/acs.chemrev.3c00186 (2023).
225. Wang, H. *et al.* Carbon dot-modified mesoporous carbon as a supercapacitor with enhanced light-assisted capacitance. *Nanoscale* **12**, 17925–17930 (2020).
226. Zhu, Y. *et al.* A carbon quantum dot decorated RuO2 network: Outstanding supercapacitances under ultrafast charge and discharge. *Energy Environ Sci* **6**, 3665–3675 (2013).
227. Li, X., Rui, M., Song, J., Shen, Z. & Zeng, H. Carbon and Graphene Quantum Dots for Optoelectronic and Energy Devices: A Review. *Adv Funct Mater* **25**, 4929–4947 (2015).

228. Yang, L. *et al.* Hierarchical MoO2/Mo2C/C Hybrid Nanowires as High-Rate and Long-Life Anodes for Lithium-Ion Batteries. *ACS Appl Mater Interfaces* **8**, 19987–19993 (2016).
229. Yun, X. *et al.* Porous Fe2O3 Modified by Nitrogen-Doped Carbon Quantum Dots/Reduced Graphene Oxide Composite Aerogel as a High-Capacity and High-Rate Anode Material for Alkaline Aqueous Batteries. *ACS Appl Mater Interfaces* **11**, 36970–36984 (2019).
230. Khan, F., Oh, M. & Kim, J. H. N-functionalized graphene quantum dots: Charge transporting layer for high-rate and durable Li4Ti5O12-based Li-ion battery. *Chemical Engineering Journal* **369**, 1024–1033 (2019).
231. Wei, J. S. *et al.* High volumetric supercapacitor with a long life span based on polymer dots and graphene sheets. *J Power Sources* **364**, 465–472 (2017).
232. Qu, D. & Sun, Z. The formation mechanism and fluorophores of carbon dots synthesized: Via a bottom-up route. *Materials Chemistry Frontiers* vol. 4 400–420 Preprint at https://doi.org/10.1039/c9qm00552h (2020).
233. Ramdon, S., Bhushan, B. & Nagpure, S. C. In situ electrochemical studies of lithium-ion battery cathodes using atomic force microscopy. *J Power Sources* **249**, 373–384 (2014).
234. Cognigni, F. *et al.* X-Ray Microscopy: A Non-Destructive Multi-Scale Imaging to Study the Inner Workings of Batteries. *ChemElectroChem* (2023) doi:10.1002/celc.202201081.
235. Nicholson J Electroanal, S. B., Wang, C. S., Zhang, X. B., Qi, Z. F. & Lib, W. Z. *Department o f Energy, COO-1545-TI*. *Denki Kagaku oyobi Kogyo Butsuri Kagaku* vol. 145 (1998).
236. Huang, R., Fan, X., Shen, W. & Zhu, J. Carbon-coated silicon nanowire array films for high-performance lithium-ion battery anodes. *Appl Phys Lett* **95**, (2009).
237. Tian, Y. X. *et al.* Hierarchical Porous Carbon Prepared through Sustainable CuCl 2 Activation of Rice Husk for High-Performance Supercapacitors. *ChemistrySelect* **4**, 2314–2319 (2019).
238. Li, X. *et al.* In Situ/Operando Characterization Techniques to Probe the Electrochemical Reactions for Energy Conversion. *Small Methods* vol. 2 Preprint at https://doi.org/10.1002/SMTD.201700395 (2018).
239. Brant, W. R., Li, D., Gu, Q. & Schmid, S. Comparative analysis of ex-situ and operando X-ray diffraction experiments for lithium insertion materials. *J Power Sources* **302**, 126–134 (2016).
240. Nelson Weker, J. & Toney, M. F. Emerging in Situ and Operando Nanoscale X-Ray Imaging Techniques for Energy Storage Materials. *Advanced Functional Materials* vol. 25 1622–1637 Preprint at https://doi.org/10.1002/adfm.201403409 (2015).
241. Li, X., Yang, X., Zhang, J., Huang, Y. & Liu, B. In Situ/Operando Techniques for Characterization of Single-Atom Catalysts. *ACS Catalysis* vol. 9 2521–2531 Preprint at https://doi.org/10.1021/acscatal.8b04937 (2019).
242. Agubra, V. A. & Fergus, J. W. The formation and stability of the solid electrolyte interface on the graphite anode. *Journal of Power Sources* vol. 268 153–162 Preprint at https://doi.org/10.1016/j.jpowsour.2014.06.024 (2014).
243. Chen, H., Qin, Z., He, M., Liu, Y. & Wu, Z. Application of electrochemical atomic force microscopy (EC-AFM) in the corrosion study of metallic materials. *Materials* vol. 13 Preprint at https://doi.org/10.3390/ma13030668 (2020).

244. Bertrand, G. *et al. In-Situ Electrochemical Atomic Force Microscopy Studies of Aqueous Corrosion and Inhibition of Copper*. *Journal of Electroanalytical Chemistry* vol. 489 www.elsevier.nl/locate/jelechem (2000).
245. Chen, W., Li, C. M., Yu, L., Lu, Z. & Zhou, Q. In situ AFM study of electrochemical synthesis of polypyrrole/Au nanocomposite. *Electrochem commun* **10**, 1340–1343 (2008).
246. Hodges, C. S. *Measuring Forces with the AFM: Polymeric Surfaces in Liquids*. (2002).
247. Zhang, Z. *et al.* Characterizing Batteries by In Situ Electrochemical Atomic Force Microscopy: A Critical Review. *Advanced Energy Materials* vol. 11 Preprint at https://doi.org/10.1002/aenm.202101518 (2021).
248. Srinivasan, V. & Newman, J. Discharge Model for the Lithium Iron-Phosphate Electrode. *J Electrochem Soc* **151**, A1517 (2004).
249. Shaker, M., Riahifar, R. & Li, Y. A review on the superb contribution of carbon and graphene quantum dots to electrochemical capacitors' performance: Synthesis and application. *FlatChem* vol. 22 Preprint at https://doi.org/10.1016/j.flatc.2020.100171 (2020).
250. Yang, X. *et al.* Integrated Carbon Dots-Matrix Structures: An Efficient Strategy for High-Performance Electric Double Layer Capacitors. *ACS Appl Energy Mater* **3**, 4958–4964 (2020).